AWARD NUMBER: W81XWH-19-1-0194

TITLE: Early Detection of Lung Cancer Through Molecular Analyses of Single Extracellular Vesicle

PRINCIPAL INVESTIGATOR: Dr. Hakho Lee

CONTRACTING ORGANIZATION: MASSACHUSETTS GENERAL HOSPITAL
55 FRUIT ST
BOSTON MA 02114-2621

REPORT DATE: August 2020

TYPE OF REPORT: Annual

PREPARED FOR: U.S. Army Medical Research and Materiel Command
Fort Detrick, Maryland 21702-5012

DISTRIBUTION STATEMENT: Approved for Public Release;
Distribution Unlimited

The views, opinions and/or findings contained in this report are those of the author(s) and should not be construed as an official Department of the Army position, policy or decision unless so designated by other documentation.

REPORT DOCUMENTATION PAGE

Form Approved
OMB No. 0704-0188

Public reporting burden for this collection of information is estimated to average 1 hour per response, including the time for reviewing instructions, searching existing data sources, gathering and maintaining the data needed, and completing and reviewing this collection of information. Send comments regarding this burden estimate or any other aspect of this collection of information, including suggestions for reducing this burden to Department of Defense, Washington Headquarters Services, Directorate for Information Operations and Reports (0704-0188), 1215 Jefferson Davis Highway, Suite 1204, Arlington, VA 22202-4302. Respondents should be aware that notwithstanding any other provision of law, no person shall be subject to any penalty for failing to comply with a collection of information if it does not display a currently valid OMB control number. **PLEASE DO NOT RETURN YOUR FORM TO THE ABOVE ADDRESS.**

1. REPORT DATE	2. REPORT TYPE	3. DATES COVERED
AUGUST 2020	Annual	15 Jul 2019 - 14 Jul 2020

4. TITLE AND SUBTITLE

Early Detection of Lung Cancer Through Molecular Analyses of Single Extracellular Vesicle

5a. CONTRACT NUMBER
W81XWH-19-1-0194

5b. GRANT NUMBER

5c. PROGRAM ELEMENT NUMBER

6. AUTHOR(S)
Hakho Lee, PhD; Miles A. Miller, PhD

E-Mail: hlee@mgh.harvard.edu; mmiller29@mgh.harvard.edu

5d. PROJECT NUMBER

5e. TASK NUMBER

5f. WORK UNIT NUMBER

7. PERFORMING ORGANIZATION NAME(S) AND ADDRESS(ES)

MASSACHUSETTS GENERAL HOSPITAL, THE SUSAN ROUDEBUSH
5 FRUIT ST, BOSTON MA 02114-2621

AND ADDRESS(ES)

8. PERFORMING ORGANIZATION REPORT NUMBER

9. SPONSORING / MONITORING AGENCY NAME(S) AND ADDRESS(ES)

U.S. Army Medical Research and Development Command
Fort Detrick, Maryland 21702-5012

10. SPONSOR/MONITOR'S ACRONYM(S)

11. SPONSOR/MONITOR'S REPORT NUMBER(S)

12. DISTRIBUTION / AVAILABILITY STATEMENT

Approved for Public Release; Distribution Unlimited

13. SUPPLEMENTARY NOTES

14. ABSTRACT

The overall goal of this project is to advance a new analytical platform tailor-designed to probe single extracellular vesicles (EVs). Specifically, we will develop a new imaging method to probe individual EVs – the imaging method will use novel cleavable light-tagged antibodies for repeated probing on same EVs. We will next apply this platform to study EVs at very early stages of lung cancers (LCs) using gold standard genetically engineered mouse models of cancer that naturally arise following genetic mutation in the lung tissue, similar to what may occur in humans. We will monitor both tumor burdens and its molecular characteristics; this information will be compared with single-EV profiling results. The study will work backwards from advanced disease towards increasingly minimal disease, with concordant EV analysis and imaging to understand limits of detection.

15. SUBJECT TERMS
lung cancer, extracellular vesicles, imaging, microfluidics

16. SECURITY CLASSIFICATION OF:			17. LIMITATION OF ABSTRACT	18. NUMBER OF PAGES	19a. NAME OF RESPONSIBLE PERSON
a. REPORT	b. ABSTRACT	c. THIS PAGE			19b. TELEPHONE NUMBER *(include area code)*
Unclassified	Unclassified	Unclassified	Unclassified	38	

Standard Form 298 (Rev. 8-98)
Prescribed by ANSI Std. Z39.18

Table of Contents

Page

1. INTRODUCTION

Cancer-derived extracellular vesicles (EVs) are an emerging new class of cancer biomarker. Most types of cancer shed EVs that carry molecular information about the parent tumor, providing a new avenue to probe and serially monitor tumor molecular status. Technical challenges, however, remain when using EVs for early cancer detection: tumor-derived EVs comprise a small fraction of total vesicles in circulation, whereas currently available EV assays are based on bulk measurements, requiring >10^4 tumor-derived EVs per biomarker. Such assays may fail to differentiate true tumor signal from biological background and miss unique molecular signature pertaining to tumor heterogeneity and phenotypic changes occurring tumor development. Responding to these challenges, the overall goal of this project is to advance a new analytical platform for screening or early detection of lung cancer (LC). We have two objectives. *Technical advances.* We will develop a new platform technology for single EV analysis with multiplexing (SEAM). Specifically, we will adopt a cycling imaging method that will allow for multiplexed protein profiling of individual EVs. *Integration with high-resolution tumor imaging.* We will apply the developed SEAM platform to detect circulating EVs at very early stages of LC. We will use gold standard genetically engineered mouse models (GEMMs) of autochthonous lung adenocarcinoma. Total tumor burden and its molecular composition will be assessed by applying single-cell resolution imaging; this information will be correlated with EV molecular profiles obtained via SEAM.

2. KEYWORDS

Lung cancer, Extracellular vesicles, Imaging, Microfluidics, Early detection

3. ACCOMPLISHMENTS

What were the major goals of the project?

The major goals of the first-year funding period (2019/07 - 2020/07) were three-fold.

Goal 1: Optimize SEAM assay (100% completion)

Goal 2: Apply SEAM to profile EVs derived from LC cell lines (80% completion)

Goal 3: Conduct EV profiling study in mouse LC model (25% completion)

What was accomplished under these goals?

We have made significant progresses in developing the SEAM technology and profiling EVs derived from LC cell lines.

Major Task	Timeline (Months)	Completion
Major Task 1: Optimize SEAM assay	1-6	100%
Major Task 2: Apply SEAM to profile EVs derived from LC cell lines	7-14	80%
Major Task 3: Conduct EV profiling study in mouse LC model	1-21	25%
Major Task 4: Conduct EV profiling study in LC patient samples	12-24	(Year 2)

Task 1.1. Prepare fluorescent detection probes. To analyze more than three markers simultaneously, antibodies were conjugated with complementary fluorochromes including Alexa Fluor 488, Alexa Fluor 555 and Alexa Fluor 647. Because these fluorochromes can be quenched by injecting an oxidation buffer, we can use a cycling imaging method for multiplexed fluorescence imaging. We have selected EV-enriched markers (*i.e.*, CD9, CD63, CD81) and LC related markers (*i.e.*, EpCAM, EGFR, ALK, MET, MUC1, HER2, ADAM10, NCAM1, FN, VIM) based on screening LC biomarker databases. In addition, we extracted three markers (*i.e.*, SDC1, CTSB, CTSH) as candidates of early LC marker from RNA sequencing data that mouse lung tumors (*i.e.*, KP tumors) are sequenced at early and late stage of progression. We have validated fluorescent detection probes using immunofluorescence image (**Fig. 1a**) and flow cytometry of LC cell lines (**Fig. 1b**). The protein expression levels of 16 protein markers were measured from two human LC cell lines (H2228, A549) and one mouse LC cell line (KP1.9) using flow cytometry.

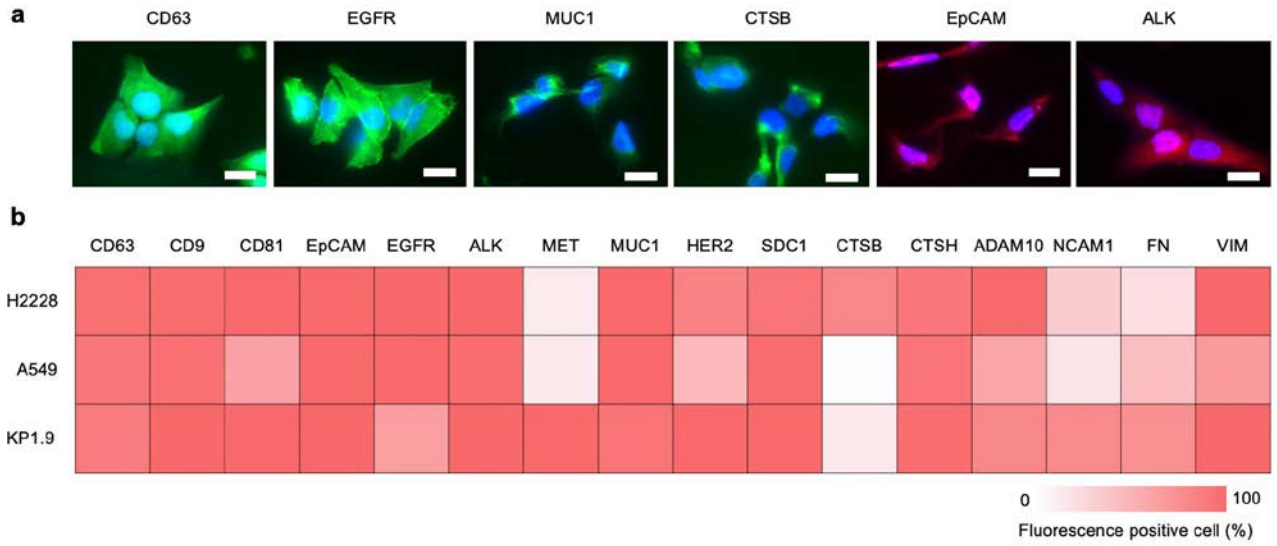

Fig. 1: Probe validation using LC cell lines. (a) Fluorescent detection probes of LC markers were validated using immunofluorescence images. Scale bar, 10 μm. **(b)** 16 protein markers were selected and protein expression levels were measured from three different LC cell lines (H2228, A549, KP1.9) using flow cytometry.

Task 1.2. Implement imaging devices. We have isolated EVs from three lung adenocarcinoma cell lines (H2228, A549, KP1.9). The average hydrodynamic size and zeta potential of EV were measured using dynamic light scattering (DLS). We obtained the pure vesicles in the size range of 50-200 nm (**Fig. 2a**) using our established protocol. EVs showed a net negative surface charge (**Fig. 2b**). We then have optimized a microfluidic system for EV capture and staining. For universal EV identification, we labeled the EV with N-hydroxysuccinimide ester (NHS-ester) form of Alexa Fluor 555 which can react with amine on the surface of the EV (**Fig. 2c**). For EV capture, the glass surface of the microfluidic chamber was modified with (3-aminopropyl)triethoxysilane (APTES) (**Fig. 2d**). Negatively charged EV surfaces could be immobilized due to an electrostatic interaction. EVs then could be permanently captured following glutaraldehyde treatment and subsequent reaction with amines on the surface of the EVs. We tested EV capture using fluorescence image.

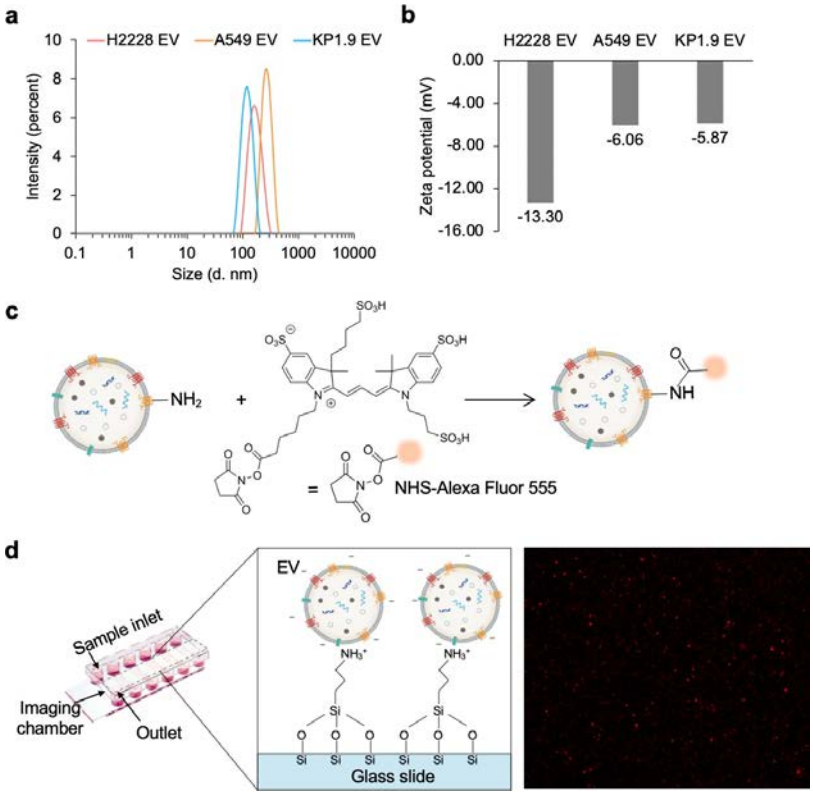

Fig. 2: Microfluidic for EV capture. (a) LC EVs (< 200 nm) were collected from two human LC cells and one mouse LC cell. **(b)** The surface charge of EV showed negative. **(c)** EV was labeled with NHS-Alexa Fluor 555 for their identification. **(d)** For EV capture and staining, the glass surface of microfluidic chamber was modified with APTES, which has positive charge in PBS buffer condition (pH=7.4). Captured EVs were observed using fluorescence image.

Task 2.1. EV profiling from different cell lines. We performed single EV image analysis (**Fig. 3a**). To analyze colocalization of fluorescent dyes from a batch of images, we used CellProfiler software. Based on image analysis, we found out colocalization% and then observed marker positive EVs (%) in the filed of view (**Fig. 3b**). In order to confirm

the tetraspanin expression of entire EVs, we also measured human LC EVs using flow cytometry. To allow detection of EVs in conventional cytometers, EVs were coupled to 3 μm diameter aldehyde-sulfate latex beads. These can then be antibody labeled and applied to conventional flow cytometry protocols. In H2228 EVs, the expression levels of CD63, CD9, and CD81 were 80, 73, and 54%, respectively (**Fig. 3c**).

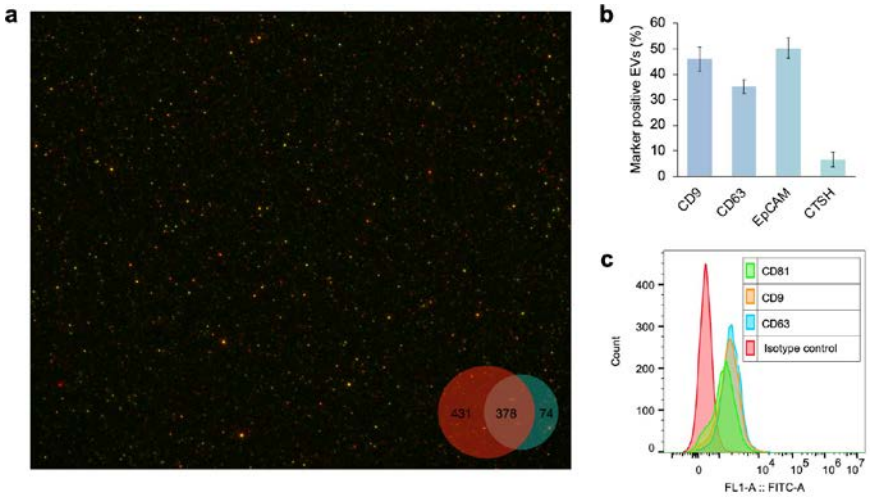

Fig. 3: EV profiling of H2228 LC. (a) Single EV image analysis was performed for tetraspanin CD9 detection. **(b)** Marker positive EVs (%) were analyzed using CellProfiler. **(c)** Tetraspanins expression of EVs were measured using flow cytometry.

Task 3.1. & Task 3.2. ACURO approval. We had submitted documents for local IACUC review and ACURO review. We received ACURO approval to conduct EV profiling study in mouse LC model.

Task 3.3. EV profiling in mouse models. We have generated mouse LC models based on KP1.9 and collected mouse plasma EVs for profiling. KP1.9 cells are clonally derived from the GEMM based on induced *Kras^{G12D}p53$^{-/-}$* mutation.

What opportunities for training and professional development has the project provided?

Training activities.

Single EV analysis and microfluidics. Dr. Cho was trained for the single EV analysis and microfluidics. This training was expedited through work with an expert research fellow (Dr. Ala Jo).

In vivo LC modeling and sample processing. To conduct in vivo experiment, Dr. Cho completed CITI Program and CCM Orientation course in the HealthStream Learning Center. With the guidance of the Sr. research technologist (Mrs. Guiles (Iwamoto), Yoshiko), Dr. Cho was trained for fluorescence microscope as well as dissecting, harvesting, and embedding mouse organs. Dr. Cho also collaborated with Dr. Nuri Oh at CSB for in vivo LC modeling and sample processing.

Professional development.

Presentation. Dr. Cho presented at the CSB Biomedical Engineering meetings and participated in weekly Prof. Lee and Prof. Miller group meetings.

How were the results disseminated to communities of interest?

Some of our preliminary progress was presented in part at HMS Bioinformatics and Integrative Genomics (BIG) PhD Program (2019) and Brigham and Women's Joint Program in Nuclear Medicine (2020). We will present the results in Year 2.

What do you plan to do during the next reporting period to accomplish the goals?

As planned in our original Aim 1 and Aim 2, we will apply SEAM platform to analyze circulating EVs in patients and mouse models of LC, and perform EV profiling following therapeutic treatment. In mouse LC models, total tumor burden and its molecular composition will be assessed by applying both translational macroscopic (μ-CT) and ex vivo microscopic (CUBIC whole-organ confocal microscopy) lung imaging. This information will be correlated with molecular profile of plasma EV obtained via SEAM. We will use SEAM to detect circulating EVs at very early stages of LC in well-studied, controlled, and genetically defined LC models. We will apply SEAM to a cohort of clinical plasma samples taken from LC patients (n = 5) and patients with non-malignant lung disease (n = 5) as a proof of principle.

4. IMPACT

What was the impact on the development of the principal discipline(s) of the project?
This project could promote both fundamental and clinical research into EVs and early biomarker detection. The developed SEAM technology enable *multiplexed molecular screening on individual vesicles* based on the cyclic imaging. This characteristic allows for revealing hidden molecular phenotypes in LC EVs, which would have implications in early cancer detection, cancer classification, and resistance monitoring. *Molecular profiles of LC-specific EVs* is a significant step forward to promote EVs' clinical use. Because EVs can be obtained safely and repeatedly by collecting serial blood samples undergoing therapeutic treatment, serial EV monitoring could be non-invasive means for diagnostics, evaluation of treatment or surgical efficacy and monitoring of recurrence. Multiplexed EV characterization could be valuable in developing novel diagnostic and intervention strategies (e.g., targeted molecular therapy, immunotherapy) by allowing for better powered trials, improved tumor detection / monitoring, and rational selection and timing of therapies.

What was the impact on other disciplines?
Nothing to report.

What was the impact on technology transfer?
Nothing to report.

What was the impact on society beyond science and technology?
Nothing to report.

5. CHANGES/PROBLEMS

Nothing to report.

6. PRODUCTS

Publications, conference papers, and presentations

Journal publications.

Van Deun J, Jo A, Li H, Lin HY, Weissleder R, Im H, Lee H (2020) Integrated Dual-Mode Chromatography to Enrich Extracellular Vesicles from Plasma. Adv Biosyst e1900310. PMID:32351054

Weissleder R, Lee H (2020) Automated molecular-image cytometry and analysis in modern oncology. Nature Reviews Materials 5:409-422. DOI:10.1038/s41578-020-0180-6

Huang CH, Park YI, Lin HY, Pathania D, Park KS, Avila-Wallace M, Castro CM, Weissleder R, Lee H (2019) Compact and Filter-Free Luminescence Biosensor for Mobile in Vitro Diagnoses. ACS Nano 13:11698-11706. PMID:31461265

Presentations

2019	Oral Seminar, Miles Miller, HMS Bioinformatics and Integrative Genomics (BIG) PhD Program
2020	Oral Seminar, Miles Miller, Brigham and Women's Joint Program in Nuclear Medicine

Technologies or techniques.
Nothing to report.

Other Products
Nothing to report.

7. PARTICIPANTS & OTHER COLLABORATING ORGANIZATIONS

What individuals have worked on the project?

Name:	*Hakho Lee*
Project Role:	*Principal Investigator*
Researcher Identifier	*orcid.org/0000-0002-0087-0909*
Nearest person month worked:	*2*
Contribution to Project:	*Dr. Lee supervised the overall research, interacting with investigators and research fellows, and discussing all experimental designs and data.*
Funding Support:	*W81XWH-14-1-0279*

Name:	*Miles A. Miller*
Project Role:	*Co-Principal Investigator*
Researcher Identifier	*orcid.org/0000-0001-7638-8898*
Nearest person month worked:	*1*
Contribution to Project:	*Dr. Miller guided the biological research, identifying biomarkers for lung cancer detection, and discussing all experimental designs and data.*
Funding Support:	*W81XWH-14-1-0279*

Name:	*Ralph Weissleder*
Project Role:	*Investigator*
Researcher Identifier	*orcid.org/0000-0003-0828-4143*
Nearest person month worked:	*1*
Contribution to Project:	*Dr. Weissleder provided scientific assistance on the development of molecular probes and their validation, translational research and early phase clinical trials, and commercialization of technology. He also granted full access to technologies available in his laboratory.*
Funding Support:	

Name:	*Cesar M. Castro*
Project Role:	*Investigator*
Researcher Identifier	*orcid.org/0000-0002-1159-5658*
Nearest person month worked:	*1*
Contribution to Project:	*Dr. Castro guided the biological research, identifying biomarkers for lung cancer detection.*
Funding Support:	

Name:	*Mi Hyeon Cho*
Project Role:	*Research fellow*
Researcher Identifier	*orcid.org/0000-0001-9429-4692*
Nearest person month worked:	*12*
Contribution to Project:	*Dr. Cho optimized SEAM assay, analyzed LC EVs derived from LC cell lines and mouse plasma.*
Funding Support:	*W81XWH-14-1-0279*

Has there been a change in the active other support of the PD/PI(s) or senior/key personnel since the last reporting period?
Nothing to report.

What other organizations were involved as partners?
Nothing to report.

8. SPECIAL REPORTING REQUIREMENTS

Not applicable.

9. APPENDICES

ADVANCED BIOSYSTEMS
www.adv-biosys.or

Integrated Dual-Mode Chromatography to Enrich Extracellular Vesicles from Plasma

*Jan Van Deun, Ala Jo, Huiyan Li, Hsing-Ying Lin, Ralph Weissleder, Hyungsoon Im, and Hakho Lee**

Purifying extracellular vesicles (EVs) from complex biological fluids is a critical step in analyzing EVs molecularly. Plasma lipoprotein particles (LPPs) are a significant confounding factor as they outnumber EVs >10^4-fold. Given their overlap in size, LPPs cannot be completely removed using standard size-exclusion chromatography. Density-based separation of LPPs can be applied but is impractical for routine use in clinical research and practice. Here a new separation approach, known as dual-mode chromatography (DMC), capable of enriching plasma EVs, and depleting LPPs is reported. DMC conveniently integrates two orthogonal separation steps in a single column device: i) size exclusion to remove high-density lipoproteins (HDLs) that are smaller than EVs; and ii) cation exchange to clear positively charged ApoB100-containing LPPs, mostly (very) low-density lipoproteins (V)LDLs, from negatively charged EVs. The strategy enables DMC to deplete most LPPs (>97% of HDLs and >99% of (V)LDLs) from human plasma, while retaining EVs (>30% of input). Furthermore, the two-in-one operation is fast (15 min per sample) and equipment-free. With abundant LPPs removed, DMC-prepared samples facilitate EV identification in imaging analyses and improve the accuracy for EV protein analysis.

Extracellular vesicles (EVs) are important disease biomarkers;[1] they are ubiquitously present in bodily fluids and carry molecular cargo from their respective parental cells (e.g., transmembrane and intracellular proteins, mRNA, DNA, and microRNA).[2] EVs thus can serve as a blood-based analytical method to obtain and monitor diseases' molecular traits,[3] promoting better-informed clinical decisions. Indeed, EVs were found superior to conventional protein markers for tumor detection.[4–6] Key mutations (e.g., EGFRvIII, IDH1R132H, $EGFR^{T790M}$) have also been detected in EVs.[6,7] Essential to diagnostic EV analysis is the ability to perform a given molecular test in true EV fractions, rather than in contaminated mixtures. In other words, EVs exist in complex heterogeneous matrices (**Figure** 1a) and retrieving pure vesicle populations is a pivotal first assay step.

Among various EV isolation strategies,[1] size-exclusion chromatography (SEC) is increasingly adopted as a preferable isolation method for clinical samples, considering its low cost, much faster turnaround time compared to ultracentrifugation, and ease-of-operation.[8] SEC separates analytes based on their differential retention time in porous gels. When applied to plasma or serum, SEC produces well-defined vesicle fractions with most soluble proteins removed.[9] The current approaches, however, often fail to differentiate EVs from certain types of lipoprotein particles (LPPs), predominantly (very) low-density lipoproteins (V)LDL, due to size overlap.[10] With LPPs ($\approx 10^{15}$ particles mL^{-1})[11] significantly outnumbering EVs ($\approx 10^7$–10^9 particles mL^{-1} in healthy individuals),[12] SEC-prepared samples are susceptible to artifacts, including overestimation of actual EV counts, steric hindrance in immunoassays, and increased biological noise. This is especially important in the discovery phase of EV protein biomarkers, as the abundance of LPPs can confound the search for less-abundant EV-associated proteins. Density-gradient ultracentrifugation can be incorporated before or after SEC to separate EVs from LPPs but the combined process negates SEC's practical advantages.

Here, we report a substantially improved chromatography method for rapid EV isolation from plasma samples. We noticed the contrast in surface charge properties between EVs, that are negatively charged,[13] and ApoB100-containing

Dr. J. Van Deun, Dr. A. Jo, Dr. H. Li, Dr. H.-Y. Lin, Prof. R. Weissleder, Prof. H. Im, Prof. H. Lee
Center for Systems Biology and Department of Radiology
Massachusetts General Hospital
Harvard Medical School
Boston, MA 02114, USA
E-mail: hlee@mgh.harvard.edu
Prof. R. Weissleder
Department of Systems Biology
Harvard Medical School
Boston, MA 02114, USA
Prof. H. Lee
Center for NanoMedicine
Institute for Basic Science (IBS)
Seoul 03722, Republic of Korea
Prof. H. Lee
Yonsei-IBS Institute
Yonsei University
Seoul 03722, Republic of Korea
The ORCID identification number(s) for the author(s) of this article can be found under https://doi.org/10.1002/adbi.201900310.

DOI: 10.1002/adbi.201900310

 © 2020 WILEY-VCH Verlag GmbH & Co. KGaA, Weinheim

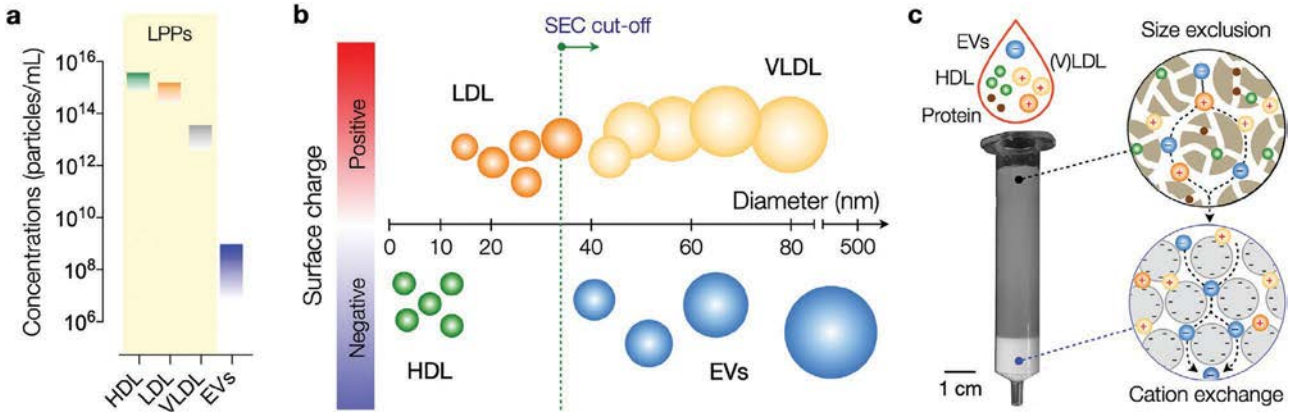

Figure 1. Rationale and principle of the dual-mode chromatography. a) Typical concentrations of lipoprotein particles (LPPs) and extracellular vesicles (EVs) in human plasma. LPP numbers are considerably higher (>104) than EV numbers and also fluctuate during the day. HDL, high-density lipoprotein; LDL, low-density lipoprotein; VLDL, very low-density lipoprotein. b) Schematic representation of the most common particle species found in plasma, discriminated by size and surface charge. Note that EVs overlap in size with (V)LDL, but have opposite surface charge. Green dotted line indicates a commonly used cut-off for size-exclusion chromatography (SEC) that separates EVs from other particles. c) Design of dual-mode chromatography (DMC) column. The device has two separation layers in tandem: size exclusion (top) and cation exchange (bottom). The top layer is used to filter out small analytes, including soluble proteins and HDL particles. Filtrates then enter the cation exchange layer where positively charged particles (e.g., LDL, VLDL) are captured. The resulting sample is depleted from LPPs and enriched in EVs.

LPPs, which carry an abundance of positive charges.[14] While previous work to discriminate EVs and LPPs predominantly focused on size and/or density, we reasoned that these charge discrepancies could be exploited for better particle separation (Figure 1b). Indeed, ApoB100 lipoproteins are known to interact with glycosaminoglycans on the arterial wall in vivo,[15] which has led to the use of polymers bearing sulfate groups for plasmapheresis[16] or general lipoprotein isolation.[17] We thus explored combining ion exchange in tandem with size-exclusion chromatography to obtain an LPP-depleted EV population. The strategy allowed us to remove the majority of plasma LPPs, >97% of high-density lipoprotein/HDL and >99% of (V)LDL, while maintaining a relatively high EV isolation yield comparable to that of SEC. We also constructed a layered monolithic device, termed a DMC (dual-mode chromatography) column, to perform orthogonal separations through a one-time sample loading. This one-time loading approach is particularly important compared to sequential separation strategies as it minimizes loss of rare EV fractions. DMC operation was simple, fast (15 min per sample) and equipment-free. Furthermore, DMC-prepared samples led to better analytical outcomes in single vesicle imaging and EV protein analyses.

The DMC column consists of a top, size-exclusion layer and a bottom, cation exchange layer (Figure 1c). The top layer separates small analytes (e.g., soluble proteins, protein aggregates, HDL) from larger particles through differential retention time. The bottom layer receives filtrates from the top and captures positively charged (V)LDL particles. For the top layer, we used a conventional SEC resin (Sepharose CL-4B, exclusion limit ≈35 nm). The resin volume was 10 mL, identical to that of gravity-driven SEC columns commonly used for EV isolation.[8,9]

To determine an optimal material for (V)LDL capture, we compared a panel of resins with varying functional groups and physical characteristics. We made cation exchange columns, each packed (2 mL) with a single resin type. Test samples were prepared by filtering human plasma through SEC and collecting the EV-enriched fractions (see the Experimental Section), enriching for (V)LDL and EVs. We then processed these fractions with the cation exchange columns, assessing each column's ability to remove (V)LDL by measuring ApoB100. Fractogel EMD SO_3^- was found to be most efficient, removing up to 70-fold more ApoB100 than other tested resins (Figure S1a,b, Supporting Information), possibly due to its "tentacle" structure which promotes interaction between resin and target.[18] The final removal efficiency of ApoB100 was ≈98%. Doubling the resin volume (to 4 mL) resulted in only a minor improvement in efficiency (Figure S1c, Supporting Information). The final DMC thus had the following dual layer structure: Sepharose (10 mL, top) and Fractogel (2 mL, bottom).

We characterized the DMC column performance and compared it to a standard SEC column. We started by assessing EV recovery ratio. EV-only samples (cell-line derived EVs in a buffer) were passed through the columns and EV counts before versus after separation were measured via nanoparticle tracking analysis (NTA; **Figure** 2a). EV recovery ratios were in the same order of magnitude: 0.34 (DMC) and 0.78 (SEC). DMC's slightly lower value could be attributed to its longer filtering path. We next measured the capacity for LPP removal and EV enrichment by DMC and SEC columns. We mimicked "clinical samples" by spiking human plasma (0.5 mL) samples with EVs (≈10^{10} mL^{-1}) from cancer cell lines (Experimental Section). Representative lipoprotein markers were ApoA1 for HDL and ApoB100 for (V)LDL, while CD63 was chosen as EV marker. We observed a significant reduction in ApoB100 after DMC separation (Figure 2b). When an equal amount (≈18 μg) of SEC and DMC sample proteins were analyzed, ApoA1 levels were found to be similar (Figure 2c), which may reflect the same HDL depletion mechanism (size exclusion) in both columns. CD63 level, however, was markedly higher in the DMC filtrate (Figure 2c) due to efficient ApoB100 removal. Figure 2d summarizes the calculated LPP removal efficiency. DMC and SEC columns both effectively cleared HDL particles from

© 2020 WILEY-VCH Verlag GmbH & Co. KGaA, Weinheim

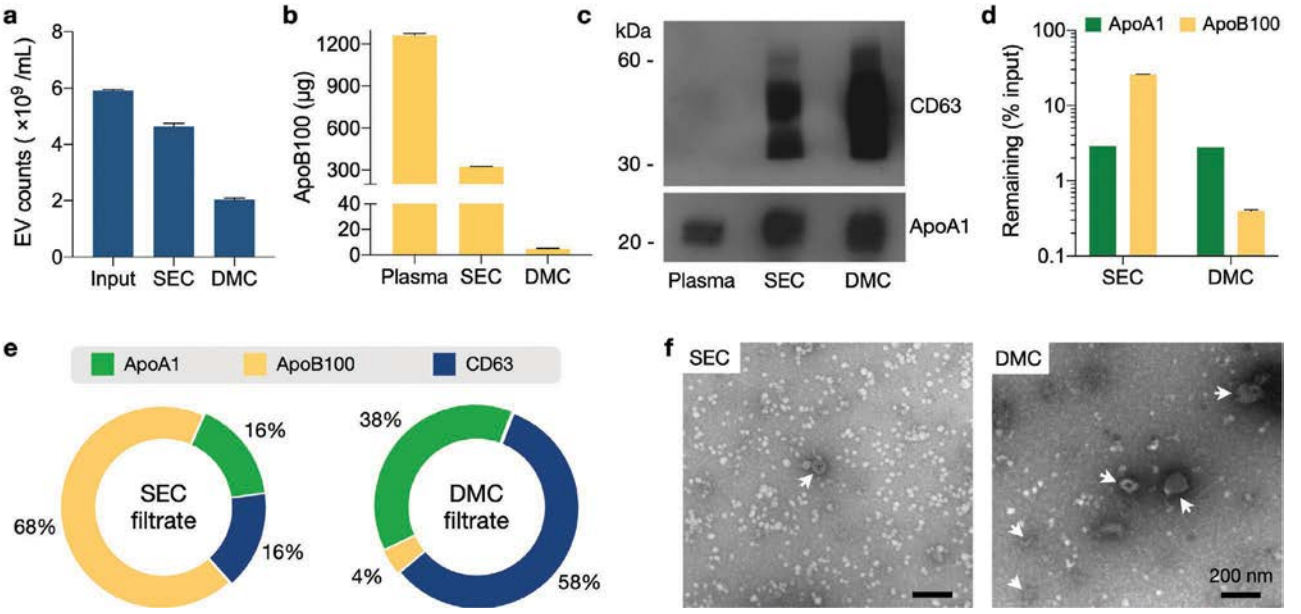

Figure 2. DMC characterization. a) EV recovery was estimated using samples with a known number of cell-line derived EVs in PBS (input). Equal amount of samples were passed through a SEC or DMC column, and particle numbers after preparation were measured via nanoparticle tracking analysis (NTA). Recovery ratios were 78% (SEC) and 34% (DMC). Data from technical triplicates are displayed as mean ± s.d. b) DMC and SEC columns were used to process mock clinical samples which were human plasma spiked with cell-line derived EVs. Most ApoB1 proteins were removed by DMC. Data from technical duplicates are displayed as mean ± s.d. c) The same amount of plasma and EV sample proteins from (b) were analyzed. ApoA1 levels were comparable between SEC and DMC. CD63 was significantly enriched in DMC samples. d) Capacity for LPP removal by DMC and SEC were compared. ApoA1 (HDL) and ApoB100 (VLDL and LDL) contents were measured before and after filtration of human plasma (0.5 mL). Both DMC and SEC showed a similar efficiency (≈97%) in ApoA1 depletion. For ApoB100 removal, DMC (efficiency: 0.4%) significantly outperformed SEC (25%). Data from technical duplicates are displayed as mean ± s.d for ApoB100. ApoA1 quantification was based on band intensity from Western blotting. e) Relative mass-ratios of ApoA1, ApoB100, and CD63 were estimated in SEC and DMC filtrates. (V)LDL was the major vesicle population in the SEC filtrate, whereas EVs were the dominant component in the DMC-prepared sample. f) Transmission electron micrographs of SEC- and DMC-prepared human plasma. EVs (arrowheads) were negatively stained; LPPs appeared white. Note LPP reduction and EV enrichment in the DMC sample. Close-up images are provided in Figure S2 (Supporting Information).

plasma, with an efficiency of ≈97%. For (V)LDL particles, however, DMC was far superior to SEC: only 0.4% of ApoB100 in the input plasma remained after the DMC filtering, whereas the number was ≈25% with the SEC column.

Based on these data, we estimated the relative mass ratio of the most significant proteins in SEC- or DMC-prepared samples. Figure 2e show the relative mass fraction of ApoA1, ApoB100, and CD63; the amount of each protein target was estimated from ELISA or Western blotting, and was normalized against the sum of these three proteins. EV protein (CD63) was the dominant fraction (>80%) in the DMC sample, while HDL and (V)LDL were largely removed. The reverse trend was observed in the SEC sample, with LPPs being the major component. Electron microscopy confirmed these observations (Figure 2f and Figure S2, Supporting Information). DMC-prepared plasma samples contained more EVs and less LPPs than SEC samples. Indeed, overall protein analysis by SDS-PAGE followed by Coomassie blue staining revealed differences in protein profile between these two samples (Figure S3a, Supporting Information). In agreement with lipoprotein particle removal, overall cholesterol levels were found to be ≈5 times less in DMC samples (Figure S3b, Supporting Information). As a consequence of lipoprotein removal, DMC-prepared samples appear much clearer than SEC samples (Figure S3c, Supporting Information).

We also noticed a potential pitfall when interpreting NTA data for plasma EV numbers. After SEC or DMC preparation, we found that NTA particle counts were directly proportional to ApoB100 amounts in samples (Figure S4a, Supporting Information). This result strongly suggests the majority of counted particles could actually be (V)LDLs rather than EVs. Western blotting supported this observation. When we analyzed SEC and DMC samples with the same NTA particle counts, we saw negligible CD63 and low ApoA1 levels in the SEC samples (Figure S4b, Supporting Information). Simply counting particle numbers in SEC filtrates, without any molecular specificity, thus can lead to overestimation of EV numbers, even by as much as an order of magnitude. By extension, this implies that calculating particle/protein ratio for estimating EV purity might be less suitable for plasma-derived samples.[19]

We hypothesized that removing LPP contamination increases the accuracies in EV immunoassays by lowering biological background noise. To test this hypothesis, we processed universal human samples using DMC and SEC columns, and subjected filtered samples to two different analytical modalities, single particle imaging[20] and the integrated magneto-electrochemical exosome (iMEX) assay.[5] For single EV imaging, we used a lipophilic dye to stain overall lipid particle populations and a fluorophore-conjugated anti-CD63 antibody for EV labeling (**Figure** 3 and Figure S5, Supporting Information). The SEC-only sample

© 2020 WILEY-VCH Verlag GmbH & Co. KGaA, Weinheim

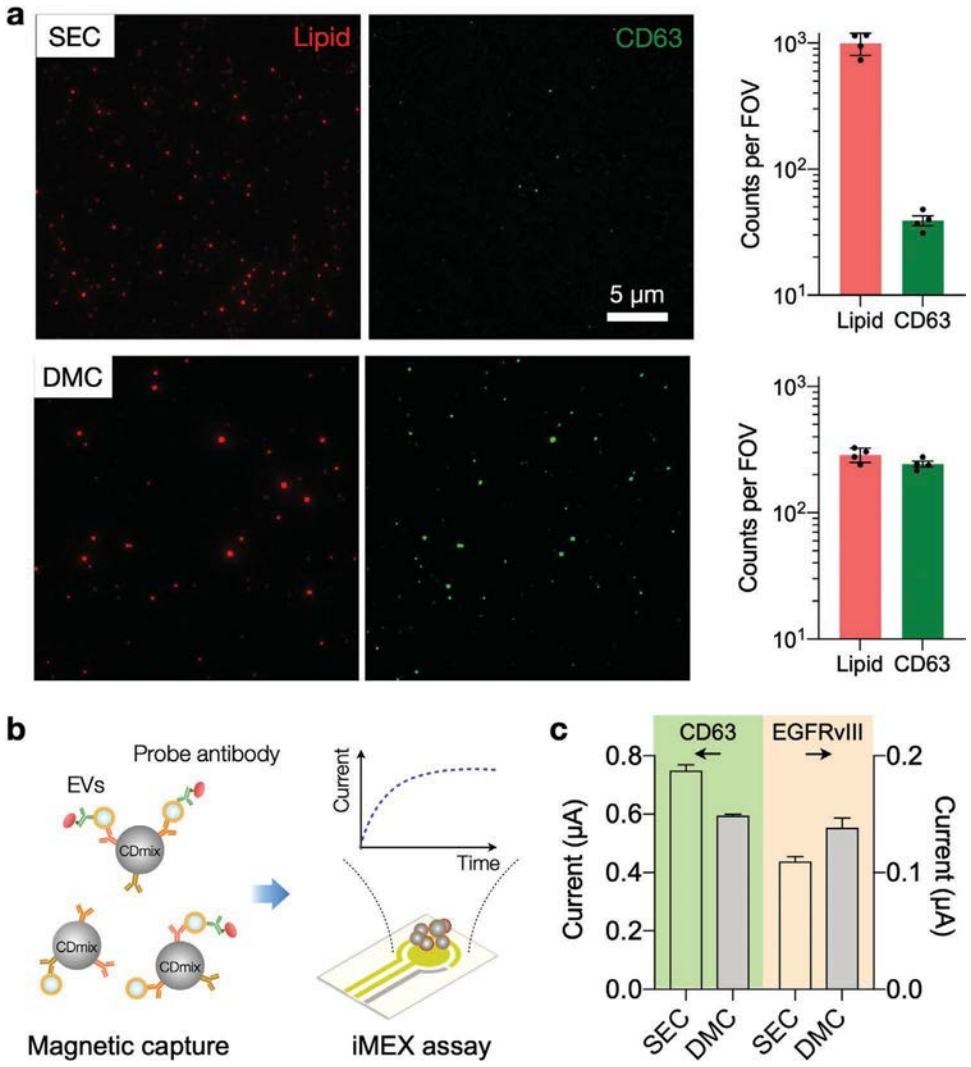

Figure 3. EV assays with DMC and SEC samples. a) Single particle imaging. SEC and DMC samples were labeled with the general lipid dye (red) and fluorescent CD63 antibodies (green). The SEC sample contained a large number of lipid particles per field-of-view (FOV, 77 × 65 μm^2), but few of them were CD63-positive (top row). The DMC sample, in contrast, was enriched with CD63-positive lipid particles (bottom row). The graphs show particle counts (mean ± s.d.) from four FOVs. b) Integrated magneto-electrochemical exosome (iMEX) EV protein assay. EVs are captured on magnetic beads based on EV-specific surface markers (CD63, CD81, and CD9) and further labeled with probe antibodies to detect target protein markers. Probe antibodies, conjugated with oxidizing enzymes, generate electrical currents through electrochemical reaction. c) Human plasma was spiked with EVs from Gli36 EFGRvIII mutation. Following SEC or DMC preparation, samples were assessed for CD63 and EGFRvIII expression via iMEX. The DMC sample showed a slightly lower CD63 signal than SEC, reflecting lower EV recovery. EGFRvIII signal, however, was higher in the DMC sample, presumably due to reduced interference from biological background. The data are from technical duplicates and displayed as mean ± s.d.

had a large lipid particle population but only a small fraction (≈4%) of them were CD63-positive (Figure 3a, top). In contrast, the DMC sample was less crowded but more lipid particles (≈85%) were CD63-positive; this led to robust EV identification and counting (Figure 3a, bottom). Note that EV-free controls showed no measurable signal in both fluorescent channels after labeling (Figure S6, Supporting Information).

We next used the iMEX assay to measure EV surface protein levels in SEC and DMC samples. We prepared test samples by spiking human plasma (1 mL) with EVs (≈10^{10} mL^{-1}) from a human glioblastoma cell line (Gli36 with EGFRvIII overexpression). Aliquots (0.5 mL) were processed with either SEC or DMC. To capture EVs, we used magnetic beads specific to tetraspanins (CD63, CD81, and CD9). Bead-EV complexes were then further labeled probing antibodies (CD63 or EGFRvIII) for signal generation (Figure 3b). The iMEX results (Figure 3c) showed that CD63 levels effectively followed the EV recovery ratio of SEC and DMC (Figure 2a), whereas EGFRvIII signal was more pronounced in the DMC sample. This observation may result from differences in target molecule concentrations. CD63 level in plasma would be higher than that of EGFRvIII, which makes CD63 detection less affected by biological background (i.e., LPPs); for the less abundant EGFRvIII, removing interfering LPPs makes the analytical signal more robust.

In summary, we developed a new, single-step chromatography approach for EV enrichment, DMC, and evaluated its

© 2020 WILEY-VCH Verlag GmbH & Co. KGaA, Weinheim

performance with plasma, the most commonly used bodily fluid for EV analyses. DMC effectively removed most plasma LPPs: >97% HDL, similar to SEC; and >99% (V)LDL, >60-fold more efficient than SEC. Consequently, DMC produced enriched EV population and improved analytical outcomes of EV immunoassays with lower biological background. We envision further investigations with different biofluids (e.g., CSF, saliva) and analytical modalities (e.g., nucleic acid detection) to broaden DMC's applicability. Such efforts would further confirm DMC as a powerful EV preparation strategy that can seamlessly replace the current SEC-based EV isolation.

Experimental Section

Plasma: The sodium-EDTA plasma was acquired from Rockland Immunochemicals, Inc.

Size-Exclusion Chromatography and Dual-Mode Chromatography: Sepharose CL-4B (GE Healthcare), Fractogel EMD SO_3^- (M) (Millipore Sigma), Capto S (GE Healthcare) and SP Sepharose Fast Flow (GE Healthcare) resins were washed three times with PBS buffer. A nylon net with 11 μm pore size (NY1102500, Millipore Sigma) was placed on the bottom of a 10 mL syringe (BD Biosciences). For the SEC column, this was followed by stacking of 10 mL washed Sepharose. For the DMC column, 2 mL of ion exchange resin was stacked first, followed by careful layering of 10 mL Sepharose on top. After adding 0.5 mL plasma sample, individual fractions of 1 mL eluate were collected. EV-containing fractions (first 2 fractions after the void volume, which was 3 mL for SEC and 3.8 mL for DMC) were pooled and concentrated using Amicon Ultra-2 10K filters (Millipore Sigma).

EV Preparation for Spike-In Experiments: ES-2 cells and Gli36 cells carrying an EGFRvIII overexpression (Gli36 EGFRvIII) were cultured in DMEM supplemented with 10% fetal bovine serum. Cells were washed 3 times with serum free medium and cultured in DMEM supplemented with 1% EV-depleted FBS (Invitrogen) for 24 h. Conditioned medium (CM) from $\approx 2 \times 10^8$ cells was collected and centrifuged at 300 g (10 min) and 2000 g (20 min). Next, CM was concentrated ≈300 times using a Centricon Plus-70 centrifugal filter device with a 10K nominal molecular weight limit (Millipore Sigma). Subsequently, a discontinuous OptiPrep density gradient (ODG) was constructed as described previously.[21] 1 mL of concentrated CM was overlaid onto the top of the gradient, which was then centrifuged for 18 h at 100 000 *g* and 4 °C (SW 27.1 Ti rotor, Beckman Coulter). Next, fractions of 1 mL were collected from the top of the gradient, with F9 and 10 (density ≈1.1 g mL^{-1}) being pooled and used for subsequent SEC-based separation of EVs from the iodixanol polymer, using Sepharose CL-2B as resin. EV-containing fractions (F4-7) were pooled, concentrated to 100 μL, aliquoted, and stored at −80 °C. In Figures 2b–e and 3a and Figures S3 and S4 (Supporting Information), the results were obtained using plasma samples spiked with ES2 EVs ($\approx 7 \times 10^9$ mL^{-1}); in Figures 2f and 3c, plasma samples spiked with Gli36 EGFRvIII EVs ($\approx 1 \times 10^{10}$ mL^{-1}). To demonstrate bona fide EV isolation, presence of CD9, CD63 and CD81 was analyzed using bead-based flow cytometry (Figure S7, Supporting Information).[22]

Nanoparticle Tracking Analysis (NTA): A NanoSight LM10 microscope (Malvern) equipped with a 405 nm laser was used. Three 30 s videos were recorded of each sample with camera level 15. After each video, the sample was advanced through the chamber to avoid repeated measurement of identical particles in the field of view. Videos recorded for each sample were analyzed with NTA software version 3.2 with detection threshold kept constant at 3. Samples were diluted with PBS buffer until particle concentration was within the linear concentration range of the NTA software (3×10^8–1×10^9 mL^{-1}).

Western Blot and Coomassie blue: EV samples were lysed in 0.2% SDS and protein concentration measured by Qubit assay (Thermo Fisher). Samples were lysed with nonreducing LDS sample buffer (Invitrogen), boiled for 5 min at 95 °C, and loaded on a 5–12% gradient gel (Invitrogen). Proteins were separated by SDS-PAGE, transferred to a nitrocellulose membrane, and immunostained for 1 h with the following antibodies: anti-CD63 (clone H5C6, BD Biosciences, 1:200 dilution) and anti-ApoA1 (clone B-10, Santa Cruz, 1:1000 dilution). HRP-conjugated secondary antibodies were added for 1 h, blots were washed, followed by addition of chemiluminescence substrate (WesternBright Sirius, Advansta). Blots were then developed using autoradiographic films. Films were digitized and quantification of signal intensity was performed using ImageJ. For Coomassie blue staining, gel was stained with SimplyBlue SafeStain (Thermo Fisher) for 1 h at room temperature, followed by destaining overnight in dH_20 at 4 °C. Gel was imaged on a Sapphire Biomolecular Imager (Azure Biosystems).

ELISA: Human Apolipoprotein B Quantikine ELISA Kit (R&D Systems) was used according to manufacturer's instructions. Standards and samples were assayed in duplicate.

Cholesterol Assay: The MyQubit Amplex Red Cholesterol Assay (Thermo Fisher) was used according to manufacturer's instructions.

Electron Microscopy: EV samples (5 μL) were overlaid with Formvar carbon-coated grids and incubated 20 min. Grids were then washed in PBS and fixed for 5 min with 1% glutaraldehyde. Grids were washed in dH_2O and incubated on 2% uranylacetate for 5 min. Excess stain was removed by blotting and grids were air-dried. Images were taken using a Tecnai G² Spirit BioTWIN microscope.

Single EV Imaging: EV-containing SEC and DMC fractions were incubated with CM-DiI (Thermo Fisher Scientific) for 30 min at room temperature. EV-free samples were subjected to the same labeling processes. Dye aggregates were removed by Millex-GV syringe filter (0.22 μm pore size, Millipore Sigma). Filtered EVs were captured on a glass slide. Following 30 min incubation at room temperature, the slide was washed with PBST (PBST buffer containing 0.001% Tween 20). After incubation with fixation buffer (4% formaldehyde) and blocking buffer (Superblock, Thermo Fisher Scientific), EV samples were incubated with anti-human CD63 antibody (Ancell) for 90 min at room temperature. After washing, Alexa Fluor 488-labeled secondary antibody was introduced and incubated for 30 min at room temperature. After final wash steps, fluorescence images were taken with BX-63 upright fluorescent microscope (Olympus) with 40 × objective. Acquisition settings (i.e., objective, exposure time, camera setting, illumination) were kept constant for all images.

iMEX Protocol: Antibodies for EV capture (mouse monoclonal anti-CD63 (clone H5C6, BD Biosciences), CD9 (clone MM2/57, Millipore Sigma) and CD81 (clone 1.3.3.22, Thermo Fisher)) were coupled to Pierce Protein A magnetic beads (Life Technologies) in a ratio of 10 μg of total antibody per 100 μL of beads by overnight incubation at 4 °C with rotation. Beads were washed three times with 500 μL of PBS/0.001% Tween and resuspended in 100 μL of the same buffer. For the iMEX assay, 100 μL of EV samples were mixed with 10 μL of the immunomagnetic bead solution for 15 min at room temperature. After incubation, magnetic beads were separated from the solution with a permanent magnet and re-suspended in 80 μL of PBS (1% BSA). After 5 s of vortexing, the beads were separated and re-suspended in 50 μL of PBS (1% BSA). 10 μL of antibodies of interest (20 μg mL^{-1} in PBS) were added to the solution and the mixture was incubated for 15 min at room temperature. The magnetic beads were separated and washed as described before and re-suspended in 50 μL of PBS (1% BSA). 5 μL of streptavidin-conjugated HRP enzymes (1:100 diluted in PBS) were mixed with the beads for 15 min at room temperature. The magnetic beads were separated and washed as described before and re-suspended in 7 μL of PBS. The prepared bead solution and 20 μL of UltraTMB solution (ThermoFisher Scientific) were loaded on top of the screen-printed electrode. After 3 min, chronoamperometry measurement was started with the electrochemical sensing device. The current levels in the range of 50–55 s were averaged.

Statistical Analysis: All data were displayed as mean ± s.d. from technical replicates. Samples numbers and relevant statistical tests are indicated in figure legends. *P* values < 0.05 were considered statistically significant. GraphPAD Prism (version 8.0) was used for analyses. All relevant data of the experiments were submitted to the EV-TRACK knowledgebase (EV-TRACK ID: EV200025).[23]

© 2020 WILEY-VCH Verlag GmbH & Co. KGaA, Weinheim

Supporting Information

Supporting Information is available from the Wiley Online Library or from the author.

Acknowledgements

A.J., H.Li, and H.-Y.L. contributed equally to this work. The authors thank Dr. Breakefield (Massachusetts General Hospital) for helpful discussion. This work was supported in part by U.S. NIH Grants P01CA069246 (R.W., H.L.), R01CA229777 (H.L.), 1R01CA204019 (R.W.), U01CA233360 (H.L.), T32CA 79443 (H.-Y.L.), W81XWH1910199 (H.L.), DOD-W81XWH1910194 (H.L.); R00CA201248 (H.I.), R21CA217662 (H.I.), P30AG062421 (H.I); Belgian American Educational Foundation fellowship (J.V.D.); MGH Scholar Fund (H.L.), MGH Fund for Medical Discovery Fellowship (H.-Y.L.); the Institute for Basic Science IBS-R026-D1 (H.L.), South Korea. H.Li thanks a postdoctoral fellowship from the Canadian Institutes of Health Research.

Conflict of Interest

The authors declare no conflict of interest.

Keywords

extracellular vesicles, lipoproteins, liquid biopsies

Received: December 31, 2019
Revised: March 26, 2020
Published online:

[1] H. Shao, H. Im, C. M. Castro, X. Breakefield, R. Weissleder, H. Lee, *Chem. Rev.* **2018**, *118*, 1917.

[2] a) M. W. Graner, O. Alzate, A. M. Dechkovskaia, J. D. Keene, J. H. Sampson, D. A. Mitchell, D. D. Bigner, *FASEB J.* **2009**, *23*, 1541; b) J. Skog, T. Wurdinger, S. van Rijn, D. H. Meijer, L. Gainche, M. Sena-Esteves, W. T. J. Curry, B. S. Carter, A. M. Krichevsky, X. O. Breakefield, *Nat. Cell Biol.* **2008**, *10*, 1470; c) L. Balaj, R. Lessard, L. Dai, Y. J. Cho, S. L. Pomeroy, X. O. Breakefield, J. Skog, *Nat. Commun.* **2011**, *2*, 180; d) H. Valadi, K. Ekström, A. Bossios, M. Sjöstrand, J. J. Lee, J. O. Lötvall, *Nat. Cell Biol.* **2007**, *9*, 654.

[3] a) J. Kaiser, *Science* **2018**, *359*, 259; b) K. Pantel, C. Alix-Panabieres, *Cancer Res.* **2013**, *73*, 6384.

[4] a) H. Shao, J. Chung, K. Lee, L. Balaj, C. Min, B. S. Carter, F. H. Hochberg, X. O. Breakefield, H. Lee, R. Weissleder, *Nat. Commun.* **2015**, *6*, 6999; b) K. S. Yang, H. Im, S. Hong, I. Pergolini, A. F. Del Castillo, R. Wang, S. Clardy, C. H. Huang, C. Pille, S. Ferrone, R. Yang, C. M. Castro, H. Lee, C. F. Del Castillo, R. Weissleder, *Sci. Transl. Med.* **2017**, *9*, eaal3226; c) Y. Yoshioka, N. Kosaka, Y. Konishi, H. Ohta, H. Okamoto, H. Sonoda, R. Nonaka, H. Yamamoto, H. Ishii, M. Mori, *Nat. Commun.* **2014**, *5*, 3591; d) P. Zhang, X. Zhou, M. He, Y. Shang, A. L. Tetlow, A. K. Godwin, Y. Zeng, *Nat. Biomed. Eng.* **2019**, *3*, 438; e) C. Liu, J. Zhao, F. Tian, L. Cai, W. Zhang, Q. Feng, J. Chang, F. Wan, Y. Yang, B. Dai, Y. Cong, B. Ding, J. Sun, W. Tan, *Nat. Biomed. Eng.* **2019**, *3*, 183; f) H. Im, H. Shao, Y. I. Park, V. M. Peterson, C. M. Castro, R. Weissleder, H. Lee, *Nat. Biotechnol.* **2014**, *32*, 490.

[5] S. Jeong, J. Park, D. Pathania, C. M. Castro, R. Weissleder, H. Lee, *ACS Nano* **2016**, *10*, 1802.

[6] H. Shao, J. Chung, L. Balaj, A. Charest, D. D. Bigner, B. S. Carter, F. H. Hochberg, X. O. Breakefield, R. Weissleder, H. Lee, *Nat. Med.* **2012**, *18*, 1835.

[7] a) J. M. Figueroa, J. Skog, J. Akers, H. Li, R. Komotar, R. Jensen, F. Ringel, I. Yang, S. Kalkanis, R. Thompson, L. LoGuidice, E. Berghoff, A. Parsa, L. Liau, W. Curry, D. Cahill, C. Bettegowda, F. F. Lang, E. A. Chiocca, J. Henson, R. Kim, X. Breakefield, C. Chen, K. Messer, F. Hochberg, B. S. Carter, *Neuro-Oncology* **2017**, *19*, 1494; b) E. Castellanos-Rizaldos, D. G. Grimm, V. Tadigotla, J. Hurley, J. Healy, P. L. Neal, M. Sher, R. Venkatesan, C. Karlovich, M. Raponi, A. Krug, M. Noerholm, J. Tannous, B. A. Tannous, L. E. Raez, J. K. Skog, *Clin. Cancer Res.* **2018**, *24*, 2944.

[8] R. E. Lane, D. Korbie, M. Trau, M. M. Hill, *Proteomics* **2019**, *19*, 1800156.

[9] A. N. Böing, E. van der Pol, A. E. Grootemaat, F. A. Coumans, A. Sturk, R. Nieuwland, *J. Extracell. Vesicles* **2014**, *3*, 23430.

[10] a) N. Karimi, A. Cvjetkovic, S. C. Jang, R. Crescitelli, M. A. Hosseinpour Feizi, R. Nieuwland, J. Lötvall, C. Lässer, *Cell. Mol. Life Sci.* **2018**, *75*, 2873; b) B. W. Sódar, Á. Kittel, K. Pálóczi, K. V. Vukman, X. Osteikoetxea, K. Szabó-Taylor, A. Németh, B. Sperlágh, T. Baranyai, Z. Giricz, Z. Wiener, L. Turiák, L. Drahos, É. Pállinger, K. Vékey, P. Ferdinandy, A. Falus, E. I. Buzás, *Sci. Rep.* **2016**, *6*, 24316; c) K. Takov, D. M. Yellon, S. M. Davidson, *J. Extracell. Vesicles* **2019**, *8*, 1560809.

[11] M. P. Caulfield, S. Li, G. Lee, P. J. Blanche, W. A. Salameh, W. H. Benner, R. E. Reitz, R. M. Krauss, *Clin. Chem.* **2008**, *54*, 1307.

[12] F. A. W. Coumans, A. R. Brisson, E. I. Buzas, F. Dignat-George, E. E. E. Drees, S. El-Andaloussi, C. Emanueli, A. Gasecka, A. Hendrix, A. F. Hill, R. Lacroix, Y. Lee, T. G. van Leeuwen, N. Mackman, I. Mäger, J. P. Nolan, E. van der Pol, D. M. Pegtel, S. Sahoo, P. R. M. Siljander, G. Sturk, O. de Wever, R. Nieuwland, *Circ. Res.* **2017**, *120*, 1632.

[13] Z. Brownlee, K. D. Lynn, P. E. Thorpe, A. J. Schroit, *J. Immunol. Methods* **2014**, *407*, 120.

[14] U. Olsson, G. Camejo, S. O. Olofsson, G. Bondjers, *Biochim. Biophys. Acta* **1991**, *1097*, 37.

[15] K. Lipponen, P. W. Stege, G. Cilpa, J. Samuelsson, T. Fornstedt, M. L. Riekkola, *Anal. Chem.* **2011**, *83*, 6040.

[16] S. Yokoyama, R. Hayashi, T. Kikkawa, N. Tani, S. Takada, K. Hatanaka, A. Yamamoto, *Arterioscler., Thromb., Vasc. Biol.* **1984**, *4*, 276.

[17] T. Liangsupree, E. Multia, J. Metso, M. Jauhiainen, P. Forssén, T. Fornstedt, K. Öörni, A. Podgornik, M. L. Riekkola, *Sci. Rep.* **2019**, *9*, 11235.

[18] L. Connell-Crowley, T. Nguyen, J. Bach, S. Chinniah, H. Bashiri, R. Gillespie, J. Moscariello, P. Hinckley, H. Dehghani, S. Vunnum, G. Vedantham, *Biotechnol. Bioeng.* **2012**, *109*, 157.

[19] J. Webber, A. Clayton, *J. Extracell. Vesicles* **2013**, *2*, 19861.

[20] a) K. Lee, K. Fraser, B. Ghaddar, K. Yang, E. Kim, L. Balaj, E. A. Chiocca, X. O. Breakefield, H. Lee, R. Weissleder, *ACS Nano* **2018**, *12*, 494; b) K. Fraser, A. Jo, J. Giedt, C. Vinegoni, K. S. Yang, P. Peruzzi, E. A. Chiocca, X. O. Breakefield, H. Lee, R. Weissleder, *Neuro-Oncology* **2019**, *21*, 606.

[21] J. Van Deun, P. Mestdagh, R. Sormunen, V. Cocquyt, K. Vermaelen, J. Vandesompele, M. Bracke, O. De Wever, A. Hendrix, *J. Extracell. Vesicles* **2014**, *3*, 24858.

[22] X. Osteikoetxea, B. Sódar, A. Németh, K. Szabó-Taylor, K. Pálóczi, K. V. Vukman, V. Tamási, A. Balogh, Á. Kittel, É. Pállinger, E. I. Buzás, *Org. Biomol. Chem.* **2015**, *13*, 9775.

[23] J. Van Deun, P. Mestdagh, P. Agostinis, Ö. Akay, S. Anand, J. Anckaert, Z. A. Martinez, T. Baetens, E. Beghein, L. Bertier, G. Berx, J. Boere, S. Boukouris, M. Bremer, D. Buschmann, J. B. Byrd, C. Casert, L. Cheng, A. Cmoch, D. Daveloose, E. D. Smedt, S. Demirsoy, V. Depoorter, B. Dhondt, T. A. P. Driedonks, A. Dudek, A. Elsharawy, I. Floris, A. D. Foers, K. Gärtner, et al., EV-TRACK Consortium, *Nat. Methods* **2017**, *14*, 228.

© 2020 WILEY-VCH Verlag GmbH & Co. KGaA, Weinheim

Check for updates

Automated molecular-image cytometry and analysis in modern oncology

Ralph Weissleder[1,2,3] ✉ *and Hakho Lee*[1,2]

Abstract | Diagnostic methods for initial diagnosis and patient stratification for treatment are key to modern oncology, but many challenges remain. In developed countries, advances in early diagnosis and therapeutics have led to challenges in the sampling of sub-centimetre lesions, with repeat biopsies straining accuracy and throughput of pathological assessment. Conversely, low-income and middle-income countries face extremely limited pathology and imaging resources, large caseloads, convoluted and inefficient workflows, and a lack of specialists. Advances in material sciences, chemistry, engineering and artificial intelligence have led to the introduction of a new class of affordable image cytometers that enable automated cell phenotyping, with ongoing clinical testing indicating that these systems can alleviate existing bottlenecks and improve diagnostic efficiency. Ultimately, these diagnostic methods are likely to surpass current pathology approaches on the basis of the richness of molecular measurements and the fact that they require only scant cellular material, rather than tissue sections. As these methods can be miniaturized and are low-power, they can also be used in point-of-care settings. In this Review, we focus on new devices and approaches for the integrated analysis of scant cancer samples, particularly those obtained by fine-needle aspiration.

Cell-based cancer diagnostics are essential for clinical decision-making, particularly for establishing the correct diagnosis, choosing the appropriate treatment, enrolling patients in clinical trials, assessing therapeutic efficacy and/or restaging disease[1]. In current clinical practice, cancer specimens are commonly obtained by image-guided biopsy, fine-needle aspiration (FNA), surgical-tissue harvesting, punch biopsies, brushings, swabs, biopsy touch preparations ('touch preps'), fluid aspiration or blood analyses. Some of these methods (for example, core biopsies and open surgical biopsies for histopathology) yield abundant tissue for sectioning and staining, whereas other approaches (for example, brushings and touch preps for cytopathology) yield scant amounts of cellular materials. FNA can often be obtained with minimal intervention using small-gauge needles (20–25G), have very low complication rates and are generally well tolerated[2].

Rapid on-site assessment of cellular specimens has become increasingly important to narrowing the time between intervention and initiation of therapy, assuring specimen quality for subsequent diagnoses and minimizing sample degradation and loss during transport. The current workflows are still labour-intensive and are often centralized, requiring extensive sample processing and expert cytopathology review. Digital cytopathology and whole-slide imaging[3] have been implemented, but they also require substantial time, labour and financial investment. Taken together, these factors limit the throughput, financial affordability and global reach of cell-based cancer diagnostics.

A particular challenge to the implementation of cell-based cancer diagnostics is the reliable analysis of scant cellular specimens, either through manual imaging (which requires a trained cytopathologist to review an entire slide) or automated analysis (which incorporates machine-learning routines for automated analysis). Driven by advances in materials science, chemistry, engineering and artificial intelligence (AI), a new class of cell-based cancer diagnostics is emerging to address this challenge. In this Review, we discuss this new generation of automated molecular-image cytometers that uses advanced materials, engineering and AI approaches for digital cell phenotyping. These new 'all-in-one' systems address a potentially large unmet clinical need by enabling advanced cellular diagnostics and are well suited to: meeting the demands of an underserved global healthcare market; repeat sampling at ultra-low invasiveness through the use of small-gauge needles (which can reduce morbidity and is important in clinical trials where frequent sampling is desirable); improving turnaround times through point-of-care analysis and by avoiding biopsy core processing; improving and automating quality control; and reducing both time-to-diagnosis

[1]*Center for Systems Biology, Massachusetts General Hospital, Boston, MA, USA.*

[2]*Department of Radiology, Massachusetts General Hospital, Boston, MA, USA.*

[3]*Department of Systems Biology, Harvard Medical School, Boston, MA, USA.*

✉*e-mail: ralph_weissleder@hms.harvard.edu*

https://doi.org/10.1038/s41578-020-0180-6

and the variability of interpretation through automation. These emerging technologies complement others that are not covered in this Review, namely, low-cost flow cytometers[4,5], liquid biopsies focusing on cell-free DNA (cfDNA)[6], exosomes[7] and circulating tumour cells (CTCs)[8–10], and genomic screening tools (such as the FoundationOne companion diagnostic (F1CDx) and the next-generation-sequencing-based MSK-IMPACT diagnostic assay)[11–13]. Herein, we focus on the automated analysis of cellular specimens obtained by FNA (FIG. 1) and highlight the stains, affinity ligands and biomarkers required for molecular diagnosis, optical technologies used for image cytometry and machine-learning algorithms for automated image analyses, providing relevant examples of clinical applicability. Finally, we offer our perspectives on the current state of the field and on future developments.

Stains and biomarkers

Important considerations for the automated analysis of cellular specimens include chromogenic cellular stains, labelled antibodies for immunostaining and cycling technologies. Each of these staining approaches has to be optimized and the choice of biomarkers validated.

Generic cellular stains. Conventional cytopathology largely relies on chromogenic stains such as haematoxylin and eosin (H&E), Papanicolaou (Pap) and Giemsa. Stained specimens are reviewed by cytopathologists, who evaluate cells for a number of parameters, such as the nuclear:cytoplasmic ratio, nuclear features, mitoses, cell clusters, cell uniformity and cell cohesiveness[14–16]. Such analyses can be automated but are inherently limited by the lack of molecular information, resulting in variable diagnostic accuracies[17]. Most commercial cell analysers (TABLE 1) use this chromogenic staining approach for the automated analysis of white blood cells, whose morphometric features are much more homogenous than those of highly variable cancer cells[18,19].

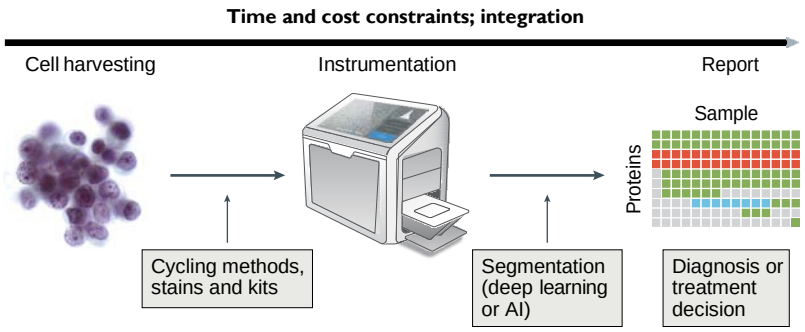

Fig. 1 | **Overview of automated molecular-image cytometry.** Small numbers of cancer cells obtained by fine-needle aspiration, brush biopsies (brushings), biopsy touch preparations (touch preps) or sampling of blood and/or bodily fluids can be subsequently analysed using automated molecular-image cytometry. Cycling methods, instrumentation and computational approaches are essential to the integrated and automated processing of such cells. Indeed, the analysis relies heavily on deep-learning and artificial intelligence (AI) approaches to extract information from dozens of channels and convert them into information that can inform patient management, including diagnosis and treatment decisions. For point-of-care settings, all of the above must occur within reasonable time frames and at a low cost.

Alternative dyes for the investigation of nuclear morphological features (such as aneuploidy and segmentation) include 4′,6-diamidino-2-phenylindole (DAPI), acridine orange, ethidium iodide, propidium iodide or flavins[20]. However, given the limitations of generic chromogenic staining, immunostaining for cancer-associated and host-cell markers has emerged as an alternative and is widely used for CTC analysis.

Immunostaining. Antibodies are increasingly being used in cytopathology, with the standard method being to perform one stain at a time, primarily using immunocytology (which involves absorption measurements of chemical reactions catalysed by antibody-conjugated enzymes) rather than immunofluorescence (which involves emission measurements of fluorescently labelled antibodies). This approach is a practical choice for the detection of key molecular cancer biomarkers while also enabling morphological assessment of cancer cells; for example, human epidermal growth factor receptor 2 (HER2) immunostaining in H&E slides enables simultaneous molecular and morphological assessment.

Multichannel fluorescence imaging allows the interrogation of molecular markers in cells via fluorescently labelled antibodies, typically in 4–8 channels. To further increase the number of biomarkers that can be analysed per cell (>20 channels), cycling technologies have been developed. These methods allow repeatedly staining, destaining (quenching) and restaining of cancer tissues. This, in turn, improves the depth of cell-by-cell profiling, pathway analysis and immunoprofiling in scant FNA samples. To compare different cycling methods[21–24], it is useful to consider how much of the sample is destroyed and/or lost during repeated washing and often harsh quenching conditions, how fast the quenching step is (which often ranges from tens of minutes to hours) and how fast each staining step is. Most cycling methods were originally developed for paraffin-embedded tissue sections that can withstand harsh destaining conditions. Unfortunately, however, these harsh conditions, which require the use of oxidants for bleaching, are often incompatible with FNA samples because the already scant cells are destroyed or lost during washes. Furthermore, it was not uncommon for early cycling technologies to require days to process samples.

Several cell-compatible cycling technologies have been developed over the past 5 years (FIG. 2; TABLE 2). We initially devised and validated multiple DNA-barcoded antibody technologies, including antibody barcoding with photocleavable DNA (ABCD)[25,26] and single-cell analysis for tumour phenotyping (SCANT)[24], while other groups have experimented with amplification strategies[27]. Although the SCANT method was shown to be robust and useful for pathway analysis in a clinical setting[24], one of the obstacles with this method was its comparatively modest signal-to-noise ratio and the long destaining times (0.5–1 h). The fast analytical screening technique (FAST), the latest method, bypasses these shortcomings and enables extremely fast cycling (>95% quenching in <10 s) (FIG. 2).

Table 1 | **Overview of experimental and commercial cell analysers**

Name	Imaging modality	Multiplex[a]	Cost[b]	Application	Ref. or company
Experimental prototypes					
D3	Holography	1	$	FNA samples	45
CEM	Holography	<3	$	Cancer FNA samples	32
AIDA	Holography	<3	$	Cancer FNA samples	31
CytoPAN	Fluorescence	4–6 (up to 20–40 with cycling)	$$	Cancer FNA samples	Under development
FPM	RGB	<3	$$	Tissue section	59
Commercial systems					
ThinPrep	RGB	<3	$$$$	Cervical (Pap) smear	Hologic
FocalPoint GS	RGB	<3	$$$$	Cervical (Pap) smear	Becton Dickinson
BestCyte	RGB	<3	$$$$	Cervical (Pap) smear	CellSolutions
CellaVision	RGB	<3	$$$$	WBC analysis	CellaVision
miLab	RGB, fluorescence	<3	$$$	WBC analysis	Noul
Iris	RGB	<3	$$$$	Urine analysis	Beckman Coulter

FNA, fine-needle aspiration; Pap, Papanicolaou; RGB, red, green and blue light; WBC, white blood cell. [a]Refers to the number of stains and not extractable image features. [b]Estimated cost of an instrument: $, <US$1,000; $$, US$1,000–US$4,999; $$$, US$5,000–US$9,999; $$$$≥US$10,000.

Choice of biomarkers. Selecting appropriate molecular markers is essential for identifying cancer cells, differentiating them from non-transformed host cells and profiling a growing number of treatment-relevant immune cells. Although host-cell markers have been thoroughly characterized by extensive flow-cytometry studies, epithelial cancer markers are more diverse and, therefore, require more immunostains for reliable detection. Furthermore, cancer markers are typically only expressed in a fraction of cells and patients. Although much more work needs to be done in this field to refine the choice of biomarker, a number of marker combinations have had some success in identifying cancer cells and differentiating them from host cells. Prominent examples include: epithelial cell adhesion molecule (EpCAM), cytokeratins, CD45 and CD16 for the identification of CTCs[28]; four-marker combination (the 'quad' marker set) comprising epidermal growth factor receptor (EGFR)+ EpCAM + mucin 1 (MUC1)+ WNT2 or EGFR, EpCAM, HER2 and MUC1[29,30]; HER2, oestrogen receptor (ER)/progesterone receptor (PR) for breast cancer[31]; CD19, CD20, immunoglobulin-κ and immunoglobulin-λ light chains and the proliferation marker Ki67 for lymphoma[32]; EGFR, thyroid transcription factor 1 (TTF1; also known as NKX2-1), chromogranin and synaptophysin for lung cancer[33]; EpCAM, calretinin, CD45 and vimentin (the 'ATCdx' marker set) for ovarian cancer[34]; and markers for mutated proteins, such as KRAS-G12D, EGFRv3, IDH1-R132G and BRAF-V600E, among others. This list is clearly not exhaustive but rather represents what has, to date, been used in automated cell analysers. We expect that the number of specific biomarker combinations and better immunostains (antibodies) and will grow in the future.

Optimizing materials for cellular analysis. Freshly obtained clinical samples need to be fixed, stained and captured on glass before they can be analysed. All of these steps require careful optimization and, often, modified materials. Fixation can usually be done in paraformaldehyde, methanol, propanol or other commercially available mixes, such as CytoRich Red (CRR). We have found empirically that some FNA samples of solid neoplasm are preserved better in 50%-diluted CRR, whereas fixation duration (ideally 15–30 min) is less critical.

Immunostaining is best performed in small plastic vials by adding antibody reagents to cells in a staining buffer. Antibody–fluorochrome stability, quality-control issues and limited access to basic tools (for example, centrifuge filters) are notable hurdles when using immunostains in remote areas and in point-of-care devices. The use of lyophilized antibodies and 'cocktails' that contain all of the necessary reagents can reduce variability[35].

An alternative immunostaining approach is to stain cells directly on glass slides after capture. Capturing cells on a glass slide is also critical to ensure that cells can be brought to the focal plane. Capture can be done using biological 'glues' (such as dopamine, biotin and neutravidin or polylysines) as slide coatings or, alternatively, glass slides can be coated with capture antibodies. Irrespective of the method used, careful validation is required for different applications. Non-specific antibody binding can often be reduced by coating slides with blocking materials such as bovine serum albumin (BSA) or polyethylene glycol (PEG) polymers.

To simplify sample handling and processing, commercial systems will likely adapt cartridges to perform all of the above steps in a single platform. One such example is in the miLab system (Noul), which incorporates cellular processing and staining in a single cartridge.

Image-cytometry systems

To inspect heterogeneous cell populations with statistical confidence, image cytometers must visualize large numbers of individual cells. Conventional geometric optics, however, are inherently constrained by the so-called space–bandwidth product (SBP)[36] and, therefore,

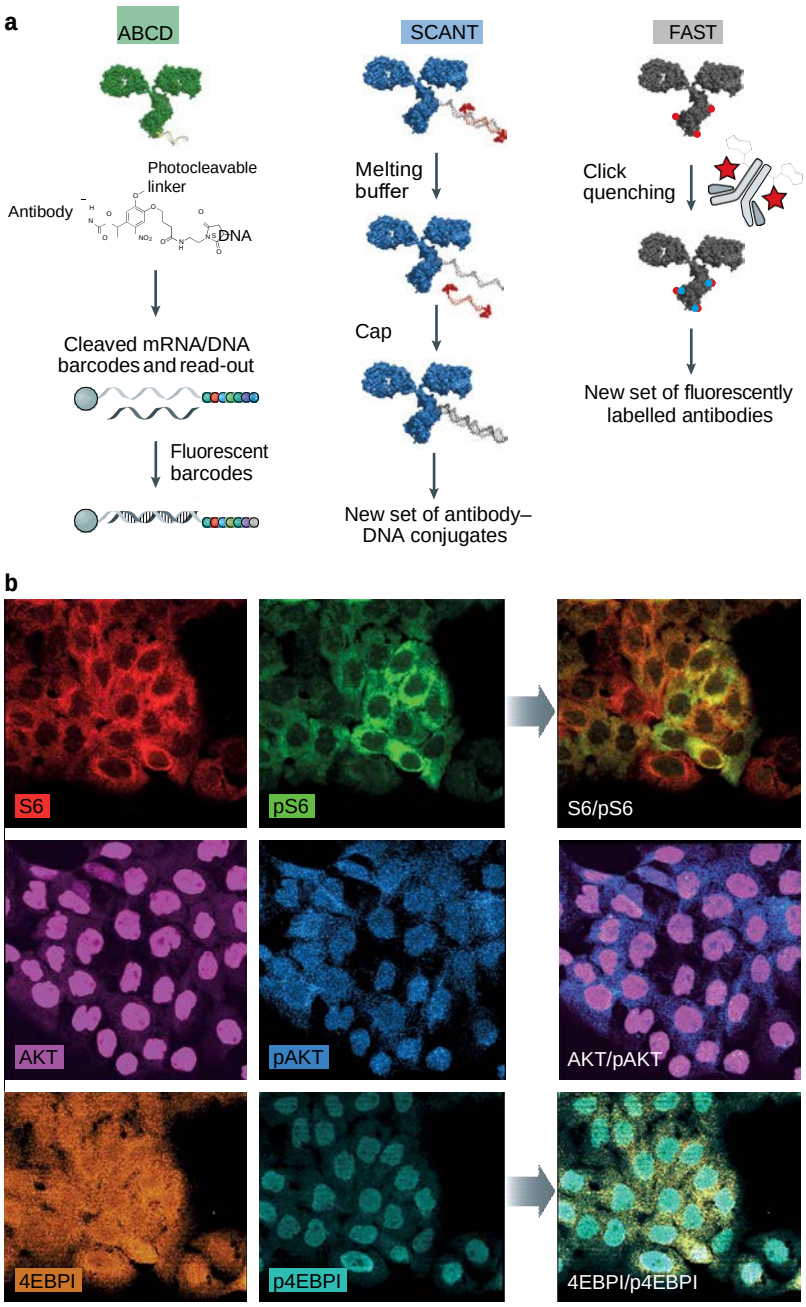

Fig. 2 | **Cyclic labelling technologies for multiplexed cancer-marker and host-cell-marker assessment. a** | An overview of the different cycling techniques, including antibody barcoding with photocleavable DNA (ABCD), single-cell analysis for tumour phenotyping (SCANT)[24] and fast analytical screening technique (FAST), is shown. In ABCD, DNA-barcoded antibodies bound to tissue of interest are photocleaved and then digitally detected by fluorescent barcodes or sequencing[25]. In SCANT, the primary barcoding stand on an antibody of interest contains a complementary imaging strand consisting of 13 bp and two fluorochromes. After imaging, the fluorescent strands are simply washed off with melting buffer and the primary strands are capped to reduce additional cycle-to-cycle background. Both ABCD and SCANT require several hours for processing. In FAST, fluorescently labelled antibodies are quenched with custom-designed clickable quenchers (<10 s), allowing multichannel imaging of 20–30 markers within an hour. **b** | Example of multiplexed single-cell profiling using the SCANT technique. Here, SCANT was applied to profile phosphoproteins in human A431 epidermoid carcinoma cells. Representative examples of phosphoprotein ratio imaging for ribosomal protein S6 (S6)/pS6RP, RACα serine/threonine-protein kinase (AKT)/pAKT and eukaryotic translation initiation factor 4E-binding protein 1 (4EBP1)/p4EBP1 are shown. Panel **b** is adapted from REF.[24], CC-BY-4.0 (https://creativecommons.org/licenses/by/4.0/).

produce megapixel information. This translates to a familiar experience — common microscopes have either a wide field of view (FOV) at low resolution or a small FOV at high spatial resolution, but not both at the same time.

Most laboratory imaging systems overcome this limit by combining high-magnification optics with mechanical stages to automatically scan slides and then transmit the information. Whole-slide imaging and digital-cytopathology technologies have progressed over the years[37] but challenges remain. Two key issues in digital cytopathology are focusing and the need for expert review. The focusing issue has largely been solved via either autofocusing algorithms or 3D imaging of thick *z*-stacks. Autofocusing software often uses either a least-squared or a mean-value method to locate the ideal focus plane[3], whereas 3D imaging, such as microscopy with optical sectioning, requires confocal laser scanning microscopy (CLSM), two-photon microscopy, structured illumination microscopy (SIM), light-sheet fluorescence microscopy (LSFM) or inverted selective plane illumination microscopy (iSPIM)[38]. All of these methods require expensive instrumentation and expert users, and often generate very large data sets[3,38,39]. As such, this particular approach limits deployment in resource-constrained remote locations.

New technological advances are increasingly enabling automated molecular-image cytometry, which is particularly helpful for point-of-care use. Computational optics, wherein optically encoded images are digitally interpreted, can expand the SBP beyond the physical limit of the optics. Advances in optoelectronics and micro-optics further enable the construction of compact, easy-to-control, high-performance systems. Using these approaches can also decrease the overall system cost, as optoelectronic parts and computation have become inexpensive. Three emerging modalities embody these new concepts — digital-holography cytometry, Fourier- ptychography cytometry and miniaturized-fluorescence cytometry.

Digital-holographic cytometry. Holographic imaging is coherent bright-field imaging that records an interference pattern or a hologram between a reference beam and an object. Digital holography acquires such holograms in a digital format and computationally converts them into object images. This approach can greatly simplify optics, as a light source, usually a light-emitting diode (LED), imaging objects and a digital imager can be aligned along the same optical axis[31,32,40–45] (FIG. 3a). This configuration, called lens-free digital in-line holography (LDIH), renders the system compact and cost-effective, requiring no intermediate optical components such as lenses and filter sets. By placing the samples directly on top of an imager, LDIH achieves a large FOV, equivalent to the entire sensing area of the imager (FIG. 3b). High spatial resolution is obtained through numerical image reconstruction (FIG. 3c), particularly using iterative phase-retrieval processes[32]. Reconstructed holograms, therefore, contain a greater amount of information (~10^8 pixels) than a conventional microscope of similar spatial resolution (~10^6 pixels). Furthermore, as LDIH

Table 2 | **Comparison of cellular cycling techniques**

Technique[a]	Targets	Channels	Cycles	Time	Cost[b]	Refs
ABCD; bead-based, fluorescent barcodes	<100	NA	NA	>1 day	$$$	25,26
SCANT; DNA–fluorochrome hybridization	~20–30	4–6	4–5	1 day	$$	24
FAST; site-specific, instant quenching	~20–40	4–6	6–8	<1 hour (for 20 markers)	$	NA

ABCD, antibody barcoding with photocleavable DNA; FAST, fast analytical screening technique; NA, not applicable; SCANT, single-cell analysis for tumour phenotyping. [a]Collectively, these cycling technologies enable the imaging of 20–40 targets in individual cells and can be used for cellular mapping, cellular pathway analysis or heterogeneity studies. [b]Estimated reagent cost for a single sample imaged at 20–100 channels: $, <US$50; $$, US$50–US$499; $$$, <US$500–US$4,999.

is a quantitative phase-imaging technique[46], phase information can be used to infer cell morphology and intracellular content related to the refractive index[47].

Various LDIH systems have been developed. Highly portable systems were initially designed based on smartphones[45], using phone-embedded cameras as detectors. Stand-alone devices were subsequently developed for global health applications, incorporating additional user-friendly features (including touchscreens and sample cartridges) that are difficult to integrate into smartphones[32] (FIG. 3d). Initial LDIH applications typically identified biological targets (such as blood cells, bacteria and *Caenorhabditis elegans*) on the basis of their unique morphology[40,48–50]. Over the past 5 years, new labelling strategies have been explored to impart molecular specificity, thereby improving diagnostic accuracy. In one example involving the labelling of cells with molecularly specific microbeads to alter holographic patterns (FIG. 3c), counting the number of cell-bound beads enabled quantitative molecular profiling of cancer cells[45]. Immunocolour staining is another approach to molecular profiling (FIG. 3e), as hologram intensities (light absorbance) can vary according to staining levels. This approach has been exploited for breast-cancer phenotyping in point-of-care settings[31]. Measurements of molecular biomarker expression using these methods are generally concordant with flow-cytometry-based measurements (FIG. 3f).

However, despite its promise, technical challenges remain for on-site LDIH applications. Hologram reconstruction is a computationally intensive process that requires a powerful computer, preferably one equipped with graphical processing units (GPUs), or cloud computing with a reliable network connection. Deep-learning-based machine vision might mitigate some of these requirements[32,51,52] (FIG. 3g), but its robust performance across a broad range of samples has yet to be demonstrated. Furthermore, spatially connected or dense biological objects can be difficult to image using LDIH, as the numerical phase retrieval becomes unstable. In such samples, multiple measurements with different physical parameters — such as sample-to-sensor distances[53], illumination angles[54] and wavelengths[31,55] — are necessary. LDIH also has limited multiplexing capacity; immunobead labelling is best suited to single-marker or dual-marker detection per sample and colour staining for ≤3 markers in the same sample. Thus, diagnostics based on cellular morphology and a few molecular markers would be a niche application for LDIH.

Fourier-ptychography cytometry. In Fourier ptychography, a set of overlapping, spatially shifted diffraction patterns are acquired and then numerically stitched (or 'folded', hence, the Greek prefix ptychí) to generate a larger diffraction pattern. The strategy effectively increases the numerical aperture (NA) of an optical system, improving spatial resolution without compromising the FOV[31,55]. Most Fourier ptychography microscopy (FPM) systems use programmable LED arrays as an illumination source, and data acquisition starts with taking a sequence of wide-FOV images at low magnification by changing the illumination pattern of the LED array (FIG. 4a). Individual images have low resolution and contain a spatially shifted spectrum of an imaged sample in the Fourier domain (FIG. 4b). Numerical post-processing coherently combines these intensity-only images in the Fourier space to recover high-frequency information. Through this process, the numerical aperture (NA_{FPM}) of the system becomes the sum of NA values of an objective lens (NA_{obj}) and an illumination source (NA_{light})[56]. Thus, for a given incident light (wavelength λ), FPM can achieve a higher resolving power ($\sim\lambda/(NA_{obj}+NA_{light})$) than a regular microscope ($\sim\lambda/NA_{obj}$). FPM yields gigapixel-level information, enabling high-resolution imaging of numerous cells, and can even reveal subcellular detail[57] (FIG. 4c). Furthermore, using low magnification objectives, FPM also supports a large focal depth, robust to variations in sample thickness.

Technical developments over the past 5 years have advanced FPM systems closer to point-of-care use. The original FPM method was time-consuming and resource-intensive, as large numbers (>200) of raw images were acquired by sequentially turning on a single LED. A new illumination scheme has increased the speed of this process through the use of a pseudorandom illumination pattern designed to minimize data redundancy in the Fourier space[57], acquiring fewer images (~40). Furthermore, a deep-learning approach to Fourier-spectrum recovery can ease the computational load of image processing[58]. Fundamental drawbacks, however, remain. For example, the aforementioned multiplexing challenges that limit LDIH still apply because FPM is a form of coherent-light microscopy. FPM also requires thin samples with a smoothly varying phase; this is necessary to map the low-resolution images, obtained at different incident angles, to different passbands of the Fourier spectrum and to, thereby, recover a high-resolution sample image[59–61].

Miniaturized-fluorescence cytometry. As the list of known cancer biomarkers grows, the need for multiplexed cellular profiling also increases, largely driven by interest in improving diagnostic accuracy and facilitating molecularly based treatment decisions. Conventional immunocytology, which is based on chromogenic staining and bright-field microscopy, typically probes only for a few biomarkers simultaneously. Fluorescent imaging, particularly in combination

with cycling technologies, is a potent approach for in-depth multiplexing; a major technical challenge is to transform bulky, expensive microscopes into compact, affordable equivalents for point-of-care use. Fortunately, advances in optoelectronics have made high-quality miniaturized optical parts available, prompting new systems engineering. For example, small LEDs can deliver sufficient power to replace conventional lamps or lasers as an excitation light source, and the photosensitivity of semiconductor imagers has improved substantially for reliable low-light detection[62]. Another opportunity is to augment manual image curation with automated analyses using machine-learning approaches.

Thumb-sized fluorescent microscopes (miniscopes) integrate optical components into a single device[62] (FIG. 5a). Using a gradient-refractive-index objective lens enables shortening of the optical path and can drastically

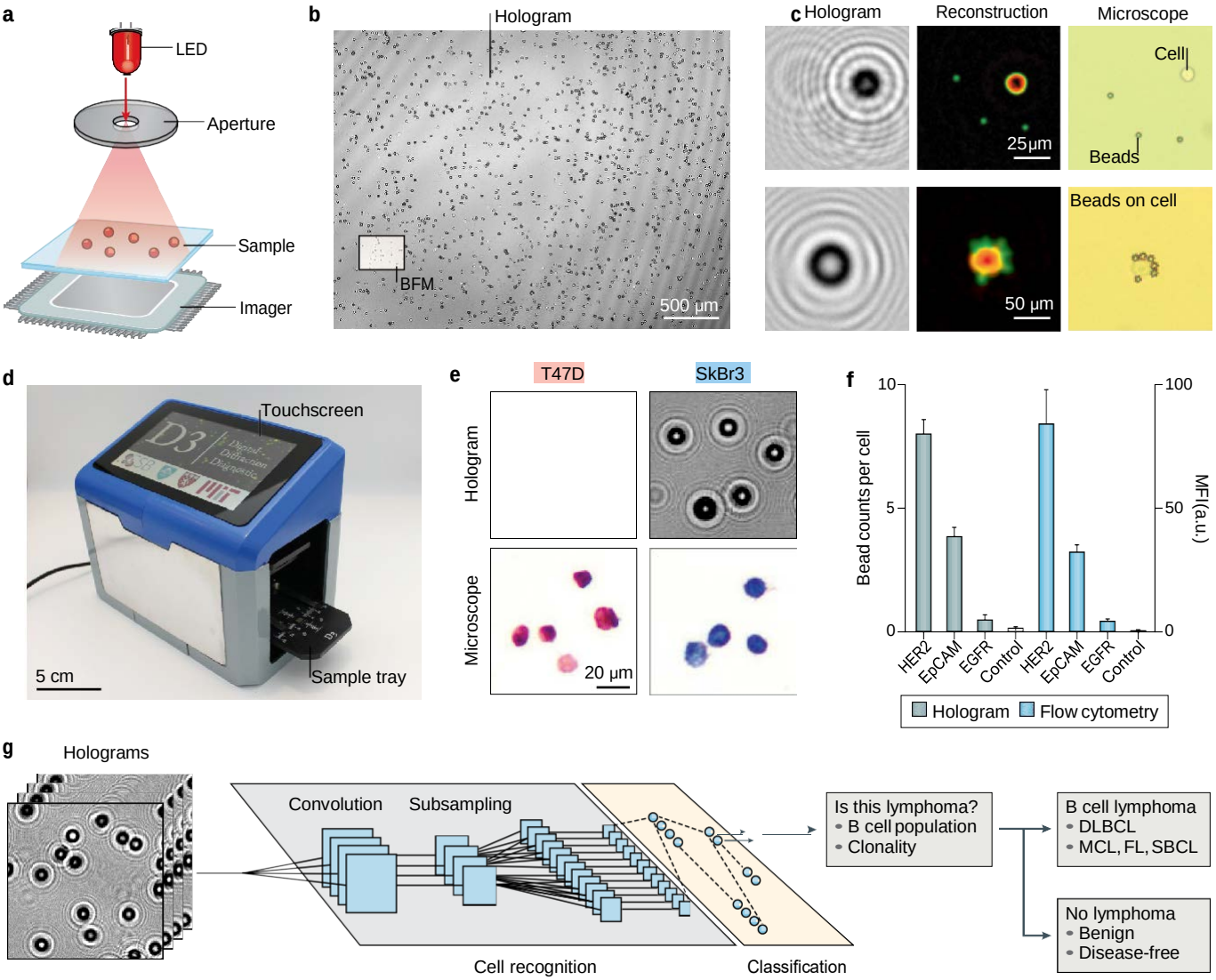

Fig. 3 | **LDIH. a** | Imaging configuration in lens-free digital in-line holography (LDIH). The system consists of a light-emitting diode (LED), an aperture and an imager, with a sample placed directly above the imager. **b** | Wide-field-of-view hologram captured by the LDIH imaging system. The individual block dots are cells, and the black box indicates the field of view of a ×20 bright-field microscope (BFM). **c** | Raw holograms show undecipherable patterns but the numerical image reconstruction recovers object images. The reference BFM images were taken at ×20 magnification. **d** | A portable, stand-alone LDIH device built and used for point-of-care cancer diagnostics. Recorded holograms are transferred to a remote server for image reconstruction. **e** | Human T47D and SkBr3 breast cancer cells were stained for the oestrogen receptor/progesterone receptor (red) and human epidermal growth factor receptor 2 (HER2; blue) and imaged via LDIH and BFM. Note that the hologram contrast changed according to the staining level. **f** | Cells were labelled for different biomarkers and analysed by LDIH and flow cytometry. Note that hologram-based and flow-cytometry-based analysis of biomarker expression is generally concordant. **g** | Deep-learning algorithms for hologram analyses. A convolutional neural network identifies labelled cells directly from holograms. Images classified as cells enter the next module for colour classification. The final information is used for lymphoma diagnostics. DLBCL, diffuse large B cell lymphoma; EGFR, epidermal growth factor receptor; EpCAM, epithelial cell adhesion molecule; FL, follicular lymphoma; MCL, mantle-cell lymphoma; MFI, mean fluorescence intensity; SBCL, spindle B cell lymphoma. Panels **a** and **b** are adapted with permission from REF.[31], American Chemical Society. Panel **c** is adapted with permission from REF.[45], Proceedings of the National Academy of Sciences. Panel **d** is adapted from REF.[32], Springer Nature Limited. Panel **e** is adapted with permission from REF.[31], American Chemical Society. Panel **f** is adapted with permission from REF.[45], Proceedings of the National Academy of Sciences.

reduce system size (2.4 cm^3, 1.9 g)[62]. Such a small form factor allows the scope to be mounted on an animal's head with minimal interruption to its natural behaviour[63,64] for imaging of live fluorescently tagged cells. As potential point-of-care applications, miniscopes have been used for cell profiling and bacterial detection[62] (FIG. 5b). In addition, a miniscope array can perform large-area imaging without scanning, taking advantage of the scope's small lateral size (~5 mm). The miniscope design is now in the public domain as an open-source microscope[65], promoting new ideas and functional extension. System modification and computational processing have enabled two-photon excitation[66], volumetric rendering[67] and lensless imaging[68].

For simultaneous multicolour (≥4) cellular analyses, we recently developed the Cytometry Portable Analyser (CytoPAN) system, which was originally built for operation in remote locations (FIG. 5c) but has since been applied in point-of-care settings (for example, in the operating room, interventional suites and doctors' offices). In this system, the excitation light sources are positioned for side illumination through a glass slide, and a single emission filter with four passbands is used; no dichroic mirrors or mechanical filter changes are necessary. Furthermore, intelligent software can be used to streamline the entire assay, including light-source calibration, sample-slide detection, data acquisition and cellular analyses. CytoPAN has four different fluorescent channels (FIG. 5d) and a bright-field imaging capacity. As proof-of-concept of its utility, automated CytoPAN software algorithms were shown to be capable of analysing individual cells and producing summary reports to inform cancer diagnosis (FIG. 5e). This affordable system (<$3,500), which is operable by non-skilled workers, is currently undergoing field testing in low-income and middle-income countries.

As these fluorescent systems are still bound by the physical SBP limit, a trade-off between FOV and spatial resolution remains. Computational methods used in coherent imaging cannot be applied because fluorescent emission does not carry phase information. New approaches for wide-FOV fluorescent imaging still need further improvement in image quality[68,69]. For now, a straightforward workaround is to combine sample scanning with miniaturized optics; a key technical requirement is to automate such operations, including stage movement and imaging stitching. Equally important is the development of tools for reliable sample preparation, for example, by connecting fluidic cartridges with cost-effective pumping systems[70]. This approach would

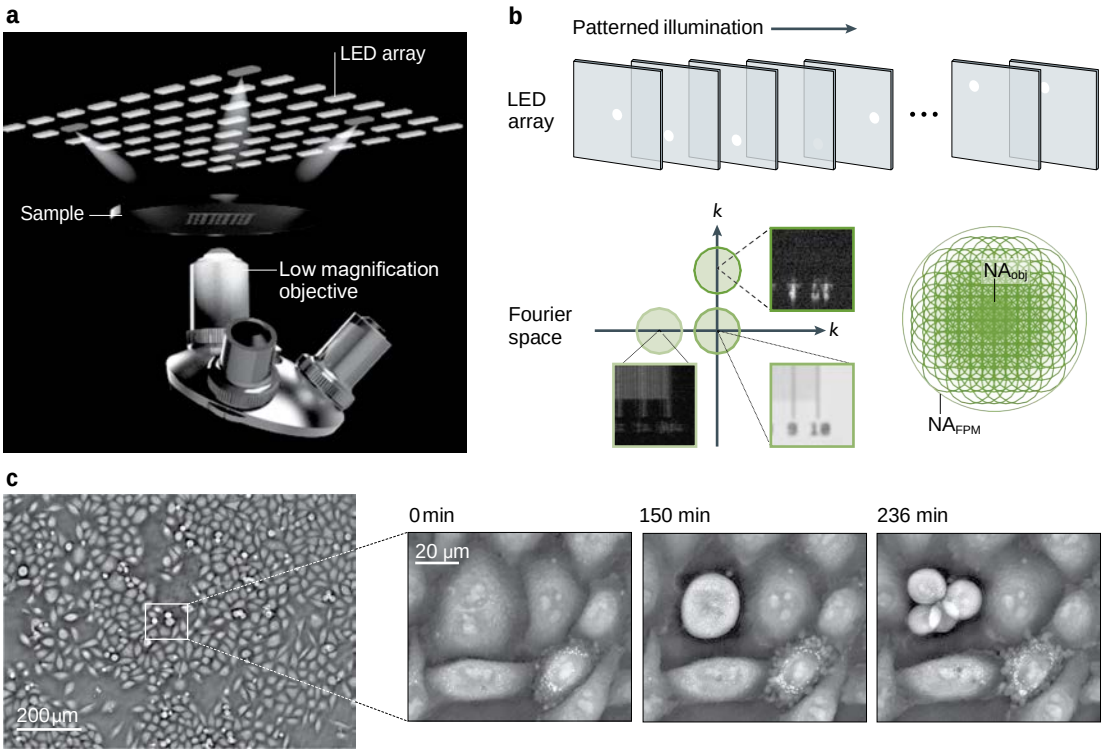

Fig. 4 | **FPM. a** | In a Fourier ptychography microscopy (FPM) system, an array of light-emitting diodes (LEDs) is used for angled illumination and low-magnification-objective lenses capture large-field-of-view (FOV) images. **b** | Sequential images at different illumination patterns are acquired. Each image, bounded by the numerical aperture (NA) of an objective lens (NA_{obj}), contains a patch of frequency information from different regions of the sample's Fourier space. Numerical reconstruction stitches these patches together to cover a larger frequency domain. The effective numerical aperture of the system (NA_{FPM}) is $NA_{obj} + NA_{light}$, where NA_{light} is the numerical aperture of the illumination source. **c** | A full-FOV FPM image reconstruction of human HeLa cells. The image, taken with a ×4 objective lens, achieved a ×0.8 NA resolution and has a FOV of 2.1 × 1.8 mm^2. The time-lapse images (reconstructed from a zoom-in of the original image; white box) reveal a cell undergoing mitosis (that is, dividing into multiple daughter cells), highlighting the ability of FPM to show subcellular detail. Indeed, globular daughter cells, which would have been blurred in conventional high-magnification microscopy, remain in focus with FPM. Panel **c** is adapted with permission from REF.[57], The Optical Society.

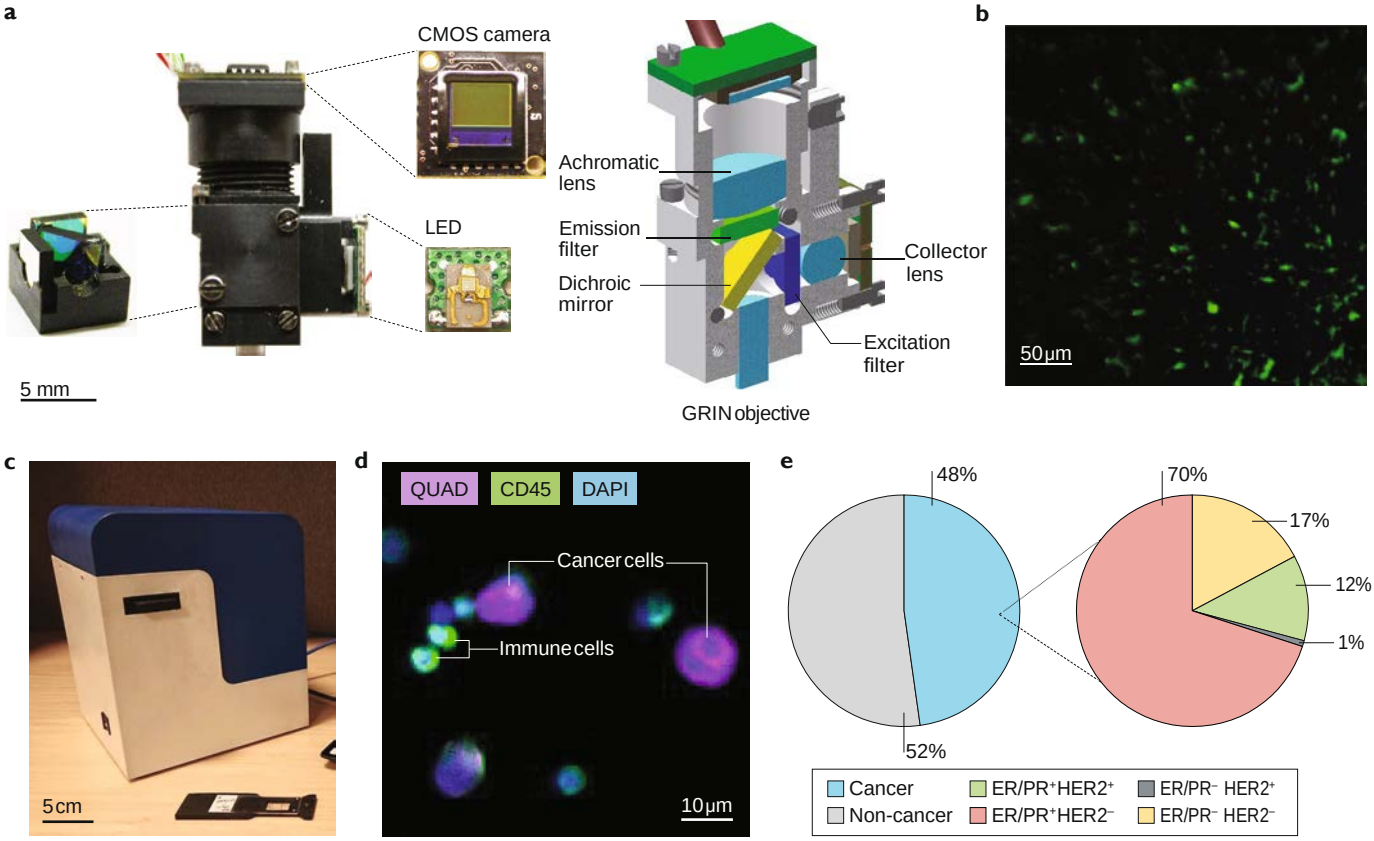

Fig. 5 | **Miniaturized fluorescent cytometers. a** | In thumb-sized fluorescent microscopes ('miniscopes'), a finger-sized, single-channel fluorescent microscope is structured like a conventional fluorescent microscope but uses a light-emitting diode (LED) as an excitation source and a gradient refractive index (GRIN) lens as an objective lens. **b** | The miniscope was used to image *Mycobacterium tuberculosis* stained with the fluorescent dye auramine O. The image shows a 300 × 300-pixel region of the complementary metal–oxide–semiconductor (CMOS) camera. **c** | The Cytometry Portable Analyser (CytoPAN) system is currently under development and integrates five light sources and a quad-band filter. No mechanical parts are necessary for multiple-channel imaging. **d** | Upon CytoPAN-based analysis of a fine-needle aspiration specimen from a patient with breast cancer, cancer cells are identified through the staining of 'quad markers' (QUAD) — epidermal growth factor receptor, epithelial cell adhesion molecule, human epidermal growth factor receptor 2 (HER2) and mucin 1, or epidermal growth factor receptor, epithelial cell adhesion molecule, cytokeratins and mucin 1 — and immune cells are identified through CD45 staining. Images are taken at ×5 magnification. **e** | CytoPAN software automatically profiles individual cells in multicolour channels and generates a summary report to guide cancer diagnosis. From the total cell counts, the proportion of cancer cells (QUAD positive) is obtained (left) and further stratified according to the expression levels of oestrogen receptor (ER)/progesterone receptor (PR) and HER2. Panels **a** and **b** are adapted from REF.[62], Springer Nature Limited. Panels **c**, **d** and **e** courtesy of J. Min and L. K. Chin.

increase the speed of assays and minimize procedural errors, particularly in cyclic imaging, which requires repeated fluidic handling (quenching, washing and labelling).

Machine learning for imaging analyses

Manually inspecting and analysing images produced by the aforementioned systems is time-consuming, impractical, subject to the bias of the operators and requires trained specialists who are often scarce in low-income and middle-income countries. Machine learning has emerged as an indispensable tool to effectively address these challenges. Classic machine-learning tools, such as logistic regression, learn to make inferred decisions based on an input of preselected data features[71]. Such features are typically manually selected and serve to condense complex information (for example, a whole-cell image) into a smaller set of numeric variables (such as size and shape). By contrast, deep-learning tools simultaneously learn to extract relevant features from complex input data and to manipulate those features to perform specified tasks[71]. With exposure to training examples, deep-learning algorithms incrementally update data-transformation parameters to improve task performance. Once fully trained, models can be further improved through continuous exposure to new data sets.

Computational platforms for machine learning and dedicated imaging software. In deep learning, convolutional neural networks (CNNs) are the most widely used architectures for cellular-imaging analyses, due to their strong performance in the analysis of spatial information[72,73] (BOX 1; FIG. 6a). CNNs are designed to process data with array-like structures, such as images, which are 2D arrays of pixels. Machine-learning models can be built with most existing programming languages

Box 1 | **Key concepts in CNNs**

In deep learning, convolutional neural networks (CNNs) are the most widely used architectures for cellular-imaging analyses. The principal concepts employed in CNN development are outlined here.

Convolution

This operation takes an input, multiplies it with a weight matrix (also termed a kernel or filter) and produces summed output layers[121]. The weight matrix is much smaller than the input, and the output layer, or feature map, displays an input's response to a particular filter. Each element of the feature map is based on a small number of neighbouring input elements (sparse interactions), and different regions of the feature map are produced by the same filter parameters (parameter sharing). These two properties dramatically minimize the number of parameters when evaluating the whole input. Convolution effectively finds localized but generalizable structures. Global interaction is still preserved through successive convolution operations; output elements in a deeper convolution layer are indirectly connected to larger numbers of input elements.

Activation functions

In CNNs, information flows unidirectionally through network layers. Activation functions bridge two adjacent networks, transforming the output of a preceding network and feeding it to the following one. Activations are necessary to make the entire network non-linear and to, therefore, increase its capacity for problem-solving. The most common function is a rectified linear unit (ReLU)[122,123] with the form $a(x) = \max(0, x)$. Another popular function is softmax, which takes number outputs from a convolution layer and converts them into the probability distributions for potential outcomes[124].

Pooling

The output from an activation function can go through a pooling operation, which replaces each output element with a summary statistic of its neighbourhood. CNNs often use the max pooling, which reports the maximum value within a rectangular neighbourhood[125]. Pooling downsamples the output by the neighbourhood size, and also makes the network invariant to minute changes in inputs. For example, the pooled output can be the same even if certain features are translated by a few pixels in images.

Training and testing

Building a CNN for a given task usually involves two steps — a new model learns to optimize its parameters using a training data set and the trained model is applied to previously unseen inputs (a test data set) to assess generalization. Underfitting occurs when the training error is above a preset threshold. Overfitting occurs when the training error is much less than the generalization error.

Regularization

Underfitting can be resolved by expanding the model's learning capacity, typically by increasing the number of network parameters. Reducing overfitting, however, requires more systematic strategies that are collectively called regularization. One such technique, dropout, stands out as computationally efficient and broadly applicable[126]. At a predefined probability (dropout rate), dropout intentionally removes the output elements from intermediate networks. This stochastically mimics evaluating an ensemble of models with different subnetwork structures. The final model can, therefore, be more generalizable to a given task.

Data augmentation

The accuracy of a neural network improves as more data are used for training. Data augmentation expands training data sets by creating artificial data[77]. The method has been particularly effective for image-classification problems. Cell images, for example, can be pixel-shifted, rotated or mirrored without losing a real-world context.

Hyperparameters

As settings that define a model architecture and control learning processes, hyperparameters exist outside of the model's domain and must be set externally. Search algorithms such as grid search and Bayesian optimization can be used to automate hyperparameter optimization by forming a wrapper around a learning model. This approach, however, is computationally expensive. In most cases, tuning hyperparameters is a heuristic process, largely relying on programmers' experience.

Transfer learning

A model trained for one task can be reused to solve a second related task if the tasks share common features[127]. For example, a CNN optimized for cancer-cell detection can be retrained to identify other cell types. In this case, the transferred network serves as an initial instance to be fine-tuned for a new task. In another form, an unaltered, pretrained network is concatenated with additional networks, wherein the pretrained network is used to capture general features. Transfer learning can narrow the scope of possible models to be searched[51].

(C, C++, Java, MATLAB, Python or R), and new languages, such as Julia, have been developed for faster computation. The de facto language for machine learning, however, is Python, the popularity of which has been boosted among data scientists by the release of TensorFlow, a computational framework for machine learning, in the Python application programming interface[74]. Various machine-learning frameworks are also available (for examples, see Supplementary Table 1), providing convenient building blocks as well as GPU-compatible libraries for accelerated computation.

The organization of computational layers, referred to as the model architecture, depends on the analysis task. Although frameworks exist for designing novel architectures, researchers might opt for predefined models with established success. For image-to-image transformations, such as single-cell segmentation, the U-Net[75] and DeepLab[76] architectures are two popular choices. These models encode images into information-rich features by convolution and then deconvolve them to produce segmentation images at input resolution. By contrast, classification tasks use feature encodings to produce a probability distribution among classes. These CNN architectures typically differ in the building blocks that make up the encoding process. Popular architectures include AlexNet[77], ResNet[78], VGG[79] and Inception[80].

Stand-alone imaging software now tends to integrate learning capacities in its design[81–86] (Supplementary Table 2). These tools make it possible to build machine-learning models in a coding-free, user-friendly environment, but analysis might be limited to predefined tasks. Some software expands its flexibility by incorporating support for script interpretation or communication with external programs.

Machine learning in conventional cytopathology. Conventional cytopathology incorporates computational approaches in the form of automated slide analysis and whole-slide imaging. These approaches still rely on expert and optimized slide preparation, state-of-the art microscopes and slide scanners (which often cost more than $100,000) and specialists to analyse flagged abnormalities. Nevertheless, these approaches and their clinical use provide important lessons from which the

next generation of automated image-cytometry systems can benefit[14].

There are currently three commercial systems that use proprietary algorithms to analyse Pap-stained cervical-cytology slides — the ThinPrep Imaging System (Hologic, Marlborough, MA), the FocalPoint GS Imaging System (Becton Dickinson, Franklin Lakes, NJ) and BestCyte (CellSolutions, Greensboro, NC)[17,87]. Beyond these systems, experimental studies have used machine learning to automate nuclear morphometry for the analysis of breast-cancer[15,16,88,89] cells and other malignancies[17].

Cellular analyses based on machine learning. In addition to facilitating conventional tasks in image analyses[75,90–95], the power of machine learning to discover and generalize hidden patterns could advance new paradigms in cytometry.

For example, in the case of in silico labelling, a deep neural network learned to predict fluorescent labels from unstained bright-field micrographs[96] (FIG. 6b). The network was trained on paired images of unlabelled and fluorescently labelled cells. The use of *z*-stacks of bright-field images improved prediction accuracy,

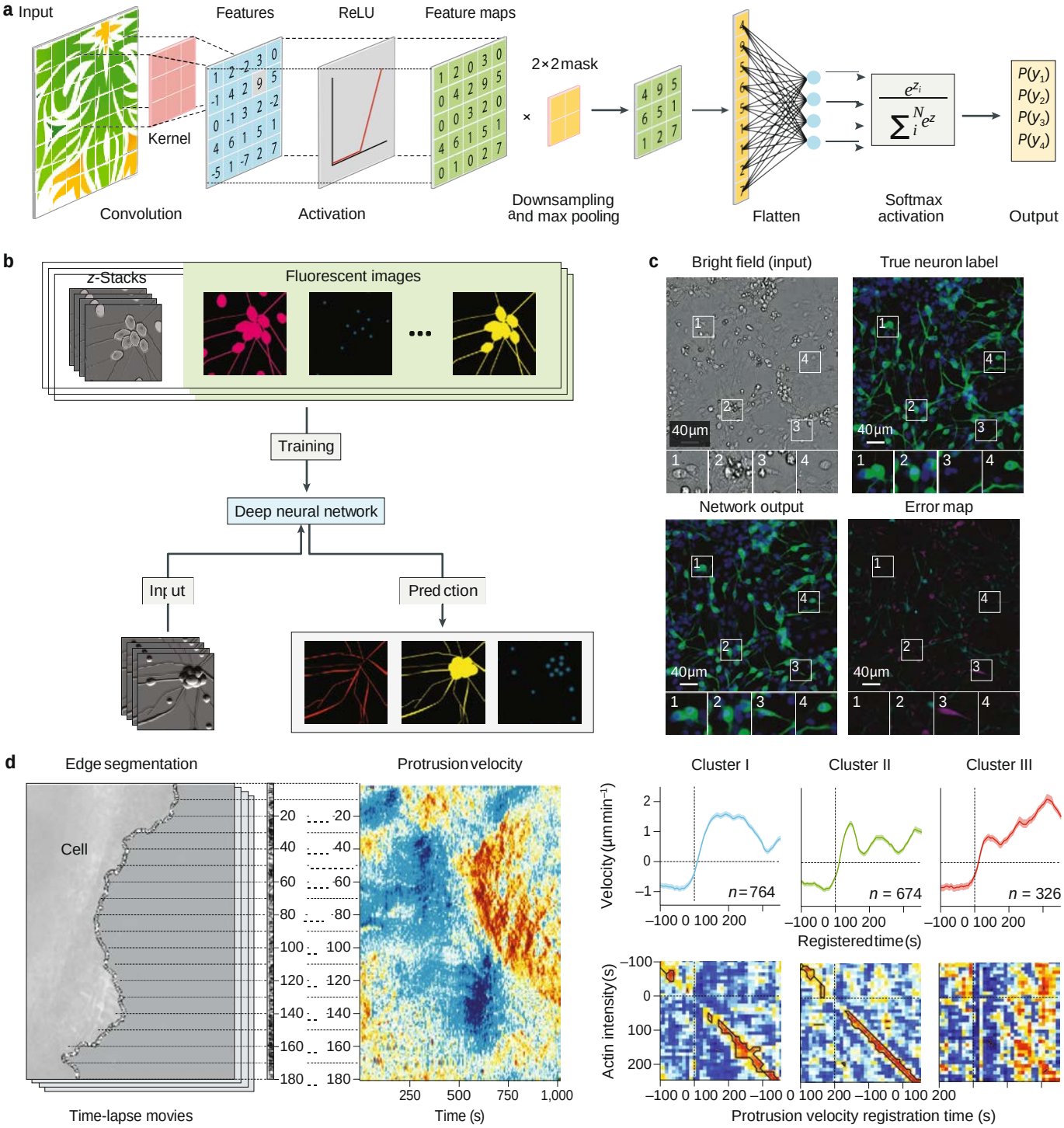

presumably by increasing the morphological information available for feature extraction. Indeed, the network reported smaller errors as more distinct *z*-stack images were used. By predicting cellular labelling, the trained model could identify cell types and cell state (FIG. 6c). Furthermore, the knowledge was transferrable; once trained to predict a set of labels, the network could learn new labels from a small number of additional data sets, effectively demonstrating transfer learning (BOX 1).

Machine learning has also effectively determined heterogeneous cellular phenotypes that otherwise would be obscured in complexity. For example, a computational approach was developed to analyse subcellular protrusion activities in time-lapse micrographs[97] (FIG. 6d). Without supervision, the framework resolved different protrusion velocities and mapped them into three distinct clusters, revealing a previously unknown 'accelerating protrusion'. Interestingly, the protrusion phenotypes could be associated with actin regulator dynamics, highlighting how machine learning might help to discover unknown molecular mechanisms.

Clinical cytometry applications

The technical requirements for diagnosis vary among different cancer types. Below are some practical examples highlighting the use of new cytometry methods.

Lymphoma. One of the major health challenges in sub-Saharan Africa is the high prevalence of AIDS-related cancers (sometimes termed the 'second wave of AIDS')[98–100]. Some such cancers, for example, diffuse large B cell lymphoma (DLBCL) and Burkitt lymphoma, are very aggressive. However, owing to limited resources, many patients with these malignancies evade comprehensive evaluation or are not appropriately classified. Diagnosis and care are often hampered by an inability to acquire proper tissue specimen, lack of diagnostic reagents, limited availability of specialists and low access to care in rural settings. Although a major portion of these cases are curable (even in low-income and middle-income countries), therapeutic opportunities are often missed[101,102].

In 2018, a prospective clinical trial used the contrast-enhanced LDIH system and the aforementioned deep-learning algorithm on percutaneously obtained FNA samples from 40 patients who were clinically referred for aspiration and biopsy of enlarged lymph nodes (lymphadenopathy) detected by whole-body imaging that were suspicious of lymphoma[32]. Freshly harvested FNA samples were captured on glass slides via CD19/CD20 antibodies and incubated with antibody-coated beads (targeting immunoglobulin κ or λ light chains or Ki67) of unique sizes, absorbancies and holographic signatures. Bead binding to cells was holographically measured and the end result was a quantitative read-out of malignant cell numbers and differentiation between high-grade and low-grade lymphoma subtypes. The automated method was surprisingly accurate and fast, with 91% sensitivity, 100% specificity and 95% accuracy for diagnosing lymphoma and 86% accuracy in triaging lymphomas into aggressive and indolent types. No false positives were found for benign or disease-free samples, and only one sample was non-diagnostic due to low B cell counts. By comparison, clinical flow cytometry showed 10 non-diagnostic cases with 87% accuracy for diagnosing lymphoma. More importantly, flow cytometry either could not or failed to distinguish aggressive from indolent types. Larger-scale trials are currently underway in HIV-endemic regions of Africa.

Breast cancer. Breast-cancer diagnosis and the differentiation between palpable mass lesions and benign lesions is another considerable problem in low-income and middle-income countries with severe diagnostic bottlenecks. Artificial Intelligence Diffraction Analysis (AIDA), a low-cost digital system based on computational optics and deep learning, was designed to diagnose breast cancer from FNA samples[31]. Unlike the bead-based microholography in lymphoma[32], AIDA uses chromogenic stains with enzyme-mediated amplification to resolve receptor status in harvested cells. A promising early study showed high accuracy (>90%) in recognizing cells directly from diffraction patterns and in classifying breast-cancer types using deep-learning-based analysis of sample aspirates. The image algorithm was fast, enabling cellular analyses at high throughput (~3 s per 1,000 cells), and the automated workflow enables use by less skilled healthcare workers. For global healthcare applications, the system is currently being adapted for even simpler operation[31]. Additionally, large-scale trials of the fluorescence multiplexing technology (CytoPAN) are underway.

Oral cancer. Over 90% of oral cancers are squamous-cell carcinomas. These head and neck squamous-cell carcinomas are the sixth leading cancer by incidence worldwide, with more than 550,000 cases and ~300,000 deaths per year, and are very common in parts of the world that

Fig. 6 | **Machine learning in imaging analyses. a** | Key concepts in convolutional neural networks are shown. Convolution followed by activation extracts features, and the pooling operation downsamples intermediate layers while keeping salient features. 2D feature maps are then reshaped into a vector (flattening) and, following traditional neural network layers, a softmax activation produces a final probability distribution for classification. **b** | In the case of in silico labelling, machine learning has been used to predict fluorescent labelling from unlabelled images and to infer cell type. By using *z*-stacks of transmitted and fluorescent micrographs as training sets, a convolution neural network learned to predict fluorescent labelling from unlabelled images. **c** | The in silico labelling approach was applied to predict cell type. The input image (bright field) contains various cell types differentiated from pluripotent stem cells. In the ground-truth image, cells were stained for neuron-specific class III β-tubulin (TuJ1; green) and nucleus (Hoechst; blue). The network was trained to predict the intensity of these labels at each pixel. In the error map, predicted pixels that are too bright (false positives) are displayed in magenta and those that are too dim (false negatives) are displayed in teal. Outsets 1, 2 and 4 show correct predictions but note that outset 3 shows a false positive — a cell that has neuronal morphology but is not TuJ1 positive. **d** | Machine learning has also shown promise for subcellular-feature analysis. A leading edge of a migrating cell was imaged over time. The cell boundary was segmented into small probing windows and the protrusion velocity in each window was tracked. Unsupervised machine learning grouped protrusion activities into three clusters. Cluster III is a previously unknown phenotype, 'accelerating protrusion', whereas clusters I and II showed a high correlation between protrusion velocities and actin activities. The results imply that actin nucleation might mediate subcellular protrusion. Cluster III had no distinct pattern, suggesting different actin molecular dynamics. ReLU, rectified linear unit. Panels **b** and **c** are adapted with permission from REF.[96], Elsevier. Panel **d** is adapted from REF.[97], CC-BY-4.0 (https://creativecommons.org/licenses/by/4.0/).

have high rates of tobacco use, betel use and/or human papillomavirus infection[103,104]. As not all oral lesions are malignant, biopsy-based histopathological diagnosis is essential. In prior research, a fluorescently labelled poly(ADP-ribose) polymerase (PARP) inhibitor (PARPi-FL) was developed as an intravital fluorescent dye to be used in point-of-care settings[105–108]. Studies from the past 5 years have shown the feasibility of using PARPi-FL as a quantitative biomarker for oral cancer[106]. Preliminary results from a first-in-human trial (NCT03085147)[108] devised a PARPi-FL topical-staining protocol for human biospecimens. Using fresh oral-cancer tissues within 25 min of biopsy, the protocol correctly identified cancer and margin samples with >95% sensitivity and specificity. The study also showed that PARPi-FL imaging can be integrated into clinical workflows to instantaneously assess the presence or absence of microscopic disease at the surgical margin.

Diagnosing cancer in fluid samples. Numerous bodily fluids can be readily sampled with small needles and subsequently analysed for cancer cells. Such procedures include paracentesis, thoracentesis and cyst-fluid aspiration, all of which are often performed either therapeutically to relieve symptoms or for diagnosis. Conventionally processing such samples still requires labour-intensive concentration, embedding, staining and review. In 2013, a microfluidic-chip platform was developed to enrich cancer cells from highly heterogeneous peritoneal fluid and then perform molecular analyses. Using four of the most promising biomarkers (EpCAM, calretinin, CD45 and vimentin) and 47 patients, the results showed that the marker set can sensitively and specifically map cancer cell numbers and, through its reliable enrichment, facilitate additional treatment-response measurements related to proliferation, protein translation or pathway inhibition[34].

Future perspective

We have reviewed the technical features of new imaging cytometers and their potential for integrated analysis of scant cancer samples. Below, we discuss key milestones to advance the clinical translation and adoption of these new technologies.

Implementation and dissemination. In contemporary laboratory medicine, virtually all blood and urine tests have been automated to reduce cost, improve test quality and accommodate the increasing volume of clinical samples[18,19] (TABLE 1). We argue that this automation should also be possible for FNA-based analysis of cancer samples, particularly in resource-limited environments. Furthermore, an expected rise in minimally invasive procedures combined with a shortage of trained cytopathologists will likely exacerbate the need for automated hardware and software solutions in such settings. Moving forward, a key consideration is what will be required to make the development of new technology a clinical reality.

We are still in the research phase of developing and testing integrated solutions. Once accomplished, the merging of technologies and approaches will need to be rigorously tested in prospective clinical trials and different settings. Preferably, these efforts must continue at a large scale and in varied environments. The latter is particularly important, as AI approaches have been shown to be location dependent[109]. In the end, adopting any new technology will require concerted efforts and investment from all parties involved. We direct interested readers to other reviews that have extensively covered the road map towards the ultimate clinical translation of diagnostic platforms[110,111].

New materials and integrated optics. Paradigms in optical system design are changing — conventional discrete free-space optics, the mainstay since the invention of microscopes, is moving towards integrated precision optoelectronics. Novel material engineering and fabrication technologies drive such transitions. Planar optical waveguides[112], adaptive microlenses[113] and meta materials[114,115] have demonstrated potential for effective beam steering and shaping, and tiny semiconductor chips are readily available for light generation and detection. Multi-material manufacturing can assemble these parts into hybrid devices. For instance, optical components (lenses, filters and waveguides) can be defined in transparent polymer layers[116] and be coupled to semiconductor modules. Hybrid optical sensors are already in production for oximetry and heart-rate monitoring (MAX30102, Maxim). The next step is to expand into optical imaging to create on-chip microscopy technologies.

Future capabilities. One of the most exciting opportunities in this field is new technological capabilities that could be implemented for automated point-of-care cytometry, including the rigorous evaluation of cellular markers and staining techniques and kits. As optoelectronics become even more affordable and integrated, they might incorporate charge-coupled devices with larger FOVs and similar or smaller pixel sizes. Together with larger FOV lenses, this will improve the spatial resolution of images and, ultimately, enable subcellular-image analysis. Computational power and advanced machine-learning algorithms should accelerate reconstructions and improve automated analysis.

Automated, AI-based diagnostic DNA karyometry is another application of interest. A number of studies have tested this method[117–120], but mostly in flow cytometers or manually, rather than by automated image cytometry. An additional unexplored frontier is the molecular testing of cytology samples. Fluorescence in situ hybridization (FISH) using probes with specificity for mutations in the *EGFR*, *KRAS* and *BRAF* genes and other cytogenetic abnormalities should be feasible with appropriate amplification strategies[117]. Finally, the techniques for analysing FNA specimens for cancer diagnosis and monitoring will likely apply almost equally well to other specimen types and diagnostic applications. Inexpensive automated cellular analyses and molecular testing could be contemplated for organ FNA obtained from liver, kidney or blood and/or bone marrow.

Published online: 05 March 2020

1. Weissleder, R., Schwaiger, M. C., Gambhir, S. S. & Hricak, H. Imaging approaches to optimize molecular therapies. *Sci. Transl Med.* **8**, 355ps16 (2016).
2. Frenk, N. E. et al. High-content biopsies facilitate molecular analyses and do not increase complication rates in patients with advanced solid tumors. *JCO Precis. Oncol.* **1**, 1–9 (2017).
3. Capitanio, A., Dina, R. E. & Treanor, D. Digital cytology: A short review of technical and methodological approaches and applications. *Cytopathology* **29**, 317–325 (2018).
4. Asthana, V. et al. An inexpensive, customizable microscopy system for the automated quantification and characterization of multiple adherent cell types. *PeerJ* **6**, e4937 (2018).
5. Balsam, J., Bruck, H. A. & Rasooly, A. Mobile flow cytometer for mHealth. *Methods Mol. Biol.* **1256**, 139–153 (2015).
6. Molnár, B. et al. Circulating cell-free nucleic acids as biomarkers in colorectal cancer screening and diagnosis — an update. *Expert Rev. Mol. Diagn.* **19**, 477–498 (2019).
7. Shao, H. et al. New technologies for analysis of extracellular vesicles. *Chem. Rev.* **118**, 1917–1950 (2018).
8. Sandlin, R. D. et al. Ultra-fast vitrification of patient-derived circulating tumor cell lines. *PLOS ONE* **13**, e0192734 (2018).
9. Sarioglu, A. F. et al. A microfluidic device for label-free, physical capture of circulating tumor cell clusters. *Nat. Methods* **12**, 685–691 (2015).
10. Cristofanilli, M. et al. The clinical use of circulating tumor cells (CTCs) enumeration for staging of metastatic breast cancer (MBC): International expert consensus paper. *Crit. Rev. Oncol. Hematol.* **134**, 39–45 (2019).
11. No authors listed. First comprehensive companion diagnostic OK'd. *Cancer Discov.* **8**, OF4 (2018).
12. Van Hoeck, A., Tjoonk, N. H., van Boxtel, R. & Cuppen, E. Portrait of a cancer: mutational signature analyses for cancer diagnostics. *BMC Cancer* **19**, 457 (2019).
13. Hannouf, M. B. et al. Cost-effectiveness analysis of multigene expression profiling assays to guide adjuvant therapy decisions in women with invasive early-stage breast cancer. *Pharmacogenomics J.* **20**, 27–46 (2020).
14. Saha, M., Mukherjee, R. & Chakraborty, C. Computer-aided diagnosis of breast cancer using cytological images: a systematic review. *Tissue Cell* **48**, 461–474 (2016).
15. Filipczuk, P., Fevens, T., Krzyzak, A. & Monczak, R. Computer-aided breast cancer diagnosis based on the analysis of cytological images of fine needle biopsies. *IEEE Trans. Med. Imaging* **32**, 2169–2178 (2013).
16. Dey, P., Logasundaram, R. & Joshi, K. Artificial neural network in diagnosis of lobular carcinoma of breast in fine-needle aspiration cytology. *Diagn. Cytopathol.* **41**, 102–106 (2013).
17. Landau, M. A. & Pantanowitz, L. Artificial intelligence in cytopathology: a review of the literature and overview of commercial landscape. *J. Am. Soc. Cytopathol.* **8**, 230–241 (2019).
18. Stephens, L., Bevins, N. J., Bengtsson, H. I. & Broome, H. E. Comparison of different small clinical hematology laboratory configurations with focus on remote smear imaging. *Arch. Pathol. Lab. Med.* **143**, 1234–1245 (2019).
19. Andrade, A. R. et al. Recent computational methods for white blood cell nuclei segmentation: a comparative study. *Comput. Methods Prog. Biomed.* **173**, 1–14 (2019).
20. Prieto, S. P., Powless, A. J., Boice, J. W., Sharma, S. G. & Muldoon, T. J. Proflavine hemisulfate as a fluorescent contrast agent for point-of-care cytology. *PLOS ONE* **10**, e0125598 (2015).
21. Lin, J. R., Fallahi-Sichani, M. & Sorger, P. K. Highly multiplexed imaging of single cells using a high-throughput cyclic immunofluorescence method. *Nat. Commun.* **6**, 8390 (2015).
22. Gerdes, M. J. et al. Highly multiplexed single-cell analysis of formalin-fixed, paraffin-embedded cancer tissue. *Proc. Natl Acad. Sci. USA* **110**, 11982–11987 (2013).
23. Schubert, W. et al. Analyzing proteome topology and function by automated multidimensional fluorescence microscopy. *Nat. Biotechnol.* **24**, 1270–1278 (2006).
24. Giedt, R. J. et al. Single-cell barcode analysis provides a rapid readout of cellular signaling pathways in clinical specimens. *Nat. Commun.* **9**, 4550 (2018).
25. Ullal, A. V. et al. Cancer cell profiling by barcoding allows multiplexed protein analysis in fine-needle aspirates. *Sci. Transl Med.* **6**, 219ra9 (2014).
26. Agasti, S. S., Liong, M., Peterson, V. M., Lee, H. & Weissleder, R. Photocleavable DNA barcode–antibody conjugates allow sensitive and multiplexed protein analysis in single cells. *J. Am. Chem. Soc.* **134**, 18499–18502 (2012).
27. Kishi, J. Y. et al. SABER amplifies FISH: enhanced multiplexed imaging of RNA and DNA in cells and tissues. *Nat. Methods* **16**, 533–544 (2019).
28. De Wit, S. et al. Classification of cells in CTC-enriched samples by advanced image analysis. *Cancers* **10**, 377 (2018).
29. Haun, J. B. et al. Micro-NMR for rapid molecular analysis of human tumor samples. *Sci. Transl Med.* **3**, 71ra16 (2011).
30. Yang, K. S. et al. Multiparametric plasma EV profiling facilitates diagnosis of pancreatic malignancy. *Sci. Transl Med.* **9**, eaal3226 (2017).
31. Min, J. et al. Computational optics enables breast cancer profiling in point-of-care settings. *ACS Nano* **12**, 9081–9090 (2018).
32. Im, H. et al. Design and clinical validation of a point-of-care device for the diagnosis of lymphoma via contrast-enhanced microholography and machine learning. *Nat. Biomed. Eng.* **2**, 666–674 (2018).
33. Ghazani, A. A. et al. Molecular characterization of scant lung tumor cells using iron-oxide nanoparticles and micro-nuclear magnetic resonance. *Nanomedicine* **10**, 661–668 (2014).
34. Peterson, V. M. et al. Ascites analysis by a microfluidic chip allows tumor-cell profiling. *Proc. Natl Acad. Sci. USA* **110**, E4978–E4986 (2013).
35. Marquard, A. N., Carlson, J. C. T. & Weissleder, R. Glass chemistry to analyze human cells under adverse conditions. *ACS Omega* **4**, 11515–11521 (2019).
36. Lohmann, A. W., Dorsch, R. G., Mendlovic, D., Ferreira, C. & Zalevsky, Z. Space–bandwidth product of optical signals and systems. *J. Opt. Soc. Am. A* **13**, 470–473 (1996).
37. Van Es, S. L. et al. Constant quest for quality: digital cytopathology. *J. Pathol. Inform.* **9**, 13 (2018).
38. Hu, B., Bolus, D. & Brown, J. Q. Improved contrast in inverted selective plane illumination microscopy of thick tissues using confocal detection and structured illumination. *Biomed. Opt. Express* **8**, 5546–5559 (2017).
39. Wang, M. et al. Gigapixel surface imaging of radical prostatectomy specimens for comprehensive detection of cancer-positive surgical margins using structured illumination microscopy. *Sci. Rep.* **6**, 27419 (2016).
40. Garcia-Sucerquia, J. et al. Digital in-line holographic microscopy. *Appl. Opt.* **45**, 836–850 (2006).
41. Gurkan, U. A. et al. Miniaturized lensless imaging systems for cell and microorganism visualization in point-of-care testing. *Biotechnol. J.* **6**, 138–149 (2011).
42. Zheng, G., Lee, S. A., Antebi, Y., Elowitz, M. B. & Yang, C. The ePetri dish, an on-chip cell imaging platform based on subpixel perspective sweeping microscopy (SPSM). *Proc. Natl Acad. Sci. USA* **108**, 16889–16894 (2011).
43. Kim, S. B. et al. A cell-based biosensor for real-time detection of cardiotoxicity using lensfree imaging. *Lab. Chip* **11**, 1801–1807 (2011).
44. Greenbaum, A. et al. Imaging without lenses: achievements and remaining challenges of wide-field on-chip microscopy. *Nat. Methods* **9**, 889–895 (2012).
45. Im, H. et al. Digital diffraction analysis enables low-cost molecular diagnostics on a smartphone. *Proc. Natl Acad. Sci. USA* **112**, 5613–5618 (2015).
46. Rostykus, M., Soulez, F., Unser, M. & Moser, C. Compact in-line lensfree digital holographic microscope. *Methods* **136**, 17–23 (2018).
47. Rappaz, B. et al. Comparative study of human erythrocytes by digital holographic microscopy, confocal microscopy, and impedance volume analyzer. *Cytometry A* **73**, 895–903 (2008).
48. Seo, S. et al. High-throughput lens-free blood analysis on a chip. *Anal. Chem.* **82**, 4621–4627 (2010).
49. Mudanyali, O., Bishara, W. & Ozcan, A. Lensfree super-resolution holographic microscopy using wetting films on a chip. *Opt. Express* **19**, 17378–17389 (2011).
50. Lee, S. A. et al. Color capable sub-pixel resolving optofluidic microscope and its application to blood cell imaging for malaria diagnosis. *PLOS ONE* **6**, e26127 (2011).
51. Kim, S. J. et al. Deep transfer learning-based hologram classification for molecular diagnostics. *Sci. Rep.* **8**, 17003 (2018).
52. Rivenson, Y., Zhang, Y., Günaydın, H., Teng, D. & Ozcan, A. Phase recovery and holographic image reconstruction using deep learning in neural networks. *Light Sci. Appl.* **7**, 17141 (2018).
53. Greenbaum, A. & Ozcan, A. Maskless imaging of dense samples using pixel super-resolution based multi-height lensfree on-chip microscopy. *Opt. Express* **20**, 3129–3143 (2012).
54. Luo, W., Zhang, Y., Feizi, A., Göröcs, Z. & Ozcan, A. Pixel super-resolution using wavelength scanning. *Light Sci. Appl.* **5**, e16060 (2016).
55. Bao, P., Situ, G., Pedrini, G. & Osten, W. Lensless phase microscopy using phase retrieval with multiple illumination wavelengths. *Appl. Opt.* **51**, 5486–5494 (2012).
56. Ou, X., Horstmeyer, R., Zheng, G. & Yang, C. High numerical aperture Fourier ptychography: principle, implementation and characterization. *Opt. Express* **23**, 3472–3491 (2015).
57. Tian, L. et al. Computational illumination for high-speed in vitro Fourier ptychographic microscopy. *Optica* **2**, 904–911 (2015).
58. Nguyen, T., Xue, Y., Li, Y., Tian, L. & Nehmetallah, G. Deep learning approach for Fourier ptychography microscopy. *Opt. Express* **26**, 26470–26484 (2018).
59. Zheng, G., Horstmeyer, R. & Yang, C. Wide-field, high-resolution Fourier ptychographic microscopy. *Nat. Photonics* **7**, 739–745 (2013).
60. Horstmeyer, R., Chung, J., Ou, X., Zheng, G. & Yang, C. Diffraction tomography with Fourier ptychography. *Optica* **3**, 827–835 (2016).
61. Dong, S. et al. Aperture-scanning Fourier ptychography for 3D refocusing and super-resolution macroscopic imaging. *Opt. Express* **22**, 13586–13599 (2014).
62. Ghosh, K. K. et al. Miniaturized integration of a fluorescence microscope. *Nat. Methods* **8**, 871–878 (2011).
63. Liberti, W. A., Perkins, L. N., Leman, D. P. & Gardner, T. J. An open source, wireless capable miniature microscope system. *J. Neural Eng.* **14**, 045001 (2017).
64. Jacob, A. D. et al. A compact head-mounted endoscope for in vivo calcium imaging in freely behaving mice. *Curr. Protoc. Neurosci.* **84**, e51 (2018).
65. Aharoni, D. & Hoogland, T. M. Circuit investigations with open-source miniaturized microscopes: past, present and future. *Front. Cell. Neurosci.* **13**, 141 (2019).
66. Helmchen, F., Fee, M. S., Tank, D. W. & Denk, W. A miniature head-mounted two-photon microscope. High-resolution brain imaging in freely moving animals. *Neuron* **31**, 903–912 (2001).
67. Skocek, O. et al. High-speed volumetric imaging of neuronal activity in freely moving rodents. *Nat. Methods* **15**, 429–432 (2018).
68. Adams, J. K. et al. Single-frame 3D fluorescence microscopy with ultraminiature lensless FlatScope. *Sci. Adv.* **3**, e1701548 (2017).
69. Ah Lee, S., Ou, X., Lee, J. E. & Yang, C. Chip-scale fluorescence microscope based on a silo-filter complementary metal-oxide semiconductor image sensor. *Opt. Lett.* **38**, 1817–1819 (2013).
70. Almada, P. et al. Automating multimodal microscopy with NanoJ-Fluidics. *Nat. Commun.* **10**, 1223 (2019).
71. LeCun, Y., Bengio, Y. & Hinton, G. Deep learning. *Nature* **521**, 436–444 (2015).
72. LeCun, Y., Bottou, L., Bengio, Y. & Haffner, P. Gradient-based learning applied to document recognition. *Proc. IEEE* **86**, 2278–2324 (1998).
73. Cao, C. et al. Deep learning and its applications in biomedicine. *Genom. Proteom. Bioinform.* **16**, 17–32 (2018).
74. Abadi, M. et al. TensorFlow: a system for large-scale machine learning. Preprint at *arXiv* https://arxiv.org/abs/1605.08695 (2016).
75. Ronneberger, O., Fischer, P. & Brox, T. U-Net: convolutional networks for biomedical image segmentation. *Med. Image Comput. Comput. Assist. Interv.* **9351**, 234–241 (2015).
76. Chen, L.-C., Papandreou, G., Kokkinos, I., Murphy, K. & Yuille, A. L. DeepLab: semantic image segmentation with deep convolutional nets, atrous convolution, and fully connected CRFs. *IEEE Trans. Pattern Anal. Mach. Intell.* **40**, 834–848 (2018).
77. Krizhevsky, A., Sutskever, I. & Hinton, G. E. ImageNet classification with deep convolutional neural networks. *Adv. Neural Inf. Process. Syst.* **1**, 1097–1105 (2012).
78. He, K., Zhang, X., Ren, S. & Sun, J. in *Proc. IEEE Comput. Soc. Conf. Comput. Vis. Pattern Recognit.* 770–778 (IEEE, 2016).
79. Simonyan, K. & Zisserman, A. Very deep convolutional networks for large-scale image recognition. Preprint at *arXiv* https://arxiv.org/abs/1409.1556 (2014).

80. Szegedy, C. et al. in *Proc. IEEE Comput. Soc. Conf. Comput. Vis. Pattern Recognit.* 1–9 (IEEE, 2015).
81. Schindelin, J. et al. Fiji: an open-source platform for biological-image analysis. *Nat. Methods* **9**, 676–682 (2012).
82. Kamentsky, L. et al. Improved structure, function and compatibility for CellProfiler: modular high-throughput image analysis software. *Bioinformatics* **27**, 1179–1180 (2011).
83. Held, M. et al. CellCognition: time-resolved phenotype annotation in high-throughput live cell imaging. *Nat. Methods* **7**, 747–754 (2010).
84. Murphy, R. F. CellOrganizer: image-derived models of subcellular organization and protein distribution. *Methods Cell Biol.* **110**, 179–193 (2012).
85. Sommer, C., Straehle, C., Koethe, U. & Hamprecht, F. A. in *Proc. IEEE Int. Symp. Biomed. Imaging* 230–233 (IEEE, 2011).
86. Kvilekval, K., Fedorov, D., Obara, B., Singh, A. & Manjunath, B. S. Bisque: a platform for bioimage analysis and management. *Bioinformatics* **26**, 544–552 (2010).
87. Thrall, M. J. Automated screening of Papanicolaou tests: a review of the literature. *Diagn. Cytopathol.* **47**, 20–27 (2019).
88. Kashyap, A., Jain, M., Shukla, S. & Andley, M. Study of nuclear morphometry on cytology specimens of benign and malignant breast lesions: a study of 122 cases. *J. Cytol.* **34**, 10–15 (2017).
89. Subbaiah, R. M., Dey, P. & Nijhawan, R. Artificial neural network in breast lesions from fine-needle aspiration cytology smear. *Diagn. Cytopathol.* **42**, 218–224 (2014).
90. Ouyang, W., Aristov, A., Lelek, M., Hao, X. & Zimmer, C. Deep learning massively accelerates super-resolution localization microscopy. *Nat. Biotechnol.* **36**, 460–468 (2018).
91. Buggenthin, F. et al. Prospective identification of hematopoietic lineage choice by deep learning. *Nat. Methods* **14**, 403–406 (2017).
92. Esteva, A. et al. Dermatologist-level classification of skin cancer with deep neural networks. *Nature* **542**, 115–118 (2017).
93. Gulshan, V. et al. Development and validation of a deep learning algorithm for detection of diabetic retinopathy in retinal fundus photographs. *JAMA* **316**, 2402–2410 (2016).
94. Van Valen, D. A. et al. Deep learning automates the quantitative analysis of individual cells in live-cell imaging experiments. *PLOS Comput. Biol.* **12**, e1005177 (2016).
95. Heo, Y. J., Lee, D., Kang, J., Lee, K. & Chung, W. K. Real-time image processing for microscopy-based label-free imaging flow cytometry in a microfluidic chip. *Sci. Rep.* **7**, 11651 (2017).
96. Christiansen, E. M. et al. In silico labeling: predicting fluorescent labels in unlabeled images. *Cell* **173**, 792–803.e19 (2018).
97. Wang, C. et al. Deconvolution of subcellular protrusion heterogeneity and the underlying actin regulator dynamics from live cell imaging. *Nat. Commun.* **9**, 1688 (2018).
98. Varmus, H. & Kumar, H. S. Addressing the growing international challenge of cancer: a multinational perspective. *Sci. Transl Med.* **5**, 175cm2 (2013).
99. Livingston, J. Cancer in the shadow of the AIDS epidemic in southern Africa. *Oncologist* **18**, 783–786 (2013).
100. Chabner, B. A. et al. Cancer in Botswana: the second wave of AIDS in Sub-Saharan Africa. *Oncologist* **18**, 777–778 (2013).
101. Naresh, K. N. et al. Lymphomas in sub-Saharan Africa – what can we learn and how can we help in improving diagnosis, managing patients and fostering translational research. *Br. J. Haematol.* **154**, 696–703 (2011).
102. Mwamba, P. M. et al. AIDS-related non-Hodgkin's lymphoma in sub-Saharan Africa: current status and realities of therapeutic approach. *Lymphoma* https://doi.org/10.1155/2012/904367 (2012).
103. Pai, S. I. & Westra, W. H. Molecular pathology of head and neck cancer: implications for diagnosis, prognosis, and treatment. *Annu. Rev. Pathol.* **4**, 49–70 (2009).
104. Pai, S. I. et al. Comparative analysis of the phase III clinical trials of anti-PD1 monotherapy in head and neck squamous cell carcinoma patients (CheckMate 141 and KEYNOTE 040). *J. Immunother. Cancer* **7**, 96 (2019).
105. Carney, B. et al. Target engagement imaging of PARP inhibitors in small-cell lung cancer. *Nat. Commun.* **9**, 176 (2018).
106. Kossatz, S. et al. Detection and delineation of oral cancer with a PARP1 targeted optical imaging agent. *Sci. Rep.* **6**, 21371 (2016).
107. Kossatz, S., Weber, W. & Reiner, T. Detection and delineation of oral cancer with a PARP1-targeted optical imaging agent. *Mol. Imaging* **16**, 1536012117723786 (2017).
108. Kossatz, S. et al. PARP1 as a biomarker for early detection and intraoperative tumor delineation in epithelial cancers–first-in-human results. Preprint at *bioRxiv* https://doi.org/10.1101/663385 (2019).
109. Couzin-Frankel, J. Medicine contends with how to use artificial intelligence. *Science* **364**, 1119–1120 (2019).
110. Goodsaid, F. M. The labyrinth of product development and regulatory approvals in liquid biopsy diagnostics. *Clin. Transl. Sci.* **12**, 431–439 (2019).
111. Pantanowitz, L. et al. Twenty years of digital pathology: an overview of the road travelled, what is on the horizon, and the emergence of vendor-neutral archives. *J. Pathol. Inform.* **9**, 40 (2018).
112. Kozma, P., Kehl, F., Ehrentreich-Förster, E., Stamm, C. & Bier, F. F. Integrated planar optical waveguide interferometer biosensors: a comparative review. *Biosens. Bioelectron.* **58**, 287–307 (2014).
113. He, Z., Lee, Y. H., Chanda, D. & Wu, S. T. Adaptive liquid crystal microlens array enabled by two-photon polymerization. *Opt. Express* **26**, 21184–21193 (2018).
114. Kuznetsov, A. I. et al. Laser-induced transfer of metallic nanodroplets for plasmonics and metamaterial applications. *J. Opt. Soc. Am. B* **26**, B130–B138 (2009).
115. Lin, R. J. et al. Achromatic metalens array for full-colour light-field imaging. *Nat. Nanotechnol.* **14**, 227–231 (2019).
116. Wolfer, T., Bollgruen, P., Mager, D., Overmeyer, L. & Korvink, J. G. Printing and preparation of integrated optical waveguides for optronic sensor networks. *Mechatronics* **34**, 119–127 (2016).
117. Hui, H. Y. L. et al. "Immuno-flowFISH" for the assessment of cytogenetic abnormalities in chronic lymphocytic leukemia. *Cytometry A* **95**, 521–533 (2019).
118. Mazzini, G. & Danova, M. Fluorochromes for DNA staining and quantitation. *Methods Mol. Biol.* **1560**, 239–259 (2017).
119. Ng, B. L., Fu, B., Graham, J., Hall, C. & Thompson, S. Chromosome analysis using benchtop flow analysers and high speed cell sorters. *Cytometry A* **95**, 323–331 (2019).
120. Smith, P. J., Darzynkiewicz, Z. & Errington, R. J. Nuclear cytometry and chromatin organization. *Cytometry A* **93**, 771–784 (2018).
121. Gupta, A. et al. Deep learning in image cytometry: a review. *Cytometry A* **95**, 366–380 (2019).
122. Jarrett, K., Kavukcuoglu, K., Ranzato, M. A. & LeCun, Y. in *IEEE 12th Int. Conf. Comput. Vis.* 2146–2153 (IEEE, 2009).
123. Nair, V. & Hinton, G. E. in *Proc. 27th Int. Conf. Mach. Learn.* 807–814 (2010).
124. Bridle, J. S. Training stochastic model recognition algorithms as networks can lead to maximum mutual information estimation of parameters. *Adv. Neural Inf. Process. Syst.* **2**, 211–217 (1990).
125. Zhou, Y. T. & Chellappa, R. in *IEEE Int. Conf. Neural Netw.* 71–78 (IEEE, 1988).
126. Srivastava, N., Hinton, G., Krizhevsky, A., Sutskever, I. & Salakhutdinov, R. Dropout: a simple way to prevent neural networks from overfitting. *J. Mach. Learn. Res.* **15**, 1929–1958 (2014).
127. Yosinski, J., Clune, J., Bengio, Y. & Lipson, H. How transferable are features in deep neural networks? *Adv. Neural Inf. Process. Syst.* **27**, 3320–3328 (2014).

Acknowledgements

The authors acknowledge extensive discussions with L.K. Chin, J. Min, J. Oh, H. Im, T. Rainer and J. Carlson, and thank C. Landeros for discussions on machine learning and K. Joyes for editing the manuscript. The authors are indebted to J. Higgins and C. Vinegoni for the critical review of the manuscript. The authors are supported by the following grants: NIH- UH3 CA202637, NIH- U01CA206997, NIH- R01CA204019 and NIH- R01CA206890 (R.W.); NIH- R01CA229777, NIH- U01CA233360, DoD- W81XWH1910199, DoD- W81XWH1910194 and MGH Scholar Fund (H.L.).

Author contributions

Both authors contributed equally to the preparation of this review.

Competing interests

R.W. declares that he has received consultancy payments from Tarveda Pharmaceuticals, Mode RNA, Alivio Therapeutics and Accure Health, and that he is a shareholder of T2 Biosystems, Lumicell, Accure Health and Aikili Biosystems. H.L. declares that he has received consultancy payments from Exosome Diagnostics and Accure Health, and that he is a shareholder of Accure Health and Aikili Biosystems. Patents: all patents associated with R.W. and H.L. have been assigned to and handled by Massachusetts General Hospital.

Publisher's note

Springer Nature remains neutral with regard to jurisdictional claims in published maps and institutional affiliations.

Supplementary information

Supplementary information is available for this paper at https://doi.org/10.1038/s41578-020-0180-6.

© Springer Nature Limited 2020

ACS NANO
Cite This: ACS Nano 2019, 13, 11698−11706
www.acsnano.org

Article

Compact and Filter-Free Luminescence Biosensor for Mobile *in Vitro* Diagnoses

Chen-Han Huang,[†,‡] Yong Il Park,[†] Hsing-Ying Lin,[†] Divya Pathania,[†] Ki Soo Park,[†] Maria Avila-Wallace,[⊥] Cesar M. Castro,[†,#] Ralph Weissleder,[*,†,▽] and Hakho Lee[*,†]

[†]Center for Systems Biology, Massachusetts General Hospital, Harvard Medical School, Boston, Massachusetts 02114, United States
[‡]Department of Biomedical Sciences and Engineering, National Central University, No. 300, Zhongda Rd., Zhongli District, Taoyuan City 32001, Taiwan
[§]School of Chemical Engineering, Chonnam National University, 77 Yongbong-ro, Buk-gu, Gwangju 61186, Republic of Korea
[⊥]Department of Obstetrics and Gynecology, Massachusetts General Hospital, Boston, Massachusetts 02114, United States
[#]Department of Medicine, Massachusetts General Hospital, Harvard Medical School, Boston, Massachusetts 02114, United States
[▽]Department of Systems Biology, Harvard Medical School, 200 Longwood Ave., Boston, Massachusetts 02115, United States

Supporting Information

ABSTRACT: We report a sensitive and versatile biosensing approach, LUCID (luminescence compact *in vitro* diagnostics), for quantitative molecular and cellular analyses. LUCID uses upconversion nanoparticles (UCNPs) as luminescent reporters in mutually exclusive photoexcitation and read-out sequences implemented on a smartphone. The strategy improves imaging signal-to-noise ratios, eliminating interference from excitation sources and minimizing autofluorescence, and thus enables filterless imaging. Here we developed a miniaturized detection system and optimized UCNPs for the system and biological applications. Nanoparticle luminescence lifetime was extended by controlling particle structure and composition. When tested with a range of biological targets, LUCID achieved high detection sensitivity (0.5 pM for protein and 0.1 pM for nucleic acids), differentiated bacterial samples, and allowed profiling of cells. In proof-of-concept clinical use, LUCID demonstrated effective screening of cancer cells in cervical brushing specimens, identifying patients at high risk for malignancy. These results suggest that LUCID could serve as a broadly applicable and inexpensive diagnostic platform.

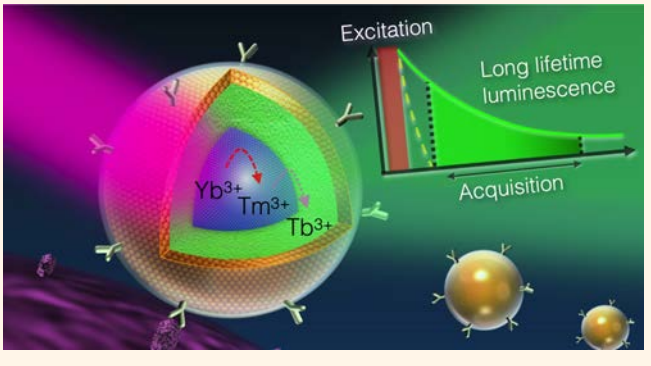

KEYWORDS: *diagnostic, point-of-care, nanoparticles, luminescence, global health*

Downloaded via HARVARD UNIV on November 27, 2019 at 14:36:35 (UTC).
See https://pubs.acs.org/sharingguidelines for options on how to legitimately share published articles.

Infections and cancer are leading causes of death in low and middle income countries (LMICs), with annual death tolls reaching over 7 million (infection, 4.7 million; cancer, 2.4 million).[1] Access to treatment of preventable and curable diseases has significantly improved in many LMIC settings, spurred by continuing global initiatives.[2,3] Reaping the full benefit of these advances mandates access to affordable diagnostic tests to enable prompt initiation of treatment or expedited patient triaging. Limited infrastructure and geographical barriers, however, demand stringent performance metrics on LMIC diagnostics.[4,5] Assays should yield actionable results preferably at the point-of-care (POC). Moreover, sensing systems should be easy to operate and maintain and also be compact for use in mobile clinics. We further reason that ideal POC sensors should be platform technologies equipped to deal with diverse targets in the field settings. Different sensor types have been advanced for POC operations, yet typically limited to specific analytic targets. For example, low-cost membrane-based sensors allow for low-resolution, qualitative measurement of soluble molecules (e.g., serum proteins, nucleic acids).[6−8] For cellular detection, miniaturized imaging devices have been developed,[9−12] although their operation often relies on intensive computation,[13] complex optics (e.g., fluorescence, illumination control),[11,14] or external servers.[15]

We set out to devise an end-user-friendly, generalizable strategy for quantitative molecular tests. We specifically explored upconversion nanoparticles (UCNPs) in an imaging-based assay, both for soluble targets, bacterial and cellular detection. UCNPs have a distinct optical feature—they emit

Received: July 18, 2019
Accepted: August 28, 2019
Published: August 28, 2019

© 2019 American Chemical Society

DOI: 10.1021/acsnano.9b05634
ACS Nano 2019, 13, 11698−11706

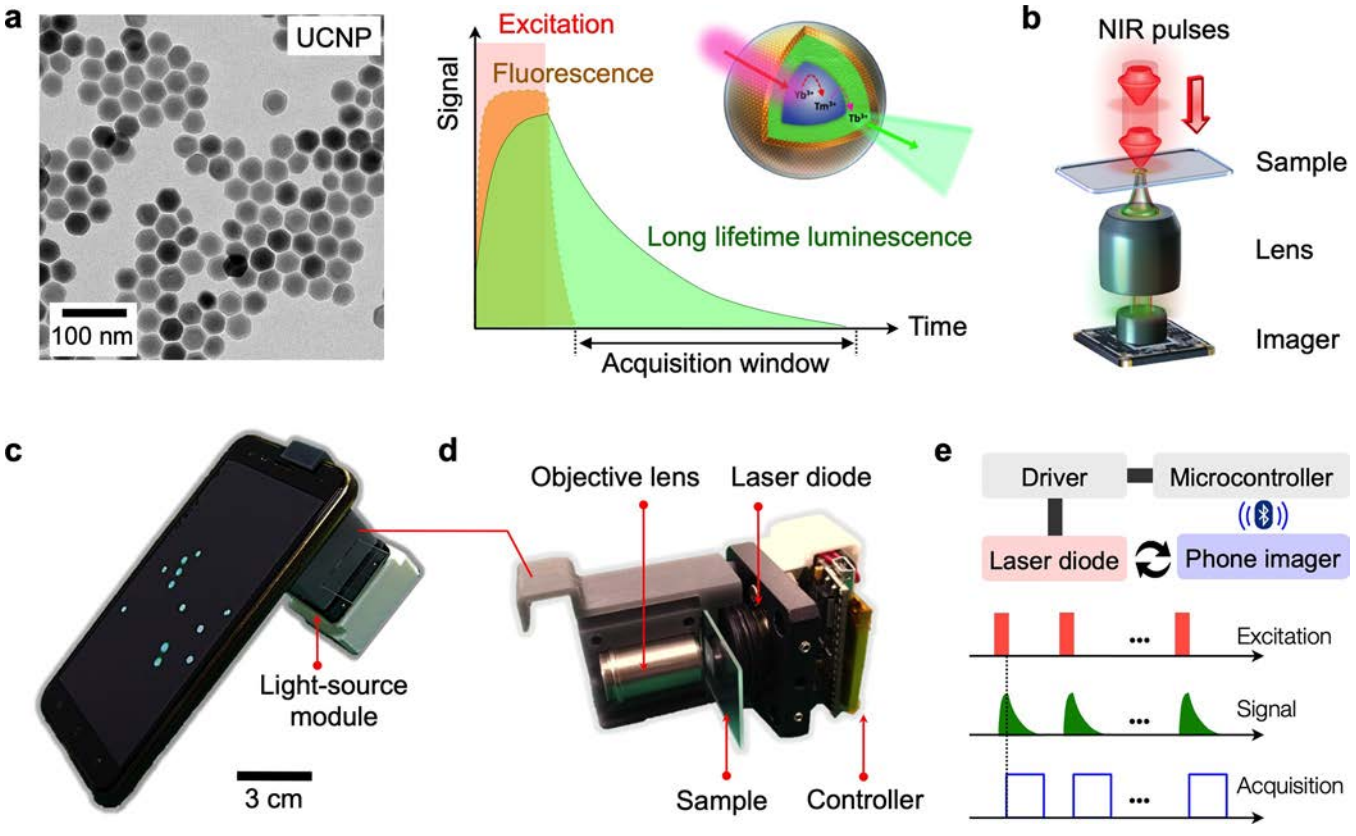

Figure 1. Luminescence upconversion *in vitro* diagnostics (LUCID). (a) The assay used upconversion nanoparticles (UCNPs; left) as reporters. Optical excitation and detection were temporally separated, as the particles can emit luminescent light after pulse excitation (right). (b) The LUCID scheme simplified the detection optical setup. An imager can directly image UCNP-labeled samples without using filter sets. (c) A mobile LUCID prototype was assembled by attaching an excitation module to a smartphone camera. (d) The excitation module consisted of a laser diode (emission, 980 nm), its control electronics, and beam shaping optics. (e) A microcontroller provided the triggering cues for particle excitation and image acquisition, ensuring that only the luminescence signal was recorded. Multiple frames could be averaged to improve overall image quality. For the prototype shown in (c), the controller communicated with the phone via Bluetooth to access its camera function.

luminescent light even after photoexcitation is turned off,[16−18] allowing for temporal decoupling between optical excitation and detection. Such imaging would be free from optical crosstalk and detector-saturation caused by high-intensity illumination. This in turn simplifies a system setup by enabling filterless imaging. Based on this principle, here we report on a compact luminescence platform, termed LUCID (luminescence compact *in vitro* diagnostics), for versatile POC molecular testing. We optimized both nanoparticles and their detection system. Specifically, we lengthened UCNPs' luminescence lifetime by controlling particle composition and built a portable, filterless imaging device around a smartphone. Applying the first prototype, we demonstrate highly sensitive detection across broad ranges of biological targets. LUCID detected soluble proteins (~0.5 pM) and nucleic acids (~0.1 pM) at high sensitivity, identified different bacterial species, and screened individual cancer cells. As for potential clinical applications, we used LUCID in the context of cervical cancer screening. Specimens obtained during colposcopy were subjected to LUCID for cellular detection, which reliably identified patients at high clinical risk for malignancy.

RESULTS AND DISCUSSION

LUCID Strategy and System Development. Photoexcited UCNPs emit both fluorescent and luminescent lights; fluorescence decays (<100 ns) soon after excitation is removed, whereas luminescence typically persists (Figure 1a). LUCID is designed to detect this long-lived luminescence only, which brings the following advantages: (i) imaging becomes free of artifacts associated with fluorescence detection (e.g., no bleed-through of excitation light, autofluorescence, photobleaching); (ii) repeated imaging can selectively amplify luminescence signal without increasing the background; and (iii) samples are directly imaged without need for optical filter sets (Figure 1b).

These merits enabled us to devise a compact, mobile LUCID system (Figures 1c and Supplementary Figure 1). Figure 1c shows a prototype built with a smartphone. We used a phone camera as a detector and interfaced it with an illumination source (Figure 1d). A snap-on module, housing a laser diode, optical lenses, and a microcontroller, was assembled and mounted over the phone camera. The microcontroller was programmed to synchronize operations between the laser diode and the phone camera, ensuring image acquisitions when the diode was turned off (Figure 1e). Specifically, the detection cycle started with NIR illumination (~5 ms). Excitation light was then turned off; the detector acquired the luminescence signal after a short time-delay (1 ms). The integration time was set to ~3 × the luminescence lifetime (τ), capturing >90% of the luminescence light.

Development of Nanoreagents. We next optimized UCNPs for LUCID applications, focusing on extending

DOI: 10.1021/acsnano.9b05634
ACS Nano 2019, 13, 11698−11706

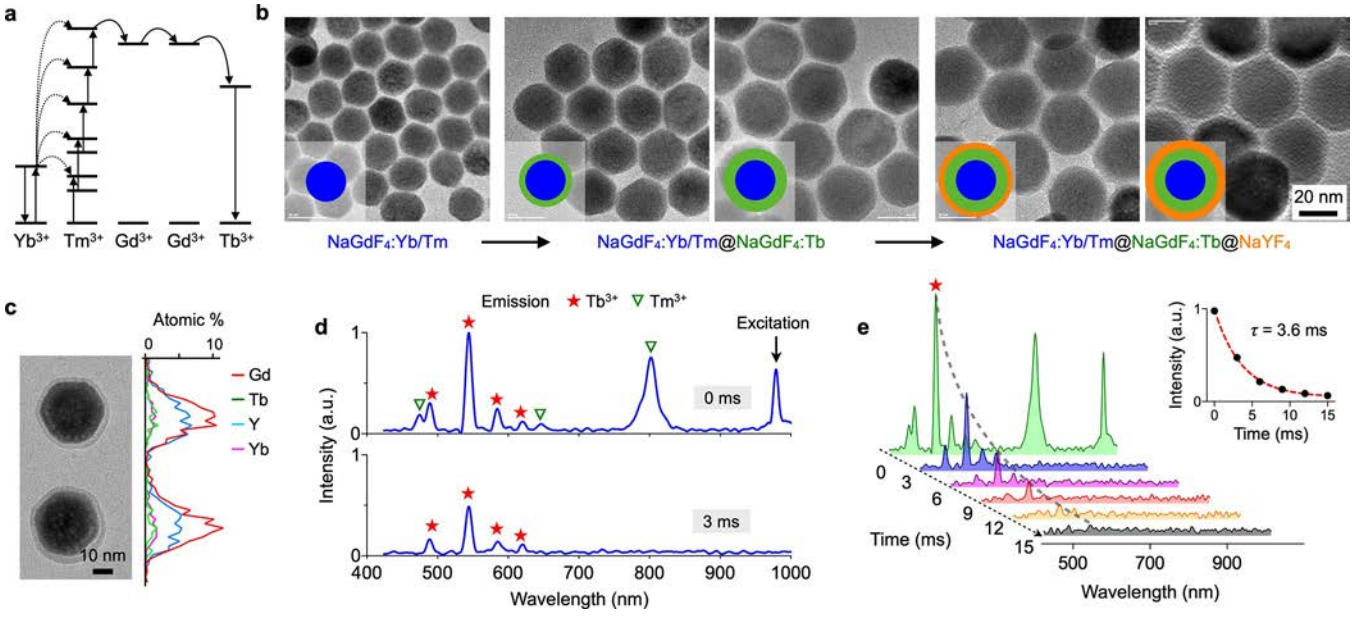

Figure 2. UCNPs optimized for LUCID. (a) Energy diagram. Yb^{3+} functions as a sensitizer to absorb NIR photons. The energy is accumulated in Tm^{3+} and then transferred to Tb^{3+} through Gd^{3+}. The particle *finally* emits photons with Tb^{3+} as an activator. (b) Synthetic route. We *first* synthesized a core particle ($NaGdF_4$:Yb/Tm) and then grew a shell of emission layer ($NaGdF_4$:Tb). The particle was further passivated with a protection layer ($NaYF_4$). (c) Energy dispersive X-ray spectroscopy (EDS) line scan con*firm*ed the incorporation of key elements (i.e., Gd, Tb, Y, Yb). (d) The emission spectra of the prepared UCNPs were measured. With the excitation light on, the particle showed emission peaks both from Tm^{3+} and Tb^{3+} (top). With the excitation o*ff*, the short-lived Tm^{3+} luminescence disappeared, but the signal from Tb^{3+} persisted (bottom). (e) Time-lapse detection revealed persistent luminescence from Tb^{3+}. The intensity was *fit*ted to a single-phase exponential decay function (inset). The decay time was 3.6 ± 0.4 ms.

luminescence lifetime. Conventional UCNPs tend to have short luminescence lifetimes (~microseconds).[19,20] Further extending luminescence lifetime is desirable; this can relax requirements for high-speed electronics and reduce electronic noise through longer signal integration. With a typical semiconductor imager, we estimated that the required luminescence lifetime should be in the range of milliseconds (see Supporting Information for details). As a luminescence source, we selected Tb^{3+} which is known to have a long luminescence lifetime (several milliseconds).[16,21] The material, however, required deep UV (254 nm) excitation, which would increase device costs (i.e., UV light source) and raise safety concerns. To provide UV-level excitation from NIR, we embedded Tb^{3+} into a UCNP substrate. Specifically, we used a Yb^{3+}/Tm^{3+} codoped $NaGdF_4$ as a core material; this particle can absorb 980 nm NIR light and emit deep UV photons through the upconversion process (Figure 2a). A Tb^{3+} doped shell was then grown around the core as an emitting layer.

Figure 2b shows the synthetic route. We first formed $NaGdF_4$:Yb/Tm core particles (diameter, 20 nm) via a thermal decomposition method (see Experimental Section).[22,23] Next, we encased the core with a shell of $NaGdF_4$:Tb. Through a dual-growth step, we thickened the shell (thickness, 5.8 nm) to enhance overall emission intensity. We finally passivated the particle with an inert $NaYF_4$ shell to protect Tb^{3+} from vibrational quenching by solvents. The particle had the overall diameter of 37 nm and showed high crystallinity (Supplementary Figure 2a) from epitaxial growth. Elemental mapping confirmed the incorporation of Tb^{3+} into the UCNP matrix (Figure 2c and Supplementary Figure 2). Synthesized UCNPs were made water-soluble through ligand exchange.[24,25] We incubated oleic-acid-capped UCNPs with excess amounts of poly(acrylic acid) (PAA). The carboxylic group on PAA was used for bioconjugation (Experimental Section).

We analyzed the optical properties of the prepared UCNPs. Aqueous suspensions of UCNPs were pulse-excited at 980 nm, and resulting emission spectra were measured. During excitation, we observed emission peaks from both Tm^{3+} (core) and Tb^{3+} (shell). The core emission (Tm^{3+}) had two major emission peaks from internal transitions (475 and 800 nm). These peaks decayed fast (<1 ms); the reported lifetimes were ~100 μs (475 nm) and ~340 μs (800 nm).[26] In contrast, Tb^{3+} emission peaks persisted much longer after excitation was turned off (Figure 2d). We determined Tb^{3+} luminescence lifetime via time-lapse measurements (Figure 2e). The emission at 546 nm, which is characteristic of Tb^{3+}, showed an exponential decay (Figure 2e, inset) with the lifetime τ = 3.6 ± 0.4 ms. This value was about 8-fold higher than the luminescence lifetime of conventional UCNPs ($NaYF_4$:Yb/Tm; Supplementary Figure 3).

Platform Characterization. We first tested LUCID using UCNP-coated microbeads (diameter, 10 μm). We compared bead images obtained through conventional fluorescence detection and LUCID (Figure 3a). Fluorescence images had lower signal-to-noise ratio (SNR = 2.6), likely due to the bleed-through from incident light. In contrast, LUCID was nearly background free, achieving higher SNR (= 7.3) even from single image acquisition (15 ms integration time). We further improved LUCID SNR through repeated time-gated imaging. For a given repetition number of N, the signal level would be linearly proportional to N, whereas system noise (mainly from dark currents of an imager) increases as $N^{1/2}$. Overall SNR is thus expected to scale as $N^{1/2}$. Repeated measurements on UCNP-coated microbeads confirmed such reasoning (Figure 3b) with overall SNR increasing (~$N^{1/2}$) with repeated

DOI: 10.1021/acsnano.9b05634
ACS Nano 2019, 13, 11698−11706

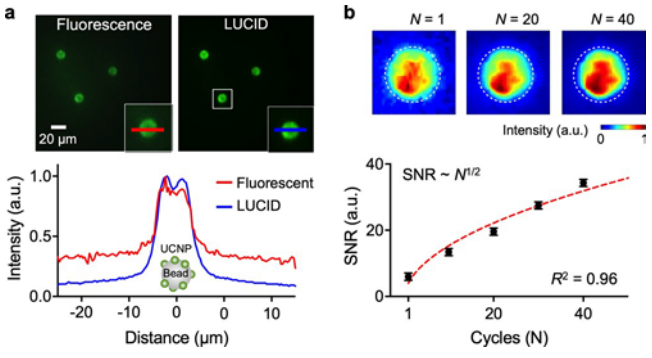

Figure 3. Characterization of LUCID signal. (a) Polystyrene microbeads (diameter 10 μm) were embedded with UCNPs and imaged in conventional *fl*uorescence and LUCID detection modes (top). LUCID had lower background than *fl*uorescence imaging, free from auto*fl*uorescence and scattering of incident light. The graph (bottom) shows intensity line scans of the same bead under the two detection modes. The signal level was normalized to its maximum. (b) The overall signal-to-noise ratio (SNR) of LUCID improved by repeating the luminescence imaging sequence (Figure 1e). The SNR scaled as $N^{1/2}$, where N is the cycle number. Each data point is from *fi*ve beads, and data is displayed as mean ± SD. The inset (top) shows pseudocolored images of an UCNP-embedded microbead (dotted circle).

excitation and integration. Note that this type of measurement was possible due to the high photostability of UCNPs (i.e., no photobleaching).

LUCID Molecular Assay Formats. We next adopted LUCID to detect different types of biological targets. We developed assays for three different types of targets: (i) soluble protein, (ii) bacterial RNA, and (iii) whole cells. For small molecular targets (e.g., soluble protein, nucleic acid), we used microbeads (diameter, 10 μm) as a solid substrate to capture molecules and subsequently label them with UCNPs (Supplementary Figure 4a). This approach effectively enhances detectable luminescence signal by locally concentrating UCNPs. The assay also benefits from three-dimensional diffusion of beads and target analytes, which shortens the traveling distance of targets before they are captured by affinity ligands. For cellular detection, we used cells as a substrate and directly labeled them with antibody-coated UCNPs.

We acquired multiple time-gated frames (N = 20) to produce a final image. For each frame, the laser diode was on for 5 ms; after 1 ms delay, signal was acquired for 10 ms. The total light illumination was short (~0.1 s) with no apparent thermal effect on samples. After the image acquisition, computing routines automatically located UCNP-labeled objects, either beads or cells, according to their light intensity, and calculated total intensity per object. As an analytical measure, we used the mean intensity value from ≥25 beads or 50 cells (see Experimental Section). A low magnification lens (20×) was sufficient for imaging while extending the system's field-of-view (350 × 350 μm^2).

For small molecule detection, we used thrombin and bacterial DNA as model targets. We conjugated microbeads with capture ligands: aptamers for thrombin (Supplementary Table 1) and oligonucleotides complementary to bacterial DNA. UCNPs were also modified with target-specific affinity ligands (see Experimental Section). To assess assay statistics, we generated calibration curves (signal vs analyte concentrations (Supplementary Figure 4b and c). Negative controls were prepared by incubating beads with UCNPs but without targets. LUCID achieved high sensitivity with a limit-of-detection (LOD) of 0.5 pM for thrombin and 0.1 pM for DNA. The dynamic range spanned about 3 orders of magnitude.

We extended the assay to pathogen analyses. A set of oligonucleotide pairs were prepared to detect different bacterial species. The oligonucleotides were complementary to the hypervariable region of 16S rRNA across different bacterial species (Supplementary Table 2).[27] RNA was extracted from bacteria samples and PCR-amplified to produce single-stranded DNA. Figure 4a shows a representative

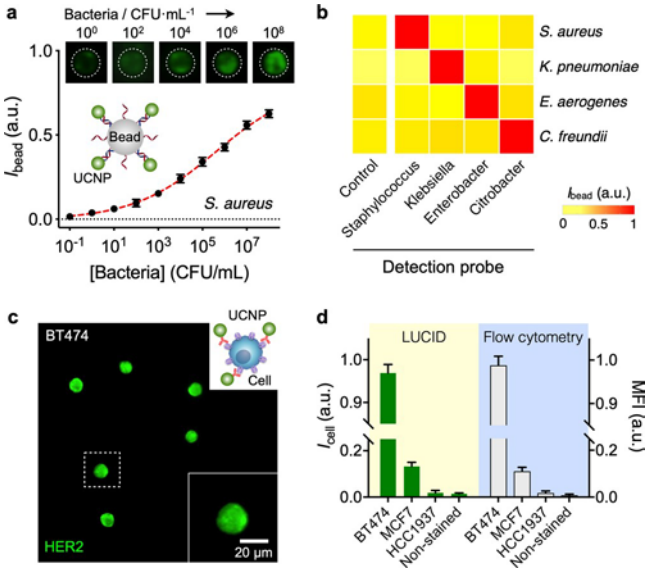

Figure 4. Versatile LUCID assays. (a) Bacteria detection. DNA targets from *S. aureus* were detected by LUCID. The detection limit reached down to single colony forming units (CFUs). Data are displayed as mean ± SD from triplicate measurements. The signal level was normalized to the maximum pixel intensity of the camera. (b) We further designed probe sets for four different bacteria genera (*Staphylococcus*, *Klebsiella*, *Enterobacter*, *Citrobacter*). LUCID displayed excellent signal contrast and achieved high specificity. For each sample, intensities from 25 beads were averaged. (c) Cell profiling. A panel of breast cancer cells (BT474, MCF7, HCC1937) were labeled with UCNPs conjugated with anti-HER2 antibodies, and imaged by LUCID. An image of BT474 cells is shown here; images of other cell lines are in Supplementary Figure 6. (d) LUCID results enabled quantitive cell profiling. The intensity (I_{cell}) of UCNP-labeled cells was reflective of HER2 expression and correlated (R^2 = 0.99) with the mean *fl*uorescent intensity (MFI) from *fl*ow cytometry. Intensities from 50 (LUCID) and 10^4 (*fl*ow cytometry) cells were averaged, and the data are displayed as mean ± SD.

example, the detection of *Staphylococcus aureus*. Titration experiments showed that the sensitivity was close to single colony forming units (CFUs). We next applied the assay to identify different bacterial species (Figure 4b). LUCID showed high detection selectivity, superior to that of conventional SBYR green-based PCR (Supplementary Figure 5). This could be attributed to the sandwich hybridization employed in the UCNP assay; both capture and detection probes should bind to their target to emit the luminescence signal.

DOI: 10.1021/acsnano.9b05634
ACS Nano 2019, 13, 11698−11706

We finally demonstrated cell profiling with LUCID. Human breast cancer cell lines (BT474, MCF7, HCC1937) were labeled with immuno-UCNPs recognizing the human epidermal growth factor receptor 2 (HER2)/*neu*. Differential luminescence signal was observed per cell line (Figure 4c and Supplementary Figure 6), reflective of varying HER2 levels. The average luminescence signal (from 50 cells) correlated linearly with mean fluorescence intensity (MFI) by flow cytometry ($R^2 = 0.99$; Figure 4d).

LUCID Application with Clinical Specimens. To explore LUCID's potential for clinical application, we identified effective yet feasible cervical cancer screening as an unmet need in point-of-care settings. Cervical cancer incurs high incidence and mortality rates in many resource-limited countries[28] which often lack robust early screening infrastructures. We reasoned that the portable LUCID system could effectively triage suspicious or high-risk cases. This decentralized strategy could potentially offset pathology bottlenecks and reduce repeated patient visits to central clinics, often complicated by geographical and/or socioeconomic constraint.[29]

We obtained excess cervical specimens through brushings or biopsies during colposcopic evaluation. Eleven patients with previously abnormal Pap smear results were recruited. We labeled cellular samples with a cocktail of UCNPs specific to EpCAM, CD44 or Trop2; these markers were chosen for their elevated expression in cervical cancer as described in the literature and Human Protein Atlas.[30−32] LUCID resolved individual cells (Figure 5a) and was able to quantify their luminescence intensities. Patient specimens were also independently assessed via conventional cytopathology, which classified them into three groups: "high risk", "low risk", or "benign" (Figure 5b, top row). On average, we observed higher luminescence signal with increased clinical risk (Figure 5b). Notably, the mean intensity per cell (I_{cell}) could serve as a classification metric (Figure 5c), significantly different among risk groups (Sidak's multiple comparison test).

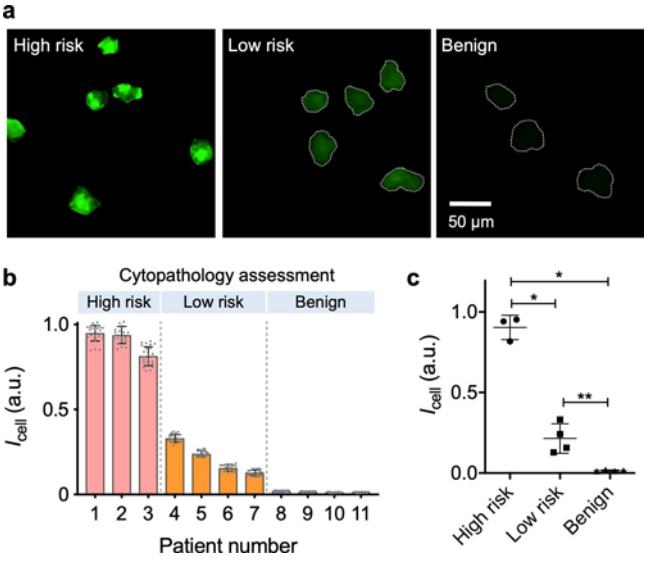

Figure 5. LUCID screening of cervical cancer. (a) Human cervical brushing samples were labeled with a cocktail of UCNPs specific to EpCAM, CD44, and Trop-2. Representative LUCID images from high-risk (cervical intraepithelial neoplasia/CIN 2, 3), low-risk (CIN 1), and benign patient samples are shown. (b) LUCID profiling results from 11 patient samples are displayed in a waterfall plot. For each sample, intensities from 25 labeled cells were measured; risk levels were independently assessed by cytopathology. Increased risk levels were found to be associated with higher LUCID signals. (c) The average cellular intensity was significantly different among high risk, low risk, and benign groups (Sidak's multiple comparisons test): $*p < 0.0001$; $**p = 0.0094$.

CONCLUSIONS

Deploying low-cost mobile diagnostics can mitigate healthcare disparities in LMIC settings where pathology bottlenecks, limited resources, and logistic barriers delay disease diagnoses and often lead to over/undertreatment.[33] Such tests would also benefit underserved populations in developed countries; in the United States, for example, a quarter of the population live in rural areas, but only 10% of physicians practice there.[34] The developed LUCID platform can help tackle diagnostic challenges in such regions: (i) sensing is robust against autofluorescence and optical scattering; (ii) filter-free, simple optics renders the assay system cost-effective and easy to maintain, and (iii) the platform can perform onsite detection of diverse molecular targets. The underlying technical innovation sought to engineer nanoparticles with long-lived luminescence and integrate them into compact, time-gated imaging devices. Our pilot studies confirmed that LUCID's analytical results are comparable or superior to costlier laboratory tests demanding greater skill sets (i.e., qPCR, flow cytometry, cytopathology).

We used upconversion nanoparticles (UCNPs) that have emerged as a new class of nanomaterials for biosensing.[35,36] Doped with lanthanide ions, UCNPs absorb multiple near-infrared (NIR) photons and emit visible or ultraviolet (UV) light. The parity forbidden nature of 4f−4f transitions of lanthanide ions delays the spontaneous photon emission, opening a temporal window to excitation-free imaging. Luminescence is also highly stable without photobleaching or blinking.[37,38] These favorable optical properties have motivated diverse applications of UCNPs for *in vivo* imaging.[17,20,39−42] One drawback of UCNPs is their low quantum yields (QYs; generally <1%).[43] We expect that our Tb-doped UCNPs have a similar QY, although the exact value is yet to be determined. UCNP QYs increase with higher excitation power[44] but at the risk of photothermal damage on samples. In LUCID, we compensated for the UCNPs' low QY through repeated time-gated imaging (Figure 1e), exploiting the particles' high photostability. Indeed, signal quality progressively improved with acquisition numbers (Figure 3b). Furthermore, by syncing the light source to the camera, the total acquisition time was <2 s.

The current system can be further refined, particularly through particle engineering. First, we envision synthesizing a panel of UCNPs for multiplexed molecular detection. The luminescence color can be tuned by varying the composition of lattice atoms and dopant ions.[16,45−47] UCNPs also have a narrower width of emission peak (10−20 nm) than that of quantum dots or organic dyes.[48,49] Combined, these features would allow LUCID to resolve different particles types through simultaneous multicolor detection. Second, we could render UCNPs excitable at longer wavelengths (>1100 nm) wherein the quantum efficiency of semiconductor imagers becomes negligible (due to indirect bandgap of silicon). For example, the excitation wavelength of 1530 nm has been demonstrated when UCNPs were doped with Er and Tm.[50] Under this condition, LUCID could directly detect particles even with

DOI: 10.1021/acsnano.9b05634
ACS Nano 2019, 13, 11698−11706

continuous illumination, which will make the system even simpler and easier to use. Third, one could explore the use of phosphorescent particles that exhibit long-lasting (minutes to hours) afterglow. The same time-gated imaging can detect these particles but with longer integration time than that of UCNPs; this would help further enhance the SNR. One technical challenge is establishing new fabrication methods, different from physical grinding of crystals,[51] to synthesize monodisperse, bioconjugatable phosphorescent particles.[52] These advances in nanoengineering will propel LUCID as an affordable and versatile diagnostic tool to improve and decentralize health care delivery in resource-limited settings.

EXPERIMENTAL SECTION

LUCID System Setup. The excitation light source consisted of a 980 nm laser diode (LDM-0980-002w-35, Roithner LaserTechnik), an aspheric lens (focal length f = 11 mm, numerical aperture NA = 0.25; C22MB, Thorlabs), and an objective lens (20×, Olympus). Two types of signal detectors, a CMOS imager (2592 × 1944 pixels; DFM 72BUC02-ML; The Image Source) or a smartphone (Galaxy S5, Samsung) with a CMOS imager (1334 × 750 pixels), were used. A microcontroller unit (Arduino MEGA 2560) was programmed to control the light source and the camera. The laser diode was turned on for 5 ms to excite UCNPs and then turned off. Following 1 ms delay, the camera was on for 10 ms to acquire a luminescence image, and the data were transferred to a computer (~70 ms). The acquisition time for a single cycle was thus <90 ms. We repeated the cycle 20 times. The total illumination time per image was thus ~0.1 s, which led to the incident light energy of ~20 mJ per sample. Considering the typical sample geometry (350 × 350 × 10 μm^3) and the absorption coefficient of water (α = 5 m^{-1} at λ = 980 nm), the energy absorbed by water would be on the order of 10^{-6} J (= 10 μm × 5 m^{-1} × 20 mJ), and the resulting increase in the sample temperature is on the order of 0.1 °C. The light-source was powered by a battery (9 V D-cell) or through USB connection.

Synthesis of $NaGdF_4$:Yb/Tm Core UCNPs. We synthesized UCNPs according to the previously reported methods with minor modifications.[23] Here, 0.5 mmol of gadolinium(III) acetate hydrate (99.9%, Aldrich), 0.49 mmol of ytterbium(III) acetate tetrahydrate (99.9%, Aldrich), and 0.01 mmol of thulium(III) acetate hydrate (99.9%, Aldrich) were mixed with 10 mL of oleic acid (technical grade, 90%, Aldrich) and 15 mL of 1-octadecene (technical grade, 90%, Aldrich) in a 100 mL three-neck round-bottom flask. The reaction mixture was heated at 150 °C with stirring for 40 min to remove residual water and oxygen and then cooled to room temperature. A 10 mL methanol solution containing 2.5 mmol of NaOH (98%, Aldrich) and 3.3 mmol of NH_4F (98%, Aldrich) was added to the reaction vessel. The reaction mixture was stirred for 30 min at 50 °C and then heated to 100 °C under vacuum with stirring for 30 min to remove methanol. The temperature was then elevated to 280 °C at the ramping rate of 10 °C/min and then kept constant for 90 min under Ar. The resulting solution was then cooled to room temperature. The UCNPs were precipitated by adding ethanol and retrieved by centrifugation. The purification procedure was repeated two more times to remove excess surfactant and solvent. The purified UCNPs were dispersible in organic solvents such as hexane and chloroform.

Synthesis of $NaGdF_4$:Yb/Tm@$NaGdF_4$:Tb Core−Shell UCNPs. Here, 0.85 mmol of gadolinium(III) acetate hydrate and 0.15 mmol of terbium(III) acetate hydrate (99.9%, Aldrich) were mixed with 10 mL of oleic acid and 15 mL of 1-octadecene in a 100 mL three-neck round-bottom flask. The reaction mixture was heated at 150 °C with stirring for 40 min to remove residual water and oxygen and then cooled to room temperature. A solution of core UCNPs in hexane was injected to the reaction vessel. A 10 mL methanol solution containing 2.5 mmol of NaOH and 3.3 mmol of NH_4F was added into the reaction vessel. The reaction mixture was stirred for 30 min at 50 °C and then heated to 100 °C under vacuum with stirring for 30 min to remove methanol. Then the reaction mixture was heated to 280 °C at a ramping rate of 10 °C/min, and then kept at that temperature for 90 min under Ar. The resulting solution was then cooled to room temperature. The prepared UCNPs were collected and washed as described above. The shell coating was repeated one more time to form the thick Tb-doped shell.

Synthesis of $NaGdF_4$:Yb/Tm@$NaGdF_4$:Tb@$NaYF_4$ Core−Multishell UCNPs. Here, 1 mmol of yttrium(III) acetate hydrate (99.9%, Aldrich) was mixed with 7.5 mL of oleic acid and 17.5 mL of 1-octadecene in a 100 mL three-neck round-bottom flask. We applied the same reaction condition as those for Tb-doped shell coating, but we used $NaGdF_4$:Yb/Tm@$NaGdF_4$:Tb UCNPs as seed particles.

Characterization of UCNPs. The shape, structure, and composition of synthesized nanoparticles were analyzed via transmission electron microscopy (TEM; JEOL 2100, JEOL USA). High resolution TEM (HRTEM) images and energy dispersive X-ray spectroscopy (EDS) were obtained using a JEOL 2100F apparatus equipped with an EDS detector (X-MAX 80T, Oxford). Optical properties of particles were measured by using a fluorescent plate reader (TECAN Safire 2).

Ligand Exchange with Poly(acrylic acid). The surface modification of UCNPs was performed using poly(acrylic acid) (PAA, M_w 1800, Aldrich).[25] A volume of 2 mL of UCNPs in chloroform (15 mg/mL) was slowly added to 2 mL of PAA in ethanol (150 mg/mL) with overnight stirring. The solution was centrifuged at 20 000g for 10 min. After washing with ethanol and deionized water for several times, the resulting UCNPs were redispersed in deionized water under sonication.

UCNP-Embedded Beads. A volume of 22 μL of polystyrene beads (Polybead Carboxylate Microspheres, 10 μm, Polysciences) was added into a mixture of butanol (9.5 mL) and chloroform (0.5 mL). After 30 min incubation with stirring, 20 μL of UCNPs in THF (10 mg/mL) was added to the bead solution. After 60 min incubation, the beads were washed using ethanol several times (3000g for 5 min) and then dispersed in deionized water.

Capture Probe Conjugation on the Beads. An amount of 10 mg of streptavidin coated polystyrene beads (SuperAvidin Coated Microspheres, 9.94 μm, Bangs Laboratories) was washed three times (3000g for 3 min) using Tris buffer (20 mM pH 7.5 Tris, 1 mM EDTA, 1 M NaCl, 0.0005% Triton X-100) and then dispersed in 1 mL of Tris buffer. The beads were incubated with 40 μL of biotinylated capture probes (40 nmol, Integrated DNA Technologies) for 60 min at room temperature. After incubation, the beads were washed four times using Tris buffer and dispersed in 1 mL of Tris buffer. The amount of oligonucleotide probes per bead was quantified using the Qubit ssDNA assay kit and Qubit 2.0 fluorometer (Thermo Fisher Scientific). The average number of capture ligands was ~10^6 per bead.

Conjugation of Oligonucleotide Probes on UCNPs. Volumes of 50 μL of detection probes (50 nmol, Integrated DNA Technologies) and 0.1 mL of EDC (1 mg, 1-ethyl-3-(3-(dimethylamino)propyl) carbodiimide hydrochloride, Thermo Fisher Scientific) were added to 0.5 mL of PAA coated UCNPs (~30 mg), and they were incubated for 60 min at room temperature. Next, 0.1 mL of EDC (1 mg) was added to the reaction mixture, and then the mixture was incubated overnight. After incubation, the nanoparticles were centrifuged at 20 000g for 10 min. The precipitated UCNPs were redispersed in Tris-Tween 20 (125 mL of 1 M pH 8 Tris, 0.1 g of Tween 20, 375 mL of deionized water) under sonication. The purification process was repeated four times, and UCNPs were dispersed in pH 8 Tris-HCl (20 mM) under sonication. The amount of oligonucleotide probes per nanoparticle (10−20 per particle) was quantified using the Qubit ssDNA assay kit and Qubit 2.0 fluorometer (Thermo Fisher Scientific).

Conjugation of Antibodies on UCNPs. The following antibodies were purchased: anti-HER2 (clone 24D2, Biolegend); anti-EpCAM (clone MAB9601, R&D Systems); anti-CD44 (clone IM7, Biolegend); Trop 2 (clone 162−46.2, Abcam). Volumes of 20 μL of antibody (1 mg/mL) and 0.1 mL of EDC (2 mg/mL) were added to 0.5 mL of PAA coated UCNPs (~20 mg), and they were incubated

DOI: 10.1021/acsnano.9b05634
ACS Nano 2019, 13, 11698−11706

for 2 h at room temperature. After incubation, the nanoparticles were centrifuged at 20 000*g* for 10 min. The precipitated UCNPs were redispersed in 1 mL of 1× PBS.

Thrombin Detection. Capture beads were dispersed in Tris-HCl buffer (50 mM pH 7.4 Tris-HCl, 1 mM $MgCl_2$, 5 mM KCl, 0.1% BSA). A volume of 40 μL of capture beads was incubated with 10 μL of thrombin solution (Human alpha-Thrombin, Haematologic Technologies) for 30 min at room temperature. After incubation, the beads were purified four times using a 5 μm centrifugal filter, and they were dispersed in 40 μL of Tris-HCl buffer. Then 40 μL of beads was incubated with 60 μL of detection UCNPs for 30 min at room temperature. Excess UCNPs were removed via centrifugation (1 min, 60*g*) using a 5 μm centrifugal filter. Collected beads were dispersed in 50 μL of Tris-HCl buffer.

DNA Detection. A volume of 40 μL of capture beads was diluted with 50 μL of Tris buffer. The beads were incubated with 10 μL of synthetic DNA specific for *S. aureus* (Integrated DNA Technologies) for 30 min at room temperature. After incubation, the beads were purified four times using a 0.45 μm centrifugal filter (94*g* for 3 min) and were dispersed in 40 μL of Tris buffer. The beads were incubated with 60 μL of detection UCNPs for 30 min at room temperature. Excess UCNPs were removed via centrifugation (1 min, 60*g*) using a 5 μm centrifugal filter. Beads were then dispersed in 100 μL of Tris-buffered saline (25 mM Tris, 150 mM NaCl).

Bacterial Detection. Four different bacteria species were purchased from the American Type Culture Collection and grown to mid log phase in suitable media: *Staphylococcus aureus* (#25923) in Staphylococcus broth (BD Biosciences); *Klebsiella pneumoniae* (#43816) in trypticase soy broth; *Enterobacter aerogenes* (#13048), *Citrobacter freundii* (#6879) in nutrient broth (BD Biosciences). For RNA extraction, bacteria were centrifuged at 6,000 × g for 10 min and pellets were treated with the preheated Trizol (Life Technologies). The resuspended cells were transferred to 2 mL Safe-Lock tubes (Eppendorf) containing sterilized disruptor beads (0.1 mm, Scientific Industries), and lysed using a vortex mixer. After centrifugation, the supernatant was transferred to a new tube and mixed with an equal volume of ethanol. The mixture was processed by Direct-zol RNA kits (Zymo Research), following manufacturer's protocol. With the extracted RNA samples, the representative single-stranded cDNA was synthesized using random priming with Promega's Reverse Transcription System per manufacturer's protocol. The asymmetric PCR was then carried out in a total volume of 25 μL containing 2.5 μL of cDNA, 0.8 μM excess primer and 0.08 μM limiting primer (Supplementary Table 2), 1× PCR reaction buffer (20 mM Tris-HCl, 20 mM KCl, 5 mM $(NH_4)_2SO_4$, and 2 mM $MgCl_2$), 0.2 mM of each dNTP, and 2 U Maxima Hot Start Taq DNA polymerase (Thermo Scientific). The reaction tubes were heated to 94 °C for 2 min, followed by 35 or 40 cycles of 5 s at 94 °C, 15 s at 56 °C, and 15 s at 72 °C, and then a final 10 min extension step at 72 °C.

SYBR Green-Based Quantitative PCR (qPCR). The qPCR was carried out on 7500 Fast Real-time PCR system (Life Technologies) in a total reaction volume of 20 μL containing 2.5 μL of cDNA derived from *in vitro* cultured bacteria (~10^6 CFU/mL), 0.5 μM of each primer (Supplementary Table 2), and 1× SYBR Select Master mix (Life Technologies). Thermal cycling was then carried out with the following conditions: Initiation (95 °C, 2 min); 40 cycles of denaturation (95 °C, 5 s); annealing (56 °C, 15 s); extension (72 °C, 30 s). The threshold cycle (C_t) values were obtained using the 7500 Fast software. No-template control (NTC) remained undetected, not crossing the established threshold for 40 cycles, which was arbitrarily given a C_t value of 41. The ΔC_t was calculated by subtracting the C_t value of the specimen from the Ct value of NTC.

Cell Preparation for LUCID. A panel of human breast cancer cell lines were purchased (ATCC) and grown in the vendor-recommended media: BT474 (Hybri-Care Medium 46-X with 0.15% $NaHCO_3$, ATCC); MCF7 (Eagle's minimum essential medium 30-2003 with 0.1% human recombinant insulin, ATCC); HCC1937 (RPMI-1640, Corning). All media were supplemented with 10% heat inactivated fetal bovine serum (Gibco) and 1% penicillin−streptomycin (5000 U/mL, Gibco). Cells were maintained at 37 °C in a humidified atmosphere containing 5% CO_2. At about 80% confluence, cells were washed, trypsinized, and resuspended to a concentration of ~10^6 cells/mL in PBS containing 1% BSA. Cells were incubated with 200 μg/mL HER2 conjugated UCNP for 20 min at room temperature, washed via centrifugation (350*g*, 5 min), and resuspended in PBS. About 10 μL of cell solution (~10^5 cells/mL) was placed on a plastic slide for LUCID imaging.

Flow Cytometry. About 10^5 cells were used for flow cytometry. Cells were suspended in 1% BSA PBS and incubated with 1 μg/mL anti-human HER2 (BioLegend, 324401) antibody for 30 min at room temperature. Cells were then triple washed with 1% BSA PBS, incubated with 1 μg/mL FITC anti-mouse IgG antibody (BioLegend, 406001), and triple washed for flow cytometry measurements. Control samples were prepared and labeled similarly using 1 μg/mL mouse IgG1, κ isotype antibody (BioLegend, 401401) and 1 μg/mL FITC anti-mouse IgG antibody. Fluorescent signal was measured by using a CytoFLEX instrument (Beckman Coulter). The mean fluorescence intensity of 10 000 cells was determined using FlowJo software.

Clinical Samples. The clinical study was approved by the Partners Healthcare Institutional Review Board. We obtained informed consent from adult women referred to the MGH Colposcopy Clinic for cervical biopsy or loop electrosurgical excision procedure (LEEP). One clinical provider (M.A.) performed all cervical procedures and provided excess or otherwise discarded ectocervical or endocervical brushing or biopsy specimens. Study specimens were collected conventionally before loop excision to avoid potential tissue alteration. Cells were rinsed in sterile PBS and concentrated via centrifugation (300*g*, 5 min). Pelleted cells were treated with collagenase 1 and 2 (5−10 mg/mL; Sigma-Aldrich) at 37 °C, gently agitated and dispersed. Treated cells were washed in PBS and targeted with a cocktail of three UCNP probes, each specific to EpCAM, CD44, and Trop-2. After 20 min incubation at room temperature, samples were washed via centrifugation (350*g*, 5 min). Cell pellets were resuspended in PBS (100 μL). We used about 10 μL of samples for LUCID. All experiments were conducted blind to the clinical interpretation of risk.

ASSOCIATED CONTENT

Supporting Information

The Supporting Information is available free of charge on the ACS Publications website at DOI: 10.1021/acsnano.9b05634.

> Schematic of LUCID device; microscopic and elemental analyses of UCNPs; luminescence lifetime of conventional UCNPs; LUCID assay for soluble molecular targets; comparison of bacteria detection; cell profiling with LUCID; aptamer sequences used for thrombin detection; DNA sequences used for bacterial detection (PDF)

AUTHOR INFORMATION

Corresponding Authors

*E-mail: hlee@mgh.harvard.edu.

*E-mail: rweissleder@mgh.harvard.edu.

ORCID

Yong Il Park: 0000-0003-3167-4908

Ki Soo Park: 0000-0002-0545-0970

Ralph Weissleder: 0000-0003-0828-4143

Hakho Lee: 0000-0002-0087-0909

Author Contributions

C.-H.H., Y.I.P., and H.-Y.L. contributed equally to this work. C.-H.H., Y.I.P., C.M.C, R.W., and H.L. designed the research. Y.I.P. synthesized and characterized UCNPs. C.-H.H. built the detection devices. C.-H.H., Y.I.P., H.-Y.L., D.P., and K.S.P. performed bioassays. C.M.C. and R.W. designed the clinical

DOI: 10.1021/acsnano.9b05634
ACS Nano 2019, 13, 11698−11706

study. H.-Y.L., M.A., D.P., C.M.C. collected and processed the clinical samples. C.-H.H., Y.I.P., C.M.C, R.W., and H.L. wrote the paper with inputs from all authors.

Notes

The authors declare no competing financial interest.

ACKNOWLEDGMENTS

This work was supported in part by U.S. NIH Grants R01CA229777 (H.L.), U01CA233360 (H.L., C.M.C), MGH Scholar Fund (H.L.), DoD-W81XWH1910199 (H.L.), DoD-W81XWH1910194 (H.L.), and MGH Fund for Medical Discovery Fellowship (H.-Y.L.); Taiwan MOST Grants 107-2112-M-008-001 (C.-H.H.) and NSC104-2917-I-564-086 (H.-Y.L.); NRF Grant 2017R1C1B1010703 (Y.I.P.).

REFERENCES

(1) *Global Health Estimates 2016: Deaths by Cause, Age, Sex, by Country and by Region, 2000−2016*; World Health Organization: Geneva, 2018.

(2) Robertson, J.; Barr, R.; Shulman, L. N.; Forte, G. B.; Magrini, N. Essential Medicines for Cancer: Who Recommendations and National Priorities. *Bull. World Health Organ.* 2016, *94*, 735−742.

(3) Klein, E. Y.; Van Boeckel, T. P.; Martinez, E. M.; Pant, S.; Gandra, S.; Levin, S. A.; Goossens, H.; Laxminarayan, R. Global Increase and Geographic Convergence in Antibiotic Consumption Between 2000 and 2015. *Proc. Natl. Acad. Sci. U. S. A.* 2018, *115*, E3463−E3470.

(4) Drain, P. K.; Hyle, E. P.; Noubary, F.; Freedberg, K. A.; Wilson, D.; Bishai, W. R.; Rodriguez, W.; Bassett, I. V. Diagnostic Point-of-Care Tests in Resource-Limited Settings. *Lancet Infect. Dis.* 2014, *14*, 239−249.

(5) Urdea, M.; Penny, L. A.; Olmsted, S. S.; Giovanni, M. Y.; Kaspar, P.; Shepherd, A.; Wilson, P.; Dahl, C. A.; Buchsbaum, S.; Moeller, G.; Hay Burgess, D. C. Requirements for High Impact Diagnostics in the Developing World. *Nature* 2006, *444* (Suppl 1), 73−79.

(6) Li, J.; Macdonald, J. Multiplexed Lateral Flow Biosensors: Technological Advances for Radically Improving Point-of-Care Diagnoses. *Biosens. Bioelectron.* 2016, *83*, 177−192.

(7) Pollock, N. R.; Rolland, J. P.; Kumar, S.; Beattie, P. D.; Jain, S.; Noubary, F.; Wong, V. L.; Pohlmann, R. A.; Ryan, U. S.; Whitesides, G. M. A Paper-Based Multiplexed Transaminase Test for Low-Cost, Point-of-Care Liver Function Testing. *Sci. Transl. Med.* 2012, *4*, 152ra129.

(8) Singh, A. T.; Lantigua, D.; Meka, A.; Taing, S.; Pandher, M.; Camci-Unal, G. Paper-Based Sensors: Emerging Themes and Applications. *Sensors* 2018, *18*, 2838.

(9) D'Ambrosio, M. V.; Bakalar, M.; Bennuru, S.; Reber, C.; Skandarajah, A.; Nilsson, L.; Switz, N.; Kamgno, J.; Pion, S.; Boussinesq, M.; Nutman, T. B.; Fletcher, D. A. Point-of-Care Quantification of Blood-Borne Filarial Parasites With a Mobile Phone Microscope. *Sci. Transl. Med.* 2015, *7*, 286re4.

(10) Breslauer, D. N.; Maamari, R. N.; Switz, N. A.; Lam, W. A.; Fletcher, D. A. Mobile Phone Based Clinical Microscopy for Global Health Applications. *PLoS One* 2009, *4*, No. e6320.

(11) Zhu, H.; Mavandadi, S.; Coskun, A. F.; Yaglidere, O.; Ozcan, A. Optofluidic Fluorescent Imaging Cytometry on a Cell Phone. *Anal. Chem.* 2011, *83*, 6641−6647.

(12) Im, H.; Castro, C. M.; Shao, H.; Liong, M.; Song, J.; Pathania, D.; Fexon, L.; Min, C.; Avila-Wallace, M.; Zurkiya, O.; Rho, J.; Magaoay, B.; Tambouret, R. H.; Pivovarov, M.; Weissleder, R.; Lee, H. Digital Diffraction Analysis Enables Low-Cost Molecular Diagnostics on a Smartphone. *Proc. Natl. Acad. Sci. U. S. A.* 2015, *112*, 5613−5618.

(13) Coskun, A. F.; Ozcan, A. Computational Imaging, Sensing and Diagnostics for Global Health Applications. *Curr. Opin. Biotechnol.* 2014, *25*, 8−16.

(14) Lee, S. A.; Erath, J.; Zheng, G.; Ou, X.; Willems, P.; Eichinger, D.; Rodriguez, A.; Yang, C. Imaging and Identification of Waterborne Parasites Using a Chip-Scale Microscope. *PLoS One* 2014, *9*, No. e89712.

(15) Boppart, S. A.; Richards-Kortum, R. Point-of-Care and Point-of-Procedure Optical Imaging Technologies for Primary Care and Global Health. *Sci. Transl. Med.* 2014, *6*, 253rv2.

(16) Wang, F.; Deng, R.; Wang, J.; Wang, Q.; Han, Y.; Zhu, H.; Chen, X.; Liu, X. Tuning Upconversion Through Energy Migration in Core-Shell Nanoparticles. *Nat. Mater.* 2011, *10*, 968−973.

(17) Lu, Y.; Lu, J.; Zhao, J.; Cusido, J.; Raymo, F. M.; Yuan, J.; Yang, S.; Leif, R. C.; Huo, Y.; Piper, J. A.; Paul Robinson, J.; Goldys, E. M.; Jin, D. On-the-Fly Decoding Luminescence Lifetimes in the Microsecond Region for Lanthanide-Encoded Suspension Arrays. *Nat. Commun.* 2014, *5*, 3741.

(18) Wen, S.; Zhou, J.; Zheng, K.; Bednarkiewicz, A.; Liu, X.; Jin, D. Advances in Highly Doped Upconversion Nanoparticles. *Nat. Commun.* 2018, *9*, 2415.

(19) Ding, M.; Chen, D.; Ma, D.; Liu, P.; Song, K.; Lu, H.; Ji, Z. Tuning the Upconversion Luminescence Lifetimes of Kyb_2F_7:Ho^{3+} Nanocrystals for Optical Multiplexing. *ChemPhysChem* 2015, *16*, 3784−3789.

(20) Lu, Y.; Zhao, J.; Zhang, R.; Liu, Y.; Liu, D.; Goldys, E. M.; Yang, X.; Xi, P.; Sunna, A.; Lu, J.; et al. Tunable Lifetime Multiplexing Using Luminescent Nanocrystals. *Nat. Photonics* 2014, *8*, 32−36.

(21) Zheng, W.; Zhou, S.; Chen, Z.; Hu, P.; Liu, Y.; Tu, D.; Zhu, H.; Li, R.; Huang, M.; Chen, X. Sub-10 nm Lanthanide-Doped CaF_2 Nanoprobes for Time-Resolved Luminescent Biodetection. *Angew. Chem., Int. Ed.* 2013, *52*, 6671−6676.

(22) Su, Q.; Han, S.; Xie, X.; Zhu, H.; Chen, H.; Chen, C. K.; Liu, R. S.; Chen, X.; Wang, F.; Liu, X. The Effect of Surface Coating on Energy Migration-Mediated Upconversion. *J. Am. Chem. Soc.* 2012, *134*, 20849−20857.

(23) Wang, F.; Deng, R.; Liu, X. Preparation of Core-Shell $NaGdF_4$ Nanoparticles Doped With Luminescent Lanthanide Ions to Be Used as Upconversion-Based Probes. *Nat. Protoc.* 2014, *9*, 1634−1644.

(24) Yi, G.-S.; Chow, G.-M. Water-Soluble $NaYF_4$: Yb, Er (Tm)/$NaYF_4$/polymer Core/Shell/Shell Nanoparticles with Significant Enhancement of Upconversion Fluorescence. *Chem. Mater.* 2007, *19*, 341−343.

(25) You, M.; Zhong, J.; Hong, Y.; Duan, Z.; Lin, M.; Xu, F. Inkjet Printing of Upconversion Nanoparticles for Anti-Counterfeit Applications. *Nanoscale* 2015, *7*, 4423−4431.

(26) Wang, Y.; Deng, R.; Xie, X.; Huang, L.; Liu, X. Nonlinear Spectral and Lifetime Management in Upconversion Nanoparticles by Controlling Energy Distribution. *Nanoscale* 2016, *8*, 6666−6673.

(27) Chung, H. J.; Castro, C. M.; Im, H.; Lee, H.; Weissleder, R. A Magneto-DNA Nanoparticle System for Rapid Detection and Phenotyping of Bacteria. *Nat. Nanotechnol.* 2013, *8*, 369−375.

(28) Schiffman, M.; Solomon, D. Clinical Practice. Cervical-Cancer Screening with Human Papillomavirus and Cytologic Cotesting. *N. Engl. J. Med.* 2013, *369*, 2324−2331.

(29) Adesina, A.; Chumba, D.; Nelson, A. M.; Orem, J.; Roberts, D. J.; Wabinga, H.; Wilson, M.; Rebbeck, T. R. Improvement of Pathology in Sub-Saharan Africa. *Lancet Oncol.* 2013, *14*, e152−7.

(30) Dall, P.; Heider, K. H.; Hekele, A.; von Minckwitz, G.; Kaufmann, M.; Ponta, H.; Herrlich, P. Surface Protein Expression and Messenger RNA-Splicing Analysis of CD44 in Uterine Cervical Cancer and Normal Cervical Epithelium. *Cancer Res.* 1994, *54*, 3337−3341.

(31) Varughese, J.; Cocco, E.; Bellone, S.; Ratner, E.; Silasi, D. A.; Azodi, M.; Schwartz, P. E.; Rutherford, T. J.; Buza, N.; Pecorelli, S.; Santin, A. D. Cervical Carcinomas Overexpress Human Trophoblast Cell-Surface Marker (Trop-2) and Are Highly Sensitive to Immunotherapy with HRS7, a Humanized Monoclonal Anti-Trop-2 Antibody. *Am. J. Obstet. Gynecol.* 2011, *205*, 567.e1−567.e7.

(32) Went, P. T.; Lugli, A.; Meier, S.; Bundi, M.; Mirlacher, M.; Sauter, G.; Dirnhofer, S. Frequent EpCAM Protein Expression in Human Carcinomas. *Hum. Pathol.* 2004, *35*, 122−128.

DOI: 10.1021/acsnano.9b05634
ACS Nano 2019, 13, 11698−11706

(33) Sayed, S.; Cherniak, W.; Lawler, M.; Tan, S. Y.; El Sadr, W.; Wolf, N.; Silkensen, S.; Brand, N.; Looi, L. M.; Pai, S. A.; Wilson, M. L.; Milner, D.; Flanigan, J.; Fleming, K. A. Improving Pathology and Laboratory Medicine in Low-Income and Middle-Income Countries: Roadmap to Solutions. *Lancet* 2018, *391*, 1939−1952.
(34) The Distribution of the U.S. Primary Care Workforce. https://www.ahrq.gov/research/findings/factsheets/primary/pcwork3/index.html. Accessed August 18th, 2019.
(35) Auzel, F. Upconversion and Anti-Stokes Processes with F and D Ions in Solids. *Chem. Rev.* 2004, *104*, 139−173.
(36) Chen, G.; Qiu, H.; Prasad, P. N.; Chen, X. Upconversion Nanoparticles: Design, Nanochemistry, and Applications in Theranostics. *Chem. Rev.* 2014, *114*, 5161−5214.
(37) Wu, S.; Han, G.; Milliron, D. J.; Aloni, S.; Altoe, V.; Talapin, D. V.; Cohen, B. E.; Schuck, P. J. Non-Blinking and Photostable Upconverted Luminescence from Single Lanthanide-Doped Nanocrystals. *Proc. Natl. Acad. Sci. U. S. A.* 2009, *106*, 10917−10921.
(38) Park, Y. I.; Kim, J. H.; Lee, K. T.; Jeon, K.-S.; Na, H. B.; Yu, J. H.; Kim, H. M.; Lee, N.; Choi, S. H.; Baik, S.-I.; Kim, H.; Park, S. P.; Park, B.-J.; Kim, Y. W.; Lee, S. H.; Yoon, S.-Y.; Song, I. C.; Moon, W. K.; Suh, Y. D.; Hyeon, T. Nonblinking and Nonbleaching Upconverting Nanoparticles as an Optical Imaging Nanoprobe and T1Magnetic Resonance Imaging Contrast Agent. *Adv. Mater.* 2009, *21*, 4467.
(39) Sun, Y.; Zhu, X.; Peng, J.; Li, F. Core-Shell Lanthanide Upconversion Nanophosphors as Four-Modal Probes for Tumor Angiogenesis Imaging. *ACS Nano* 2013, *7*, 11290−11300.
(40) Kwon, O. S.; Song, H. S.; Conde, J.; Kim, H. I.; Artzi, N.; Kim, J. H. Dual-Color Emissive Upconversion Nanocapsules for Differential Cancer Bioimaging *in Vivo*. *ACS Nano* 2016, *10*, 1512−1521.
(41) Chen, S.; Weitemier, A. Z.; Zeng, X.; He, L.; Wang, X.; Tao, Y.; Huang, A. J. Y.; Hashimotodani, Y.; Kano, M.; Iwasaki, H.; et al. Near-Infrared Deep Brain Stimulation *Via* Upconversion Nanoparticle−Mediated Optogenetics. *Science* 2018, *359*, 679−684.
(42) Zhao, J.; Chu, H.; Zhao, Y.; Lu, Y.; Li, L. A Nir Light Gated DNA Nanodevice for Spatiotemporally Controlled Imaging of MicroRNA in Cells and Animals. *J. Am. Chem. Soc.* 2019, *141*, 7056−7062.
(43) Boyer, J.-C.; Van Veggel, F. C. J. M. Absolute Quantum Yield Measurements of Colloidal $NaYF_4$: Er^{3+}, Yb^{3+} Upconverting Nanoparticles. *Nanoscale* 2010, *2*, 1417−1419.
(44) Wilhelm, S. Perspectives for Upconverting Nanoparticles. *ACS Nano* 2017, *11*, 10644−10653.
(45) Wang, F.; Liu, X. Upconversion Multicolor Fine-Tuning: Visible to Near-Infrared Emission From Lanthanide-Doped $NaYF_4$ Nanoparticles. *J. Am. Chem. Soc.* 2008, *130*, 5642−5643.
(46) Liu, Y.; Tu, D.; Zhu, H.; Li, R.; Luo, W.; Chen, X. A Strategy to Achieve Efficient Dual-Mode Luminescence of Eu^{3+} in Lanthanides Doped Multifunctional $NaGdF_4$ Nanocrystals. *Adv. Mater.* 2010, *22*, 3266−3271.
(47) Wang, F.; Han, Y.; Lim, C. S.; Lu, Y.; Wang, J.; Xu, J.; Chen, H.; Zhang, C.; Hong, M.; Liu, X. Simultaneous Phase and Size Control of Upconversion Nanocrystals through Lanthanide Doping. *Nature* 2010, *463*, 1061−1065.
(48) Bruchez, M.; Moronne, M.; Gin, P.; Weiss, S.; Alivisatos, A. P. Semiconductor Nanocrystals as Fluorescent Biological Labels. *Science* 1998, *281*, 2013−2016.
(49) Wang, F.; Banerjee, D.; Liu, Y.; Chen, X.; Liu, X. Upconversion Nanoparticles in Biological Labeling, Imaging, and Therapy. *Analyst* 2010, *135*, 1839−1854.
(50) Chen, Q.; Xie, X.; Huang, B.; Liang, L.; Han, S.; Yi, Z.; Wang, Y.; Li, Y.; Fan, D.; Huang, L.; Liu, X. Confining Excitation Energy in Er^{3+} -Sensitized Upconversion Nanocrystals Through Tm^{3+} -Mediated Transient Energy Trapping. *Angew. Chem., Int. Ed.* 2017, *56*, 7605−7609.
(51) Zhen, X.; Tao, Y.; An, Z.; Chen, P.; Xu, C.; Chen, R.; Huang, W.; Pu, K. Ultralong Phosphorescence of Water-Soluble Organic Nanoparticles for *in Vivo* Afterglow Imaging. *Adv. Mater.* 2017, *29*, 1606665.
(52) Miao, Q.; Xie, C.; Zhen, X.; Lyu, Y.; Duan, H.; Liu, X.; Jokerst, J. V.; Pu, K. Molecular Afterglow Imaging with Bright, Biodegradable Polymer Nanoparticles. *Nat. Biotechnol.* 2017, *35*, 1102−1110.

DOI: 10.1021/acsnano.9b05634
ACS Nano 2019, 13, 11698−11706